Monte Carlo Simulation of Charge Transport in Amorphous Selenium Photoconductors

A Thesis

Submitted to the College of Graduate Studies and Research

in Partial Fulfillment of the Requirements for the Degree of

Master of Science

in the Department of Electrical Engineering

University of Saskatchewan

By

Zahid Shakoor

Saskatoon, Saskatchewan

PERMISSION TO USE

In presenting this thesis in partial fulfillment of the requirements for a postgraduate degree from the University of Saskatchewan, I agree that the Libraries of this University may make it freely available for inspection. I further agree that permission for copying of this thesis in any manner, in whole or in part, for scholarly purposes may be granted by the professor or professors who supervised my thesis work or, in their absence, by the Head of the Department or the Dean of the College in which my thesis work was done. It is understood that any copying or publication or use of this thesis or parts thereof for financial gain shall not be allowed without my written permission. It is also understood that due recognition shall be given to me and to the University of Saskatchewan in any scholarly use which may be made of any material in my thesis.

Requests for permission to copy or to make other use of material in this thesis in whole or part should be addressed to:

Head of the Department of Electrical Engineering

University of Saskatchewan

Saskatoon, Canada, S7N 5A9

ABSTRACT

The electronic properties of amorphous materials are greatly affected by the density of localized states in the mobility gap of these materials. The exact shape of the density of states (DOS) distribution in amorphous selenium (a-Se) is still unresolved despite decades of research. One of the most commonly employed methods to investigate charge transport properties in high resistivity materials is time-of-flight (TOF) transient photoconductivity experiment. The TOF transient photoconductivity technique is used to measure the induced photocurrent in the external circuit when the sample is photoexcited. Information pertaining to carrier mobility and other carrier parameters are deduced from the shape of the photocurrent. The investigation of the charge transport phenomenon is well known to be a complicated task. Monte Carlo (MC) simulation method has become a standard method for carrier transport studies in amorphous materials. The purpose of this research work is to develop a Monte Carlo simulation model for charge transport in typical TOF transient photoconductivity experiment to investigate the DOS distribution in a-Se. The MC simulations were first performed for relatively simpler models for which theoretical and analytical solutions were available. The MC model developed here is based on simulating the drift of carriers resulting from photogeneration, subject to the influence of an applied electric field and multiple trapping events. The free drift time of photocarriers and their dwell time in the traps are stochastic in nature, in accordance with the probabilities of these events. Electron time-of-flight transient photocurrents were calculated in amorphous selenium as a function of the electric field. The distribution of localized states (DOS) in a-Se has been investigated by comparing the experimentally measured and calculated transient photocurrents. The analysis of multiple-trapping transport has been done by the discretization of a continuous DOS. The DOS distribution has been optimized to produce the best agreement between the calculated and measured transient photocurrents. The resulting DOS has distinct features: A first peak at ~0.30 eV below E_c with an amplitude ~10^{17} eV^{-1} cm^{-3}, a second small peak (or shoulder) at 0.45–0.50 eV below E_c with an amplitude 10^{14}–10^{15} eV^{-1} cm^{-3}, and deep states with an integral concentration 10^{11}–10^{14} cm^{-3} lying below 0.65 eV, whose exact distribution could not be resolved because of the limitations of the available experimental data. The density of states (DOS) distribution in the vicinity of the valence band mobility edge in vacuum coated a-Se films has been investigated by calculating the MC hole transient photocurrents at different temperatures, and also the dependence of the drift mobility on the temperature *and* field. The calculated TOF transient photocurrents were compared with experimental data published elsewhere. It is shown that, analogous to electron transport in a-Si:H, the DOS near E_v is a featureless, monotonically decreasing distribution in energy up to E_v + 0.4 eV, *without* the 0.28 eV peak near the valence band which was thought to control the hole drift mobility. Such a DOS was able to account for hole TOF data reported previously by several authors to date.

ACKNOWLEDGEMENTS

I am deeply grateful to my supervisor, Professor S.O. Kasap, for his continuous guidance, encouragement, wholehearted supervision, and financial support throughout the progress of the work. I am especially thankful to Dr. Cyril Koughia for his guidance and support throughout the duration of this project. This work could have never materialized without his help. I am grateful to my friend Mohammad Yunus for many helpful discussions. I would also like to thank my friends Shaikh Hasibul Majid, Zahangir Kabir and all my colleagues in our lab for their support, encouragement and helpful discussions. Finally I would like to thank my parents and my family for their patience and support.

TABLE OF CONTENTS

LIST OF FIGURES

LIST OF ABBREVIATIONS

AB	anti bonding
AMA	active matrix array
a-Se	amorphous selenium
a-Si:H	hydrogenated amorphous silicon
BJT	bipolar junction transistor
CB	conduction band
CFO	density of states model proposed by Cohen, Fritsche and Ovshinski
CMOS	complementary metal oxide semiconductor
DEC	deviant electron configurations
DOS	density of states
DR	digital radiography
EHP	electron hole pair
ESR	electron spin resonance
FET	field effect transistor
HARP	high gain avalanche rushing photoconductor
HDTV	high definition television
IVAP	intimate valence alternation pair
LCD	liquid crystal display
LP	lone pair
MC	Monte Carlo
MSD	mean square deviation
NB	non bonding

NSB	normal structure bonding
PDF	probability density function
SCP	space charge perturbed
TCT	transient charge technique
TFT	thin film transistor
TP	transient photoconductivity
VAP	valance alternation pair
VB	valence band

1 Applications of Amorphous Semiconductors

1.1 Introduction

Solids in terms of regularities in their atomic structure are broadly categorized into two groups; *crystalline* and *amorphous*. Crystalline materials are solids in which atoms are arranged in a perfect periodic order throughout the solid. Amorphous materials, on the other hand are the ones in which the constituent atoms lack such periodicity. The lattice structure in such materials contains some deviations from the "perfect" periodic lattice arrangement that serves to destroy the overall periodicity of the solid.

The physics of crystalline semiconductors has been very well understood after the advent of quantum mechanics. The periodic structure of the crystalline materials led to mathematical simplifications; such as the Bloch theorem, which made it easy to develop the theoretical framework to understand the properties of these materials. One of the most prominent inventions based on crystalline material was the invention of the transistor which literally revolutionized electronic devices. The vast majority of the modern electronic systems involve the employment of components fabricated from crystalline semiconductors. Amorphous materials, on the other hand did not experience such a rapid development. The short-range order of the amorphous semiconductors resulted in mathematical complexities and hence retarded the understanding process of the theory of such materials. For a long period of time, amorphous materials were not considered to behave as semiconductors, although there were experimental evidences suggesting otherwise, e.g. the photoconductivity of amorphous selenium and the ability of conventional glasses to transmit light of sufficiently high wavelength. It was not until the mid-1950s, when Kolomites and co-workers [1] reported semiconducting behavior in

various chalcogenide glasses and ushered in an era of interest in amorphous semiconductors [2].

One of the main driving forces in research on amorphous and microcrystalline semiconductors has been, and still is, the ability of these materials to be economically prepared in large areas for applications such as displays, scanners, solar cells, image sensors, position sensors, and other similar large area applications. This phenomenon gives amorphous materials a significant advantage over their crystalline counterparts since the preparation of crystalline solids usually requires carefully controlled growth techniques.

Amorphous selenium (*a*-Se) is one of the most widely studied elemental semiconductors due to its numerous commercial applications and its status as a prototype amorphous semiconductor. It was first used as a resistive material [3], but it was not long before its photoconductive properties were discovered. Its most important application to date has been in Xerography. During fifties and sixties it was used in the commercial Xerox photocopiers. Later in the eighties it was replaced by the organic photoconductors which are more cost effective. At present, its excellent photoconductive property has again attracted interest due to its application in two imaging devices. First is its use as an X-ray photoconductor in the recently developed and commercialized direct conversion X-ray image detectors. The second is its use as an avalanche photoconductor in ultrahigh sensitivity vidicon tubes called HARPICONS. Despite the long history of research and interest it has generated, the electronic properties of a-Se have still not been not completely understood. This is partially due to the strong influence of small amounts of impurities and preparation conditions on its electronic properties. Structural defects inherent in disordered solids and impurities greatly affect the charge transport process in amorphous selenium. Successful use of a-Se in commercial applications therefore depends on our understanding of the electronic properties of this material.

In the next section the principle of operation of some commercial applications of amorphous selenium is briefly described. Then the research objective of this work and the thesis layout is presented in this chapter.

1.2 Application of Amorphous Selenium in Digital Xerography

1.2.1 Film-Based Radiography

The purpose of this section is to illustrate the application of a-Se in X-ray image detector. Radiographic imaging is one of the most commonly employed diagnostic tools used by physicians today. This imaging technique uses X-rays as the information carriers. The differential attenuation of the incident X-ray radiation as it passes through the patient's body is used to obtain the image of the internal structure of the body which is captured on a photographic film or other radiographic detector. As the X-rays pass through the patient's body, the intensity of the radiation is modulated. The modulation takes place because X-ray attenuation is different for different parts in the body, e.g. the bones are denser than fat and the tissues and therefore absorb more radiation. The modulated X-ray radiation; also referred to as *remnant radiation*; is projected onto an X-ray detector. This modulated radiation contains information about the internal structure of the patient's body and the X-ray detector converts the intensity pattern of the remnant radiation into a measurable response. The final image typically consists of various light and dark regions representing the internal structure of patient's body. For example, the area of the detector falling in the shadow of bones appears lighter in the image because relatively few X-rays propagate through the bones and generate a small response in the detector. Conversely, areas falling under the shadow of soft tissue such as fat and muscle appear brighter in the image because a large number of X-rays pass through this area without being absorbed and the detector records a large response.

At present, the majority of X-ray detectors in use are based on photographic films. The film-based detector consists of a photographic film sandwiched between two fluorescent screens. The cross-sectional view of a film based detector is shown in Figure 1.1. The incident X-rays are converted into visible light upon irradiation and expose the film. The intensity pattern is thus registered onto the film and the film is later developed using standard techniques.

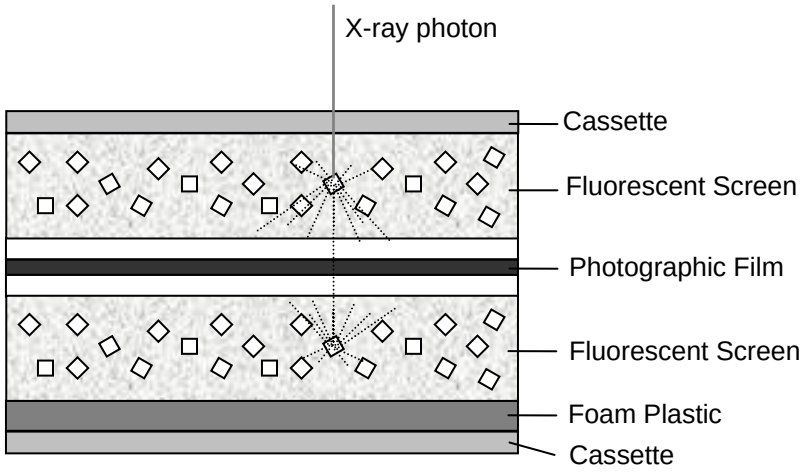

Figure 1.1: Cross-sectional view of a film-screen cassette [4].

Film-based technology offers good image quality, but it suffers from some drawbacks. The film-screen cassette has to be manually inserted in the radiographic system before exposing the patient to X-ray radiation. After exposure, the cassette is physically taken to a dark room, where it is developed using chemical agents. If the radiologist is not satisfied with the image quality, the whole process is repeated after making necessary adjustments. This process from X-ray exposure to obtaining the final image is laborious and time consuming. The film is developed using chemical techniques and is not reusable, hence it produces chemical waste raising environmental concerns. The interaction between human body and radiation results in biological damage. Therefore the reduction of X-ray exposure is of prime importance for patient safety. Another serious drawback of film-based radiographic image is archiving and transportation of the radiographic images. Usually the radiographic images are archived at some central location in the health care facility and have to be physically delivered to the health care provider when required. A promising alternative to the analog film based radiographic imaging is the solid state digital radiography (DR) and is discussed in the following section.

1.2.2 Digital Radiography

Digital radiography overcomes nearly all of the disadvantages inherent in film-based radiography. Radiographic detectors used in digital radiography are usually connected to a computer via some peripheral devices and the radiographic image can be viewed on a monitor immediately after exposure. Image quality in digital radiography can be improved by means of image processing software and the radiological images could be more easily compared with the images obtained from other imaging methods. The radiographic image in digital form could easily be stored and distributed electronically within the hospital and to other distant locations for secondary opinion, hence facilitating archiving and making remote access possible. Highly qualified personnel in larger centers could provide service and help with diagnosis to patients in remote and distant regions by means of "teleradiology" [5].

In digital radiography the film-screen cassette is replaced by a photoconductor-based X-ray image detector that converts the X-rays into an electronic signal which is then digitized by an analog to digital (A/D) converter and recorded by computer memory. The image can then be processed, displayed, transmitted or archived using a computer. Currently, digital radiography is in use through three approaches, two of which make use of phosphor screens. In the first phosphor-based technique, a video camera is optically coupled to an X-ray image intensifier. The signals from the video camera are then digitized to provide instant readout. The second phosphor-based technique is the stimulable phosphor system. The phosphor screen used for this purpose contains traps for electrons excited by incident radiation. The phosphor screen is then illuminated from point to point using a red laser. The latent image therefore is obtained in form of blue light from the trapped electrons. This type of detection is referred to as *indirect conversion* because the electronic signal is generated indirectly from the pattern of visible light given off when X-rays strike the phosphor screen. It is necessary that the phosphor layer is thick enough to stop the energetic X-rays. Both these phosphor based systems have some disadvantages. The radiographic images obtained from these systems exhibit poor resolution which is the consequence of the spreading of light in the thick phosphor layer. The later mentioned technique has the disadvantage of not providing instant image. The phosphor screen must

be carried to the laser scanner for readout by a photomultiplier, which performs the digitization [5].

Third and one of the most promising digital radiographic system is a direct conversion flat panel X-ray detector. This system has been widely discussed in literature by Kasap and co-workers [6,7,8,9,10,11,12,13], and is reviewed here along the lines of Reference [6]. The incident X-rays are directly converted to electrical charge that is the consequence of the ionization of the atoms in the detector. This function is achieved using a large-area, thin-film-transistor, (TFT) active-matrix array (AMA) with an electroded X-ray photoconductor. The detector captures the X-ray image and converts it directly to a digital signal for processing, display and storage. An electric field is created across the photoconductor by applying a biasing voltage to the electrodes. The charge carriers released in the photoconductor by the absorption of X-rays are guided to the photoconductor surface under the influence of the electric field with negligible lateral spreading making higher resolution possible. This combination of an active matrix array (AMA) of thin film transistors (TFT) and an X-ray photoconductor constitutes a direct conversion X-ray image detector. The term "direct" implies that the X-ray photons in these detectors are directly converted to charge carriers that are subsequently collected and detected. The development of displays made up of individual flat panel thin film transistors (TFTs) was the important first step in the advancement of direct conversion X-ray detector technology. The flat panel displays are also called active matrix arrays (AMAs) due to the fact that active devices, i.e. thin film transistors, are arranged in arrays forming a large matrix. The flat panel displays are being manufactured from TFTs using the hydrogenated amorphous silicon (a-Si:H), microcrystalline silicon and polycrystalline cadmium selenide (CdSe).

A simplified schematic of an AMA is shown in Figure 1.2. An AMA consists of millions of individual pixel electrodes connected by transistors (one per pixel) to electrodes passing over the whole array to auxiliary electronics on the periphery. The thin film transistors act as switches to control and coordinate the clocking out of the charge a line at a time. The magnitude of the charge stored in each pixel represents the image resulting from the ionization due to remnant radiation.

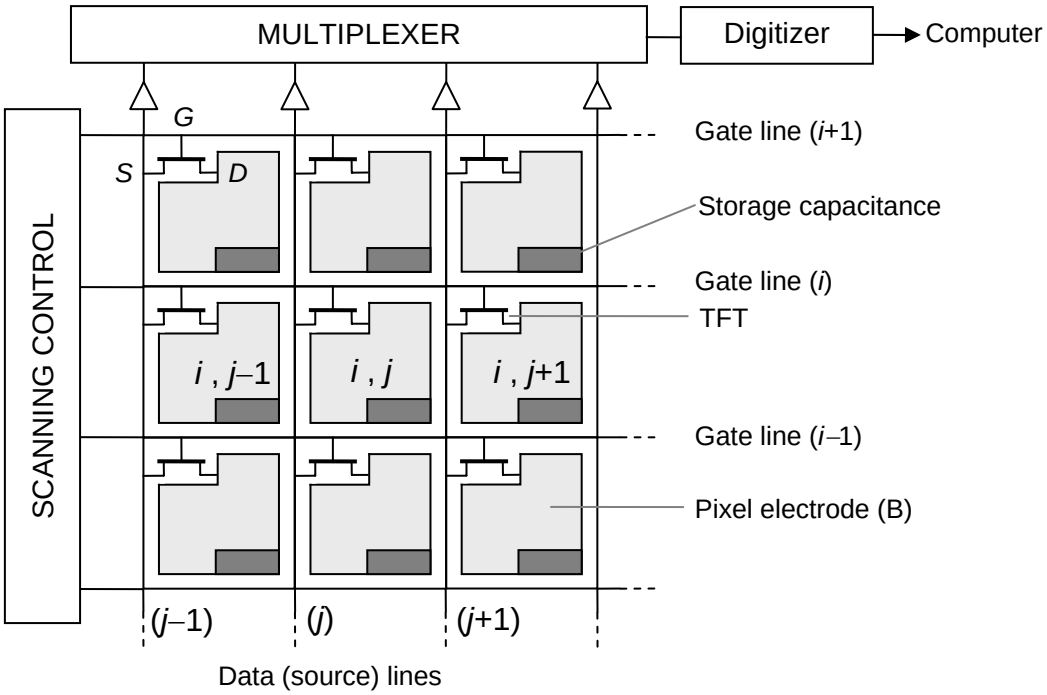

Figure 1.2: Thin film transistor (TFT) active matrix array (AMA) for use in X-ray image detectors with self-scanned electronic readout. The AMA has of $M \times N$ pixels [6].

In general, an AMA consists of $M \times N$ TFT-based pixels (i, j). Each pixel consists of a signal storage capacitor C_{ij} that collects the charge through a charge collection electrode labeled as B. The charge stored in these capacitors can be read by properly addressing the TFT, acting here as switches, by the way of the gate line i and source line j. External electronics and software, by proper self-scanning, converts the charge stored on C_{ij} to a digital image. No external means, such as scanning laser beam as in the case of some other digital X-ray imaging systems, are used to extract the information stored in these pixels, hence the term self-scanning is used for these types of detectors.

In order to create a flat panel X-ray photodetector, the AMA panel is coated with a layer of amorphous selenium (a-Se), as shown in Figure 1.3. An electrode is then deposited on top of the a-Se layer. In order to create a uniform electric field across the a-Se, a biasing

potential is applied to the deposited electrodes. Upon irradiation the photoconductor absorbs the X-rays and the photogenerated electron hole pairs (EHPs) travel towards the respective electrodes under the influence of the applied bias. Electrons are collected by the positive electrode, labeled as here as A, and holes are accumulated in the storage capacitor C_{ij}, and the resulting charge Q_{ij} is read during self-scanning. The capacitance of the photoconductor layer on each pixel is much smaller than the pixel capacitance C_{ij} so that most of the applied voltage drops across the photoconductor. The amount of charge in each pixel is therefore proportional to the amount of X-rays absorbed by the photoconductive layer above that pixel. As shown in the Figure 1.3, the gates of all TFTs in a row are connected and all the TFTs in a column have their sources connected. When the gate line i is activated, all the TFTs in that row are turned "on" and N data lines from $j = 1$ to N then read the charges on the pixel electrodes in row i. The parallel data are then multiplexed into serial data, digitized and then fed into a computer for imaging. Similarly the scanning control then activates the next row, $i + 1$, and then performs the same actions until all the rows are scanned and eventually the complete image is acquired on the computer [5].

The high sensitivity and high resolution render this system a good candidate compared to other contenders in high resolution, low dosage digital radiography as recently analyzed and discussed in literature [14,15,16]. The resolution in digital radiographic detectors is determined by the pixel size which in present experimental detectors is typically 150 μm but is expected to be as small as 50 μm in future detectors. This resolution is necessary for applications like mammography. Furthermore the flat panel detector also has potential for use in real-time interactive X-ray imaging called fluoroscopy.

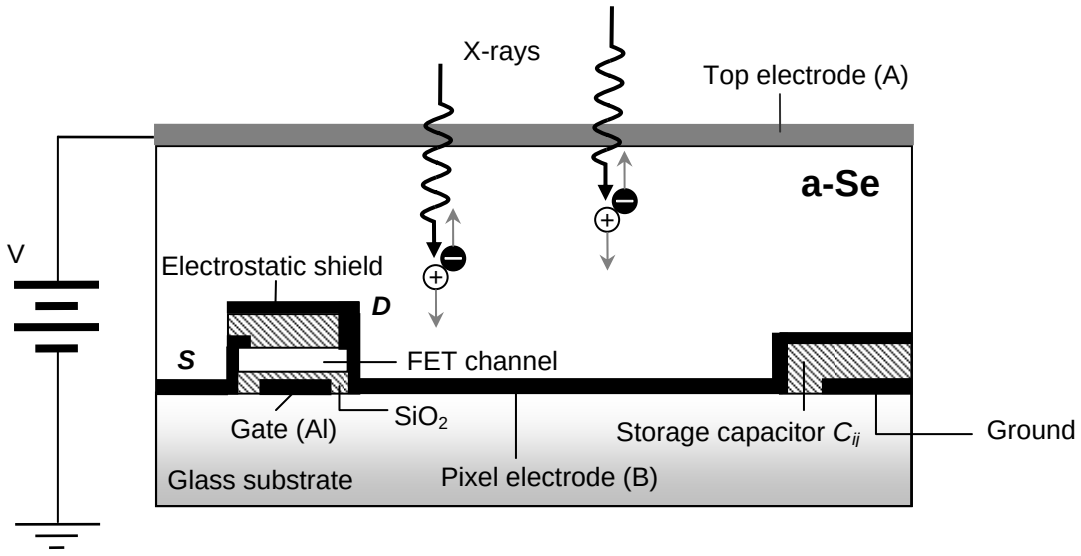

Figure 1.3: Cross section of a single pixel (i,j) with a TFT showing the accumulation of X-ray generated charge on the pixel electrode (exaggerated scale). Pixel size is typically 150μm × 150μm in size [6].

1.2.3 Practical Advantages of a-Se as X-Ray Photoconductor

Amorphous selenium is one of the leading candidates to be used as a photoconductive layer coating on AMA. This is because of the distinct advantage that it can be easily prepared as thick films or layers over large areas by straightforward thermal evaporation in a conventional vacuum coater. Vacuum deposition technique consists of loading vitreous selenium pellets into a stainless steel boat. The boat is resistively heated by passing a large current through it until the pellets reach the melting point and evaporate. The melting point for selenium is 220 °C. Selenium vapor condenses onto the AMA substrate to form a layer of a-Se. Typical boat temperature is between 250-280 °C and that of substrate is 65-70 °C. These temperatures are low enough to spare the flat panel AMA and its delicate peripheral electronics from damage. Compared with other photoconductor materials this is another significant advantage since the melting temperatures for the other materials are relatively higher.

Moreover, since typical deposition rates are 2–4 μm per minute, 200 μm photoconductive coating can be applied in less than an hour. In addition to being convenient to prepare, flat panel sensors are cost effective because the AMAs used are readily available for use in the market.

Many other semiconductors can also be vacuum-deposited, but they generally result in polycrystalline films and require annealing at high temperatures (hotter than 200 °C for lead iodide) to eliminate structural defects. Also the grain boundaries in polycrystalline films can trap charge carriers, limiting charge transport to the point of making the photoconductor practically useless [5].

1.3 TV Camera Pick-Up Tubes and Avalanche Multiplication

The purpose of this section is to discuss the application of a-Se in ultra high sensitivity TV pickup tubes. This section is discussed along the lines described in Reference [6]. One of the most interesting properties of a-Se is that at sufficiently high electric fields, charge carriers in a-Se exhibit avalanche multiplication. This phenomena has been exploited in the development of super sensitive TV pick up tubes (the HARPICON vidicons) with a gain as high as 800. In this section the principle of operation of the HARPICON and the avalanche multiplication that has enabled super sensitive pickup tubes for high-definition television (HDTV) is discussed. A commercially available TV pickup tube that employs amorphous Se-As-Te (selenium-arsenic-tellurium) alloys is Hitachi's Saticon. A schematic diagram of the structure of a typical a-Se Saticon is illustrated in Figure 1.4. This pickup tube utilizes the high panchromatic photosensitivity of the Se-Te alloy and the relatively fast drift mobility of a-Se. The Se-Te alloy is sandwiched between layers of CeO_2 and Sb_2S_3 which act as barriers for holes and electrons respectively. Electrons are injected by the scanning electron beam and they become trapped in the Sb_2S_3 layer resulting in a negative space charge in this layer. Exposing the face plate to light leads to photogeneration of holes in a-Se which transit across towards the Sb_2S_3 layer to recombine with the electrons trapped in that layer. The photogeneration is

contained within the region with high Te concentration. In order to limit the crystallization process in a-Se, 1% As to a-Se is added.

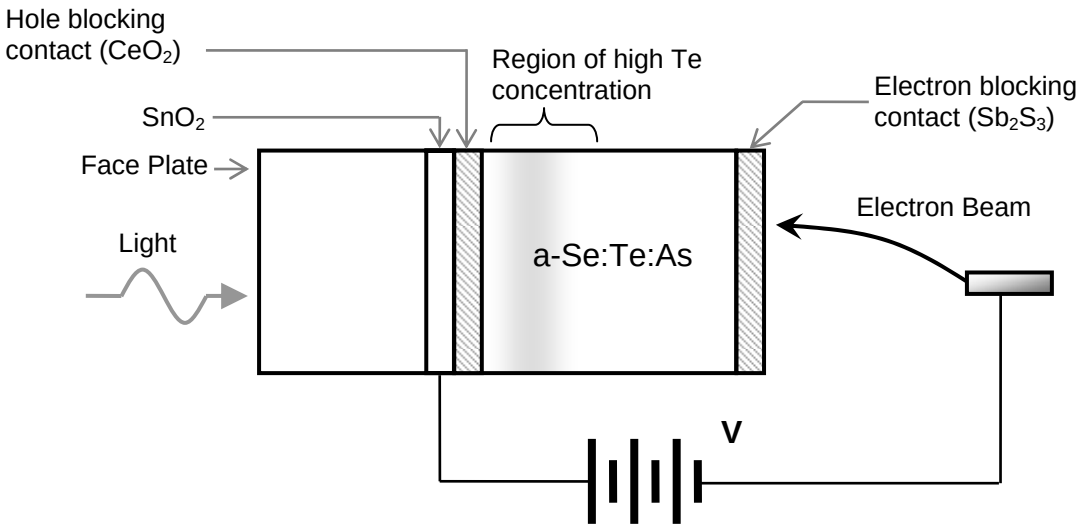

Figure 1.4: Schematic diagram of a Saticon TV image pickup tube utilizing an s-Se:Te:As alloy. The Te concentration is concentrated in the region shown in the figure [5].

Tanioka and coworkers at NHK labs developed a super-sensitive photoconductive target for use in HDTV camera pickup tubes. The target is called HARP; acronym for high-gain avalanche rushing amorphous photoconductor; and the vidicon using the HARP target is called HARPICON or a-Se avalanche vidicon. The entire target is about ~2 μm or thicker depending on the sensitivity requirements of the target. The basic structure of the HARP target is illustrated in the Figure 1.5.

The layers of CeO_2 and SbS_3 act as blocking contacts for hole and electron injection respectively. The transparent signal electrode SnO_2 is biased positively with respect to the cathode. The incident light is absorbed in the a-Se layer and results in photogeneration of electron hole pairs (EHPs). These EHPs drift towards their respective electrodes under the influence of the electric field. As the photogenerated holes drift through the a-Se layer towards the back electrode under the action of high electric fields, they experience

avalanche multiplication and hence effective quantum gain greater than unity. Quantum efficiency is defined as the number of EHPs generated per absorbed photon and quantum gain is the number of EHPs collected per photon. The effective quantum gain resulting from avalanche multiplication depends on the magnitude of the applied electric field and photoconductor thickness. For example, a HARP target with 2 μm thickness and an applied field of 120 V/μm results in a quantum gain of 10, whereas a 24.8 μm thick target at an applied field of 100V/ μm results in a gain of ~ 1000. TV pickup tubes using such HARP targets have far superior sensitivity than conventional TV pickup tubes and hence constitute ultra-high sensitive image pickup tubes.

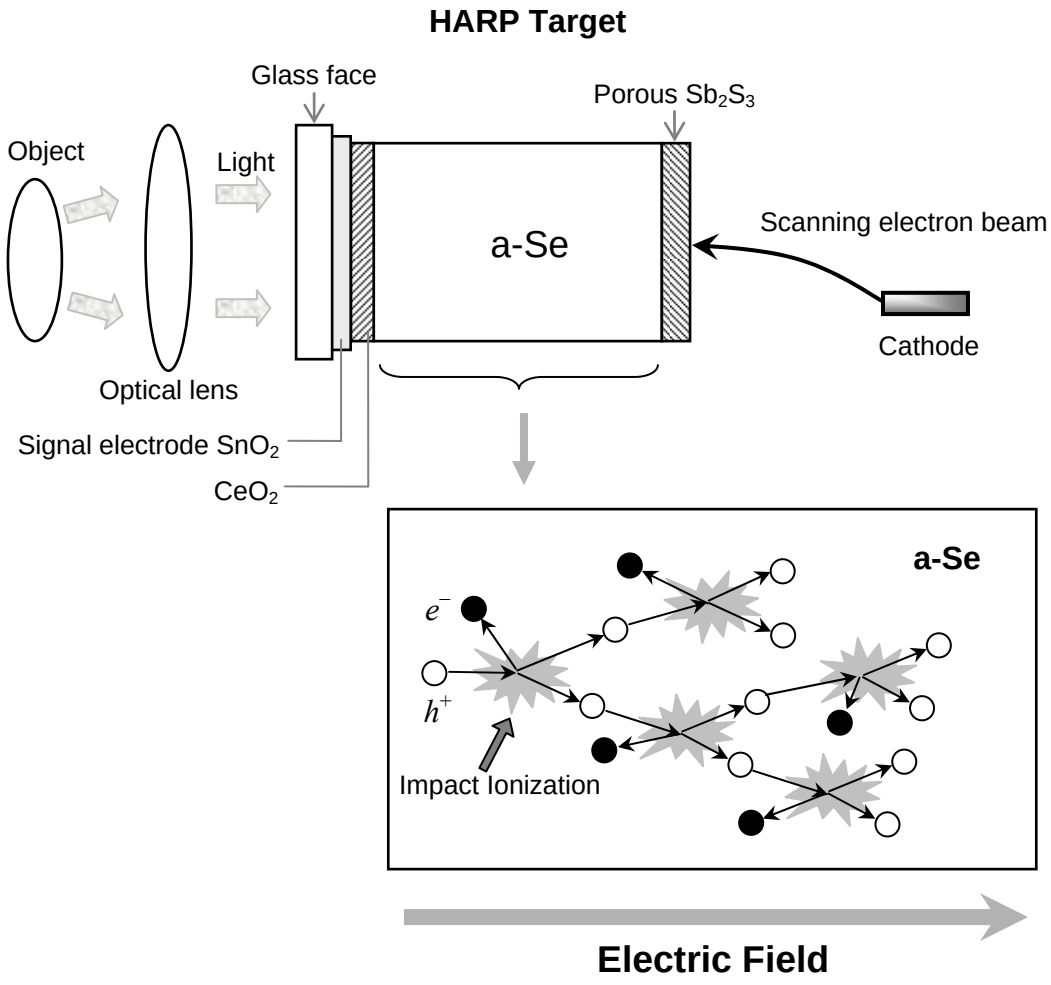

Figure 1.5: A schematic illustration of a HARPICON. Avalanche breakdown by impact ionization in the a-Se layer is also illustrated. One photogenerated hole results in many electron-hole pairs to be generated by impact ionization (avalanche breakdown) in the a-Se layer where the electric field is very large [5].

1.4 Research Objectives

Due to the various commercial applications, some of which were briefly described in this chapter, thorough understanding of the electronic properties of amorphous selenium is crucial for its useful utilization in commercial products. Theoretical formulation of electronic and optoelectronic properties using mathematical tools is either extremely difficult or impossible for semiconductors lacking periodicity in their atomic arrangement. Various experimental techniques are used to deduce information regarding the charge

transport mechanism in amorphous semiconductors. One of the most commonly employed methods to investigate the carrier transport process is the time-of-flight (TOF) transient photoconductivity. Important parameters like effective carrier mobility and carrier lifetimes are obtained from these experiments. These parameters are used to understand the science and technology of amorphous semiconductors and hence help to improve the devices employing amorphous semiconductors. This research project investigates the carrier transport mechanism in amorphous selenium in a typical time-of-flight transient photoconductivity experiment using Monte Carlo simulation techniques.

One of the most important features of amorphous materials is the presence of localized states in the mobility gap. The electronic properties of amorphous materials are strongly associated with these localized states. The shape of the density of states (DOS) for amorphous selenium is still controversial despite a long history of research. There are at least two general models of the density of states for amorphous selenium; both having distinctly different features in their DOS distribution. These DOS distributions have been derived mostly from charge transport and trapping experiments, such as Xerographic discharge, time-of-flight (TOF) and post-transit photocurrent analysis. Among these methods of investigation, the most common and widely used method is the TOF technique.

Monte Carlo simulation has become a standard method in studying the charge carrier transport mechanism in many amorphous materials. A Monte Carlo (MC) model of the TOF experiment is used to calculate the transient photocurrents of the TOF experiment. The MC model will employ a DOS distribution below the conduction band (CB) edge, simulating electron transport across the sample undergoing trapping and release events based on the DOS distribution used, and the resulting current waveforms are compared with current waveforms measured from experiments. The density of states distribution is optimized until reasonable agreement between experimental and calculated waveforms is obtained. This procedure is repeated for various applied bias conditions. The MC simulation technique provides the flexibility of incorporating practical aspects of the experiment without making the model overly complicated. Effect of finite absorption of radiation on carrier generation position in the sample will be incorporated in the MC simulation model.

The density of localized states distribution in the lower half of the mobility gap near the VB edge is even more controversial. A new study suggests that the distribution is featureless and monotonically decaying. The featureless DOS distribution near the valence (VB) edge will be used to study hole transport in a-Se samples. The calculated transient photocurrents will be compared with data published elsewhere.

1.5 Thesis Outline

This thesis is divided into seven chapters. This chapter briefly describes the two most recent applications of a-Se that have attracted interest of researchers. The principle of operation of direct conversion X-ray photo-detector and ultra high sensitivity TV pickup tubes (HARPICON) and the objective of this work are discussed.

In Chapter 2, the atomic and band structure of amorphous materials is described. The different bonding arrangements leading to possible defects and the DOS model for a-Se are then discussed. The localized states greatly affect the charge transport properties in amorphous materials. Some charge transport mechanisms are also discussed in Chapter 2. In Chapter 3, the theoretical principles of the TOF transient photoconductivity technique is presented, and expressions for the TOF transient photocurrent under a variety of trapping conditions (i.e. set of discrete traps, a continuous trap distribution) are developed. The Monte Carlo simulation model developed to study charge transport in semiconductors with a monoenergetic trap distribution and a three trap level distribution is discussed in Chapter 4. The DOS distribution in the upper half of the mobility gap is investigated in Chapter 5 by comparing the TOF transient photocurrents calculated using MC techniques with those measured experimentally. In Chapter 6, the proposed DOS distribution model in the lower half of the mobility gap is investigated. In Chapter 7, the conclusions inferred from this research are outlined.

2 Properties of Amorphous Selenium

2.1 Introduction

After the pioneering work of Kolomites and co-workers [1] on amorphous chalcogenide glasses, amorphous selenium has attracted considerable attention because of its status as a *prototype* non-crystalline semiconductor [17]. Simplifying concepts such as the Bloch theorem are not valid for materials lacking periodicity in their atomic structure. A more in-depth understanding of such materials can be achieved by looking at the arrangement of constituent atoms and the different bonding possibilities among these atoms. In this chapter the atomic structure of amorphous solids especially amorphous selenium and possible bonding arrangements which can occur in amorphous selenium are studied. The effect of the bonding arrangements on the density of states (DOS) is also assessed. This review will provide some background to the electronic properties of a-Se.

2.2 Structure of Amorphous Solids

The key features of atomic arrangement in a perfect crystal and an amorphous material are shown in Figure 2.1. The solid spheres represent the equilibrium position about which the atoms oscillate. In the crystalline structure, there exists a translational periodicity; almost all the bond lengths and bond angles are identical, independent of the atom's position in the solid. This results in long-range order throughout the solid. In amorphous solids there are slight variations in the bond lengths and bond angles. These slight variations serve to dissolve the spatial periodicity of the structure for distances

greater than a few atomic radii. The amorphous structure therefore exhibits short-range order rather than long-range order characteristic of crystalline states. This type of disorder is called topological disorder. In some cases, the disorder in the amorphous semiconductors makes it impossible to satisfy the bonding requirement for the atom. This leads to the formation of dangling bonds which has significant influence on the physical and electronic properties of these materials. Other forms of disorder include spin disorder, compositional disorder (for compound materials) and vibrational disorder.

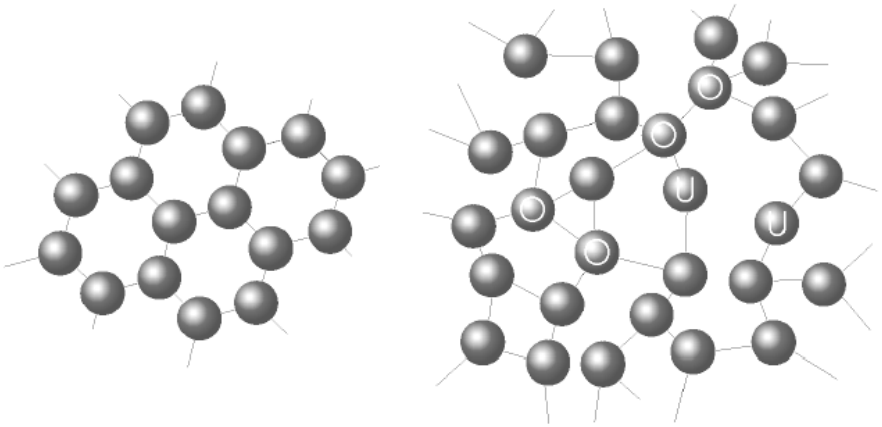

Figure 2.1: Comparison of the atomic arrangements in (a) a perfect crystal and (b) an amorphous semiconductor. The atomic structure shown here is three-fold coordinated, with the atoms labeled with U are under- and atoms labeled with O are over-coordinated.

Despite lacking long-range spatial order, the amorphous solid still has a high degree of short range order. Generally the valency requirements are satisfied for individual atoms, and each atom is normally bonded to the same number of nearest neighbors. Hence it can be said that no solid is strictly "amorphous" in the sense of completely lacking in any type of definable order [2,18].

2.3 Band Structure of Amorphous Semiconductors

A solid consists of a large number of atoms which interact with each other resulting in a large number of electronic states within a small band of energy. Within these bands the electron energy levels are almost continuous. The electron energy falls within the possible states in these bands of energies. The interaction of bonding orbitals leads to the formation

of an energy band called the valance band (VB) by the virtue of the valence electrons it contains. The interaction between the anti-bonding orbitals leads to the formation of another band that is entirely vacant and is called the conduction band (CB). In semiconductors, the conduction band and valance band are separated from each other by a fixed *energy gap* or *bandgap* E_g. This bandgap is measured from the top of the CB to the bottom of VB. There is no state in the bandgap and an electron cannot have energy within E_g. E_v is the energy at the top of the VB and E_c is the energy at the bottom of the CB [19]. These bands lead to the important concept of density of states (DOS), which is defined as the number of possible electronic states per unit volume per unit energy. The density of states for a perfect crystalline structure is shown in Figure 2.2(a).

During the development of the band theory of electronic conduction in crystalline semiconductors, the concept of bands of allowed electronic energy states, separated by forbidden ranges of energy became firmly associated with materials with long rage order. The band theory was thought be the consequence of interaction of electronic wave function with periodic lattice with long-range order. Consequently for a period of time, amorphous materials, lacking long rage periodicity, were not considered to behave as semiconductors.

N. F. Mott in 1960 [20] was the first to generalize the band theory of crystalline semiconductors to amorphous materials. His work was based on the assumption that despite the differences in their atomic arrangements, crystalline and amorphous semiconductors will have similarities in their band structure. He noted that in all crystalline solids, the electronic structure has the following universal features:

1. the individual electrons are described by extended Bloch wave functions possessing long range order in both amplitude and phase
2. the allowed electronic states form bands with sharp edges separated by well defined energy gap

Mott postulated that in amorphous semiconductors Bloch wave functions have amplitudes with long-range order but their phase will only have short-range order. Therefore the sharp band edges that were the result of long-range periodicity will be replaced by “tails” of localized states as shown in Figure 2.2(b). Mott’s hypothesis was

based on the work of P.W. Anderson [21], who in 1958 showed that the translational and compositional disorder in amorphous materials will result in "localized" states. These localized states, which lie in the forbidden energy gap, have an adverse effect on the carrier drift mobility. The carriers have finite band transport mobility in the extended states, while in localized states mobility is controlled by thermally activated tunneling between localized states. This region of abrupt change in mobility gives rise to a *mobility gap* in amorphous semiconductors, similar to the *bandgap* of crystalline semiconductors.

M. H. Cohen, H. Fritzsche and S. Ovshinsky [22] advanced a model that was based on the assumption that Mott had underestimated the degree of disorder. Their model (also known as the CFO model) consisted of localized states that extend throughout the mobility gap. The density of states distribution based on CFO model is shown in Figure 2.2(c). Attempts to apply this model to amorphous semiconductors in general failed, since many amorphous semiconductors posses a significant degree of short range order.

N. F. Mott and E. A. Davis [23] in 1971 proposed another idealized model with comparatively limited linear tails of localized states, shown in Figure 2.2(d). The Fermi level was assumed to be close to the center of the mobility gap pinned by another small group of localized states. All solids, amorphous or crystalline, contain atoms that are coordinated differently from their normal structure bonding (NSB). The local connectivity of the network is well defined on a local basis. This may lead to well defined defects in the amorphous structure such as dangling bonds, chain ends, vacancies, substitutional impurities, interstitials etc. Such defects are called deviant electron configurations (DECs) and may lead to localized states within the mobility gap of the material in addition to the disorder induced states. The carrier transport properties in crystalline semiconductors are well known to be controlled by these defects.

Marshall and Owen performed studies on the charge transport properties of amorphous chalcogenide semiconductors. Their experiments indicated the presence of localized states in the mobility gap at various well-defined energies in addition to the tail states. These defect states are shown in Figure 2.2(e). It had been previously assumed that the disorder induced tail states would be sufficient to take into account the DEC defects mentioned above. But Marshall and Owen argued otherwise and suggested that the

localized mid-gap states were the consequence of these intrinsic defects. Spear and co-workers [24] in 1976 studied amorphous silicon (a-Si) and reached similar conclusions.

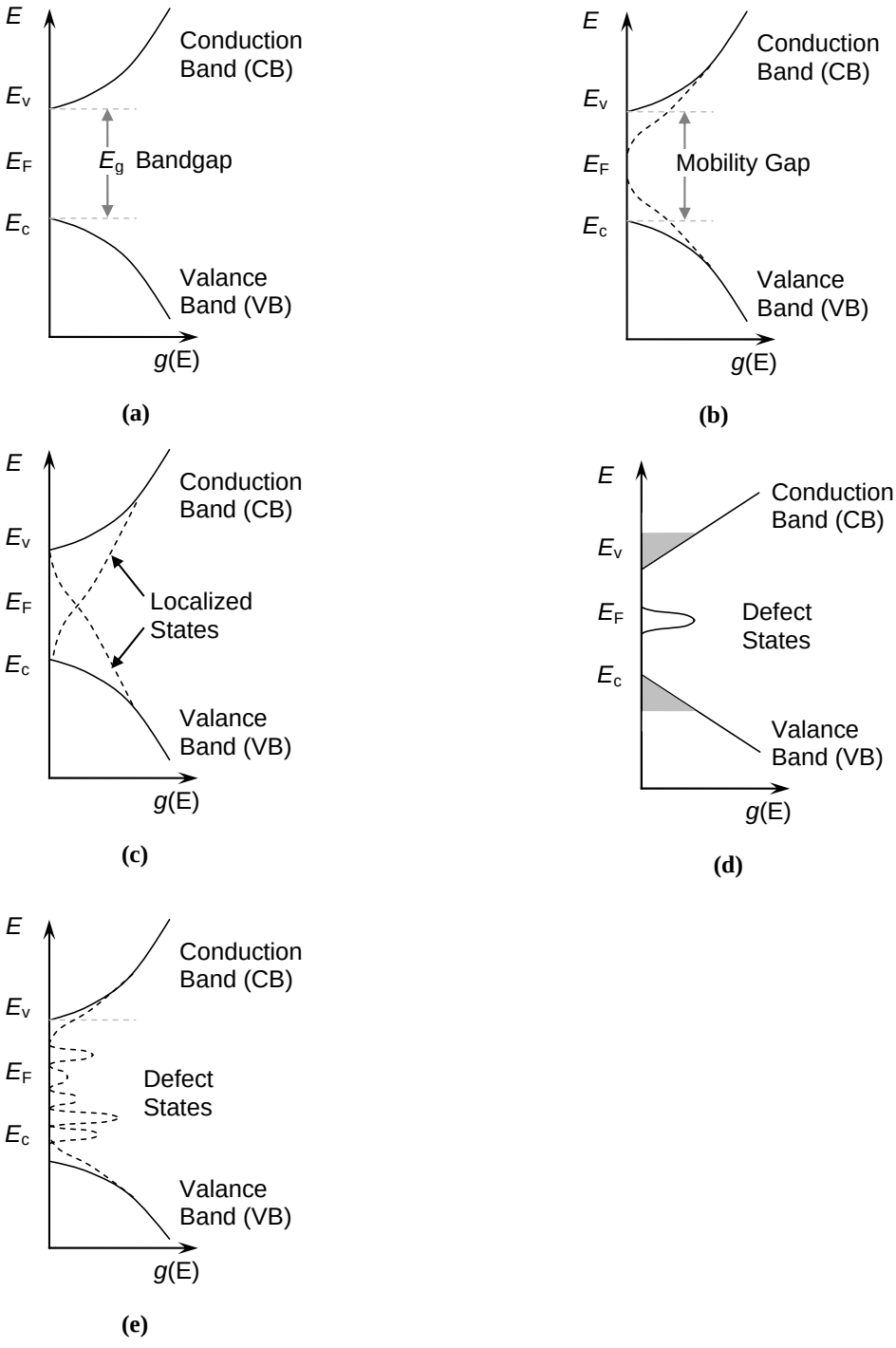

Figure 2.2: Various proposed models for density of states $g(E)$ as a function of energy. (a) DOS model for crystalline semiconductors (b) Mott's model (c) CFO Model (d) Mott and Davis model (e) Marshall and Owen model.

2.4 Structure of Amorphous Selenium

Selenium is an element from the group VI column of the periodic table. The elements in this column are referred to as *chalcogens*. All elements of the chalcogen family have six electrons in their outermost shell and can accommodate up to eight electrons. The outermost shell consists of two subshells, called *s*-type and *p*-type subshells. The *s*-type states can hold two electrons, while *p*-states have six allowed states. Selenium has atomic number Z = 34, implying that it has twenty eight inner core electrons and six valance electrons in the outer most shell. The two *s*-electrons form a lone pair (LP) and do not participate in bonding. The remaining four electrons reside in the *p*-subshell. Two of the four *p*-state electrons usually form a lone pair and are sometimes referred to as non-bonding (NB) states. The remaining two electrons are available for covalent bonding to other atoms. This configuration results in two-fold coordination bonding and has an optimal bond angle of 105° and represents the lowest energy configuration for selenium. Chalcogens generally exhibit divalent bonding and thus form chain-like structures. However, if trigonally bonded atoms, for example those from Group IV or V, are added to the structure, they cross-link with the divalent chains to attain three dimensional stability in the amorphous alloy.

Selenium exists in both crystalline and amorphous form. In the crystalline state, selenium has two major allotropes; monoclinic Se (α-Se) and trigonal Se (γ-Se). The α-monoclinic Se is composed of eight-member (Se_8) rings and γ-Se consists of screw-like spiral chains which run parallel in hexagonal symmetry. γ-Se is more stable at room temperature. It was assumed that the amorphous form of Se would consist of a mixture of the rings and chain formations of trigonal and monoclinic allotropes. However, structural investigation of a-Se and its alloys indicates a "random chain model" with all the atoms in a two-fold coordinated chain structure. The angle between two adjacent bonding planes is defined as the dihedral angle, denoted by ϕ. The concept of dihedral angle ϕ is explained in Figure 2.3 which shows a selenium random chain model. In this example, atoms labeled 1, 2, and 3 form one bonding plane and atoms 2, 3, and 4 from the second bonding plane. The angle between these two planes is the dihedral angle, which is further illustrated in Figure 2.4(b) by looking down the bond that connects atoms 2 and 3. The magnitude of the

dihedral angle ϕ in the random chain model remains constant but its sign changes randomly [25,26].

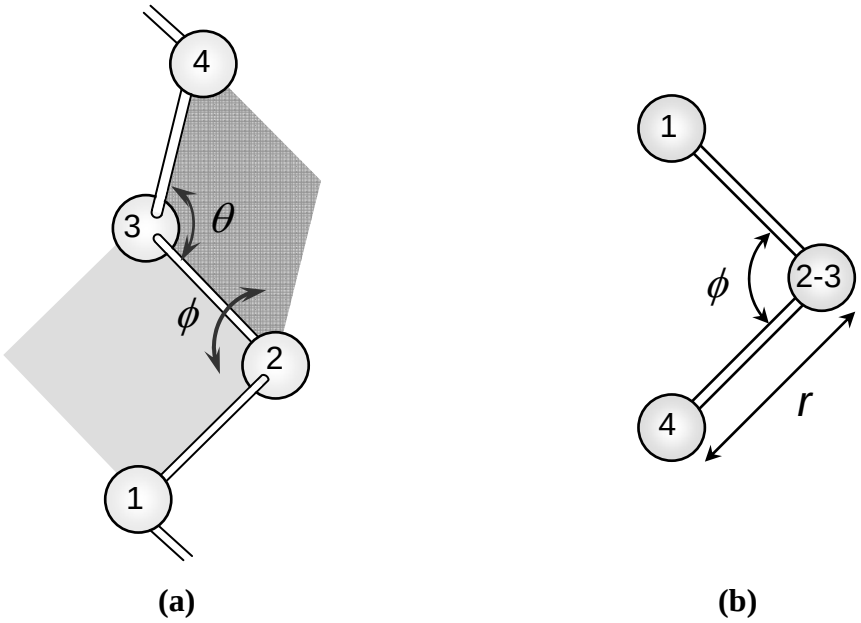

Figure 2.3: Definition of dihedral angle ϕ in selenium random chain model. (a) The definition of dihedral angle formed between two planes of atoms 123 and 234. (b) Looking down on the bond joining atoms 2 and 3 [27].

In the crystalline form, the position of the selenium atoms are fixed by symmetry, the bond length r, and bond angle θ. Therefore, the magnitude of ϕ is a function of bond length r, and bond angle θ. In γ-Se, the dihedral angle rotates in a manner similar to moving along a chain to give a spiral pitch of three atoms, while in α-Se, the dihedral angle alternates its sign as we move along the ring-like structure. In the amorphous form of selenium, the dihedral angle changes its sign randomly, leading to ring-like and chain-like segments. If + or – is used to indicate the relative phase of the dihedral angle ϕ, then a sequence of + – + – represents a ring-like and a sequence of ++++ or – – – – represents a chain-like structure. A structure of amorphous selenium shown in Figure 2.4 can be characterized by +++ – + – + – – –. Only local molecular order within the selenium chain has been assumed in this model and it has been used successfully to explain the vibrational

spectra of a-Se to account for the presence of various Se_8-like spectral features in the infrared absorption and Raman scattering spectra. Other structural studies also support this random chain model [28,29].

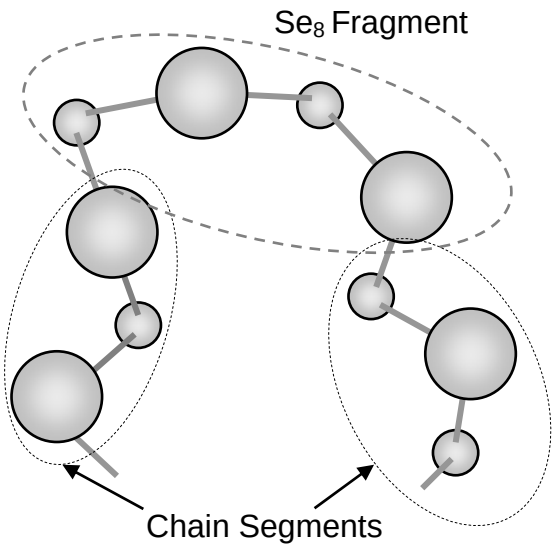

Figure 2.4: Random chain model of amorphous selenium depicting chain-like and ring-like segments [27].

The structure of amorphous solids is not completely random and there is a degree of order at least between the individual atoms. Each individual atom in the solid tends to fulfill its valency requirements, however not all the atoms can satisfy their individual requirements due to lack of periodicity in the amorphous structure. An important property of chalcogenide glasses is that these materials contain thermodynamically derived charged structural defects, called valence alternation pairs (VAP). These defects correspond to some of the chalcogen atoms being over and under coordinated [30,31,32]. Figure 2.5 depicts the bonding configurations possible for a-Se. The first column in the figure consists of notations representing the bonding configurations. In this column, *C* stands for chalcogenides and the subscripts indicate coordination number and the superscripts represent the polarity. The energy of the non-bonding lone pair is taken to be zero. The energy per electron of any bonding orbital σ is taken as $-E_b$ regardless of the nature of the

bond. Since anti-bonding orbitals lie at a slightly higher energy level as compared to the energy depth of the bonding orbitals, the per electron anti-bonding orbital energy is $E_b + \Delta$, where $\Delta > 0$ and is called anti-bonding repulsive energy. Whenever an additional electron is placed on an atom, there is an increase in energy due to electronic correlation U_c. The first state shown in Figure 2.5(a) represents the two-fold coordinated structure, C_2^0 which has overall energy $-2E_b$. In this configuration two of the *p*-state electrons form a lone pair (LP) in the non-bonding state, and the rest of the two electrons reside in bonding states. The next lowest energy configuration is trigonally coordinated atom, C_3^0 shown in Figure 2.5(d). Formation of this type of defect costs the anti-bonding repulsive energyΔ. Another electrically neutral defect is the chain end, represented as C_1^0 in Figure 2.5(b). In this configuration, three *p*-shell electrons are in non-bonding state and one electron is in the bonding state available for bonding. Since this configuration lacks a second bond, this defect costs the system the energy of the second bond.

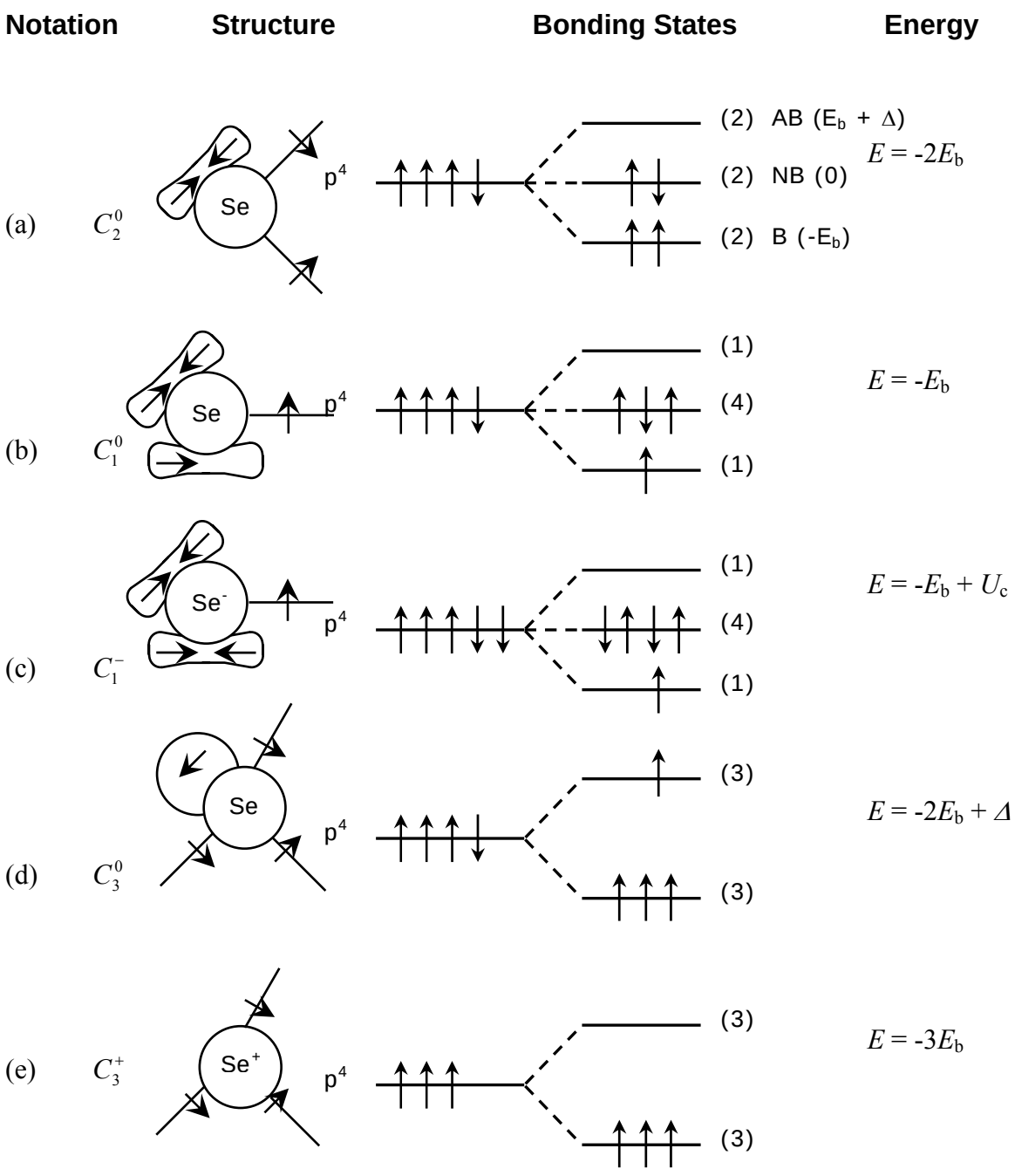

Figure 2.5: Bonding configurations and structure of selenium atoms. Solid straight lines represent boding orbitals, lobes represent lone-pair (non-bonding) orbitals, and circles represent antibonding orbitals (Figure taken from Adler and Yoffa [33]).

Unpaired non-bonding and anti-boding electrons can be detected using experimental techniques. The absence of electronic spin resonance (ESR) signal eliminates the existence of these types of defects in amorphous selenium [34,35]. Kastner, Adler, and Fritzsche [30] studied the absence of ESR signal and proposed that the neutral defect C_3^0 is unstable and would transform into positively and negatively charged centers (VAPs), C_1^- and C_3^+ respectively. The defect generating reaction can be written as

$$2C_2^0 \longrightarrow C_1^- + C_3^+ \qquad (2.1)$$

The one-fold C_1^- and three-fold coordinated C_3^+ defects are shown in the Figure 2.4(c) and (e) respectively. If a pair of these defects is in close proximity, then they are called intimate valence alternation pairs (IVAP). The formation of these under- and over-coordinated atoms is energetically more favorable, as the singly bonded defects are relatively unstable and the total energy of the system is lowered by the transformation provided the electron correlation energy U_c is less than 2Δ. For example, a chain end C_1^0 can lower its energy by approaching the lone pair on a normally coordinated C_2^0 atom and generate an IVAP. The diffusion of the resulting IVAP pair away from each other can further reduce the Gibbs free energy of the solid.

An example of the reaction given by Equation 2.1 is shown in Figure 2.6. A bond between trignonally coordinated defect, C_3^0 and a two-fold coordinated atom, C_2^0 is broken. An electron from a trigonally coordinated atom can be transferred to the singly bonded defect, resulting in an IVAP as shown in the adjacent Figure 2.6(b). The overall material remains neutral despite the presence of large number of positive and negative charged defects. The defect centers C_1^- and C_3^+ are in close proximity to each other, and hence an approaching carrier "sees" IVAP centers as neutral defects.

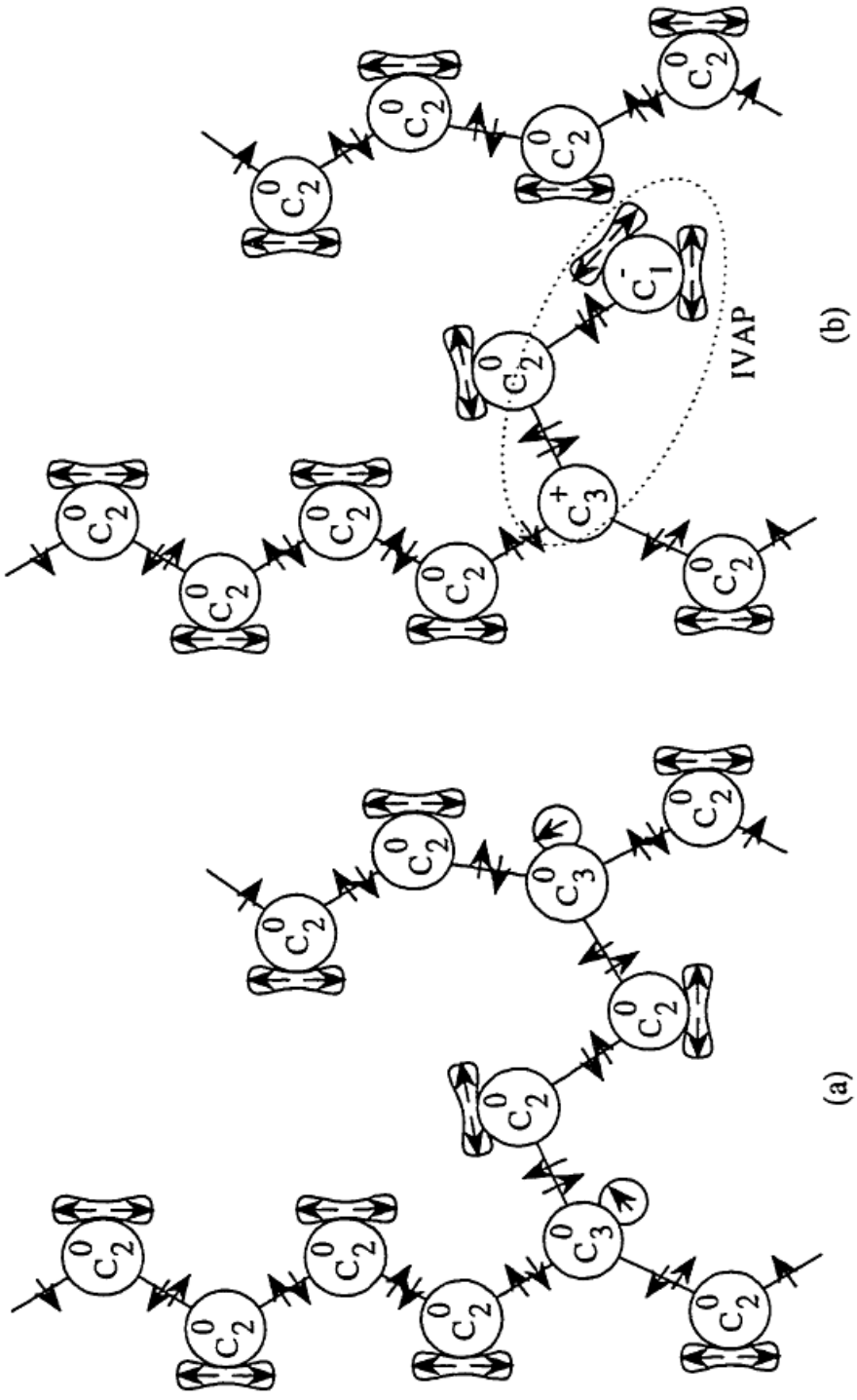

Figure 2.6: In amorphous selenium, (a) C_3^0 defects cross-link the divalent chains and (b) dissolve to form and IVAP.

Many photoelectric properties of a-Se and its alloys can be qualitatively explained by using concepts based on VAP- and IVAP-type defects, and on the inter-conversions between the normally bonded (two-fold coordinated) Se atoms and these defects. The physics of such processes has been extensively discussed in the literature [36,37]. Their existence and the possible defect reactions that can occur in the structure have led to many important predictions and have provided much insight in to the behavior of chalcogenide semiconductors. For example, the linear dependence of the steady state photoconductivity on the light intensity in a-Se has been interpreted via photoinduced IVAP-type centers [38].

2.5 Density of States Model for Amorphous Selenium

The electronic properties of amorphous materials are strongly connected with the DOS distribution in the mobility gap. Even though a-Se has been extensively studied, the exact shape of DOS for a-Se is still surrounded by various uncertainties and controversies. A number of DOS models have been proposed and discussed in the literature [39,40,41,42,43,44,45]. At present, there are at least two general models [46,47,48] which are distinctly different in their DOS distributions; they agree only on the fact that the DOS distribution is not featureless, but contains various peaks as is expected from the Marshall–Owen model of amorphous semiconductors. Within these two DOS models, the number, position, and magnitude of the peaks are still unresolved and are being actively discussed.

A tentative schematic diagram for a-Se is sketched in Figure 2.7. The salient features in the DOS, described by Kasap [49], are discussed here. This DOS distribution is originally based on the model proposed by Abkowitz [46] in 1988 as an extension of the Owen-Marshall DOS model reviewed in the section 2.3. The DOS model is developed through various charge transport and trapping experiments such as transient photoconductivity and electrographic measurements of cycled-up residual and dark discharge. The DOS distribution in the upper half of the mobility gap near the conduction band (CB) edge has been further studied in detail by Koughia et al. [45]. They have studied electron TOF transient photocurrents in stabilized a-Se as a function of electric field, annealing, aging (relaxation), and alloying with As and doping with Cl. The distribution of

localized states in stabilized a-Se has been investigated by comparing the measured and calculated transient photocurrents. The upper part of the DOS shown in Figure 2.7 has been adapted from their findings.

The notable features of this DOS model are a decaying density of localized states from the band edges, with peaks close to the CB edge, called *shallow electron traps*. Over the time scale of typical transit times involved in a-Se applications such as in X-ray imaging, the electron drift mobility μ_e is controlled primarily by these shallow traps at about $\Delta E'_1 = 0.30 - 0.35$ eV below E_c. There is a secondary smaller peak at about $\Delta E'_2 = 0.45 - 0.50$ eV below E_c, and a distribution of deep electron traps at about $\Delta E'_d \approx 1.1\text{-}1.2$ eV below E_c. For the DOS shown here, the mobility gap $E_c - E_v$ is about 2.1 eV wide.

New evidence [50] points to a drift mobility μ_h that is controlled by a monotonically decreasing distribution of tail states near E_v, which explains the field dependence of the activation energy. There is a peak in the DOS at about $\Delta E_2 \approx 0.45$ - 0.50 eV above E_v, and a distribution of deep hole traps at $\Delta E_d = 0.85 - 0.90$ eV above E_v. The Fermi level is about 0.95 – 1 eV above E_v, slightly below midgap (a-Se is *p*-type). $\Delta E'_2$ and ΔE_2 have been proposed to represent the positions of valence alternation pair (VAP) type defects (Se_3^+ and and Se_1^-) in the structure. The concentration of deep traps in a-Se depends on alloying, doping, and aging. The deep states are of particular interest for the X-ray imaging applications. The deep states control the carrier lifetimes, or trapping times, and thus determine the carrier shubweg controlling X-ray photoconductor sensitivity. The nature and the exact origin of the shallow traps at $\Delta E'_1$ and the deep traps at $\Delta E'_d$ from E_c and ΔE_d from E_v have not yet been fully resolved. Two different peaks have been shown in Figure 2.7 for electron and hole traps above and below E_F based on the discharge of the saturated cycled-up Xerographic potential [51] and cycled time-of-flight experiments [52].

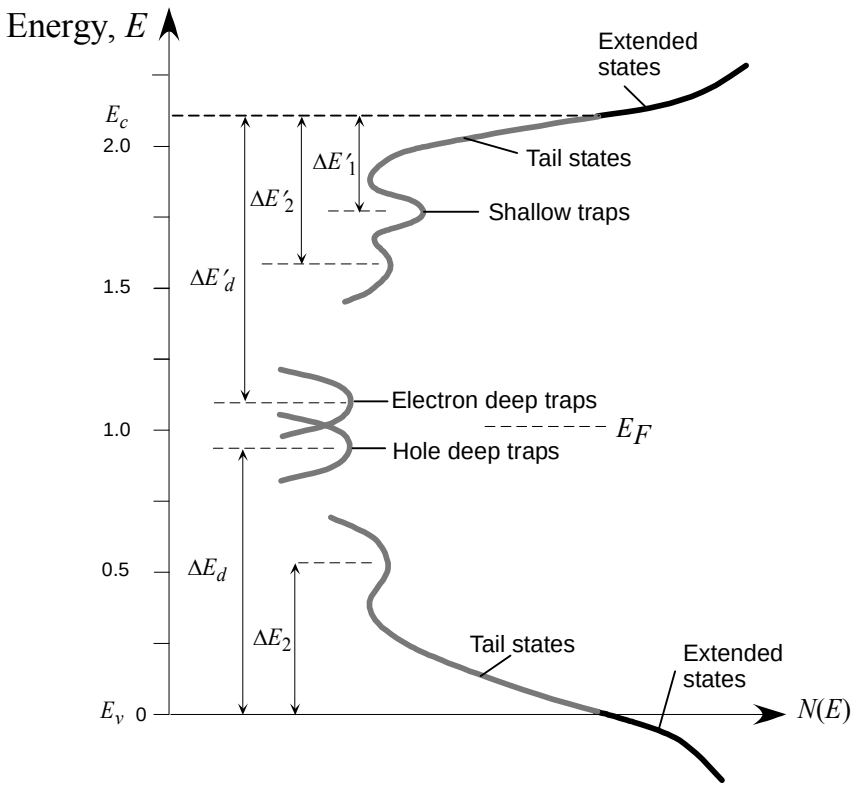

Figure 2.7: A tentative schematic density of states for a-Se [49]

The effects of impurities and alloying elements on the transport properties of a-Se have been extensively studied in the literature. Selenium in its pure amorphous form is unstable and crystallizes over time. The rate of crystallization depends on the ambient conditions [53]. In order to control the crystallization process, small amounts of As (0.2%-0.5%) is alloyed with a-Se. Trivalent As atoms are triply bonded and link with Se chains which increases the viscosity of the amorphous structure and prevents crystallization. One drawback of adding As is that it increases the number of VAP defects that act as hole traps, resulting in the decrease of hole lifetime. This can be compensated by adding a halogen (e.g. Cl) in the parts per million (ppm) range.

A thermally stable film with good hole and electron transport is therefore achieved by adjusting the amount of As and Cl in order to balance the number of VAP defects that lead to carrier traps. The resulting material is called stabilized a-Se, and the nominal composition is indicated, for example, as a-Se:0.3%As +20ppm Cl. The compensation

effects of As and Cl on the charge transport properties of a-Se photoconductors are currently being studied as there are fundamental issues that have yet to be fully resolved [35, 43]. Koughia et. al. [45] have investigated the influence of doping, aging, annealing, and substrate temperature on the density of localized states distribution near CB edge. They have concluded that doping with Cl does not affect the amplitudes of the first and second peaks at $\Delta E'_1$ and $\Delta E'_2$ respectively while the concentration of deep states increases dramatically. Alloying with As reduces the density of deep states and seems to increase the amplitude of first and second peaks. For the effects of aging on the DOS, they concluded that it substantially reduces the deep states density and the amplitude of the second peak while the amplitude of the first peak remains practically unchanged. They interpreted the results in terms of thermodynamic and intrinsic structural defects in the chalcogenide glass structure.

The other generalized model for the DOS is based on the results from experiments based on post-transit transient photoconductivity techniques [40,42,43,44]. The results from these experiments suggest that the peaks in the densities of the shallow traps occur at 0.55 eV below the CB edge and 0.40 eV above the VB edge. The carrier mobility in this case is thus determined by a distribution of shallow localized states that extends over an energy range ΔE from the band edges. The distributions of the deep states are not accessible within the limits of the post transient photocurrent experiment, and are, therefore, not defined by this model.

2.6 Carrier Transport Processes in Amorphous Semiconductors

Carrier transport in crystalline semiconductors always involves motion in extended states, except for the cases with extremely high doping levels or at very low temperatures. Electrons travel in the CB and holes can travel in the VB. Free electrons and holes travel in the extended states under the influence of an electric field. In the absence of some external source of excitation such as X-rays or light, random thermal vibrations of the crystalline lattice create electrons and holes. If these vibrations acquire sufficient energy, they can

excite electrons from the VB into the CB. Alternatively, photons with energy $h\upsilon > E_g$ can also excite the electrons across the bandgap.

Localized states in the mobility gap of amorphous materials have a profound effect on the carrier transport process and thus on electronic properties of these materials. Considering the band structure of the form shown in Figure 2.2(c), a number of carrier transport processes are possible. First we consider the states above E_c, which in the corresponding crystalline materials lie well within the conduction band. Only electron mobility is discussed in this section but the arguments are equally valid for holes after proper modification in terminology and carrier parameters. The effect of random potentials and varying interatomic distances is comparatively low in these states. The mean free path is considerably longer than average interatomic distances and carrier transport is interrupted by occasional scattering. Applying considerations of conventional band theory, the predicted minimum value of mobility for electrons in these states is 100 $cm^2V^{-1}s^{-1}$[2].

For mobilities less than 100 $cm^2V^{-1}s^{-1}$ the mean free path between two scattering events becomes less than de Broglie wavelength of the electron and for mobilities smaller than 10 $cm^2V^{-1}s^{-1}$, the mean free path is less than the interatomic spacing. In the extended states just above the mobility gap of the material, effects of the disorder dominate the charge transport process to the extent that it can no longer be considered band motion with occasional scattering. Cohen described the motion in these states as a diffusive motion similar to the Brownian motion of dust particles in a gas. He estimated the mobility in these states to be of the order of 1 $cm^2V^{-1}s^{-1}$ [54].

In amorphous semiconductors, a high density of defect states results in localization at energies below E_c. Conduction in these localized states can still occur by direct tunneling between localized states as if the carriers "hop" from one localized state to another. The mobility of such phonon assisted "hoping" transport has been estimated by Mott and Davis [55] as

$$\mu_h \approx e\nu_{ph}\frac{\overline{R}^2}{6kT}\exp\left(-2\frac{\overline{R}}{R_0}\right)\exp\left(-\frac{W}{kT}\right) \qquad (2.3)$$

where ν_{ph} is the attempt to hop frequency of the order 10^{12} – 10^{13} Hz, $\bar{R}$ is the mean separation between neighboring sites, R_0 is the localization radius of the centers.. The term ν_{ph} exp (-W/kT) represents the probability per second that the localized electron hops up to a new site, at energy difference W. Equation 2.3 predicts drift mobility in the range of ~10^{-2} $cm^2V^{-1}s^{-1}$ or less at room temperature. This sharp decrease in mobilities near E_c and E_v defines the mobility edge of the non-crystalline solids.

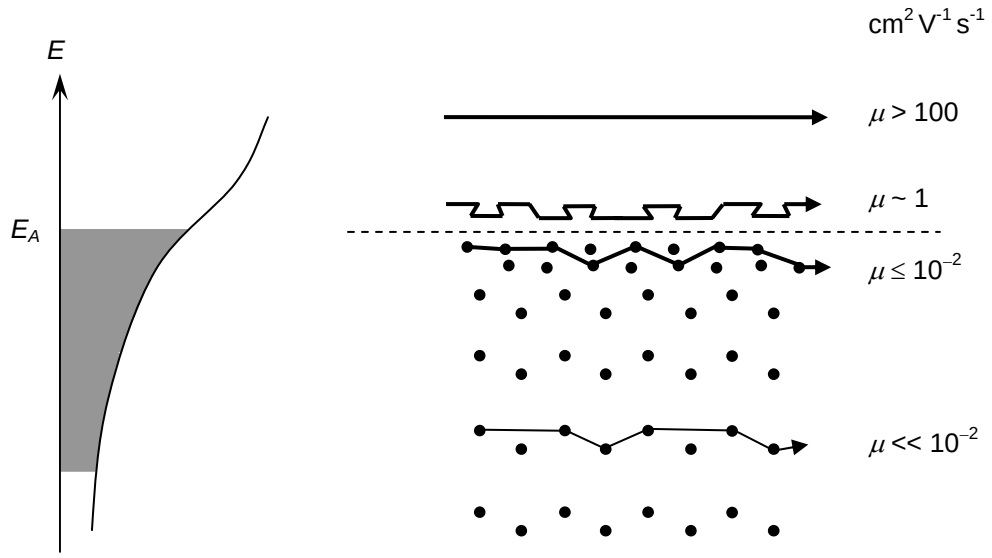

Figure 2.8: Variation in charge carrier mobility with energy for disordered semiconductors [2]

In materials like a-Se with a large number of disorder induced localized states, the microscopic mobility μ_0 is modulated by the traps that lie at lower energy levels below the conduction levels. The localized states that are located near the band edges act as trapping centers that remove the carriers from the transport bands. Carrier transport process across these materials is interrupted at regular intervals by trapping and release events due to these *shallow* traps. The effective drift mobility of the carriers thus decreases due to the time spent immobilized by the carrier in the traps. These traps are characterized by their capture and release time. If τ_c is the mean time the carriers is free and τ_r is the mean time spent by the carrier in the trap then the microscopic drift mobility of the carriers reduced by a

factor $\tau_c/(\tau_c+\tau_r)$. This type of conduction mechanism is called *trap-controlled* or *trap-limited transport*. The theory of trap-limited transport is further discussed in Chapter 3. The probability that a carrier will be captured is given by

$$\frac{1}{\tau_c} = N_t C_t \tag{2.4}$$

where N_t is the density of traps and C_t is the capture coefficient which depends on the species of the traps. Equation 2.4 implies that the capture lifetime is inversely proportional to the trap density. Charge carriers after getting captured in a trap can be re-emitted by a number of mechanisms. Re-emission from a Coulombic trap is a thermally activated process and the probability of the re-emission is given by the Boltzmann statistics as

$$\frac{1}{\tau_r} = \nu_{ph} \exp\left(-\frac{E_t}{kT}\right) \tag{2.5}$$

where ν_{ph} is the attempt-to-escape frequency and E_t is the depth of the trap below the CB edge on the energy scale. Release from the shallow traps is much faster than from deeper traps.

The probability of re-emission from the trap increases by application of an electric field. The electric field applied reduces the potential barrier in a Coulomb-attractive trap through the Poole-Frenkel effect. The Poole-Frenkel effect decreases the potential barrier E_t by an amount δE, which is given by the expression

$$\delta E = \beta\sqrt{F} \tag{2.6}$$

where β is the Poole-Frenkel constant and F is the magnitude of the applied electric field. Since the potential energy barrier is lowered, the equation for the probability must be modified to take into account this effect, and hence Equation 2.2 becomes

$$\frac{1}{\tau_r} = \nu_{ph} \exp\left(-\frac{E_t - \beta\sqrt{F}}{kT}\right) \tag{2.7}$$

The shallow trap release time is very short. For the time scale of experiments like TOF photoconductivity, carriers may experience capture and release numerous times while traversing a solid. The release time from deep traps is very large and the carriers may be permanently removed from the transport band for the timescale of a typical TOF experiment.

For a-Se the peaks close to the CB edge at $\Delta E'_1 = 0.30 – 0.35$ eV below E_c (shown in Figure 2.7) primarily controls the electron drift mobility μ_e. Electron drift mobility μ_e is thermally activated with an activation energy $\Delta E'_1$, and the measured activation energy is relatively field independent as borne out by experiments. The hole drift mobility μ_h is also thermally activated but with an activation energy that depends on the field [49].

2.7 Summary

In this chapter, the structure and electronic properties of amorphous selenium were discussed. The atomic arrangement in amorphous semiconductors is not completely random and has short-range order. The variations in the periodic lattice structure tend to dissolve the sharp band edges in the DOS diagrams and are replaced by tail states extending in the *mobility gap*. Various band models proposed for amorphous materials over time by different researchers were also discussed briefly.

The disorder in amorphous solids is believed to give rise to certain states that are localized in space in the mobility gap of the DOS model. In amorphous selenium, these states are recognized to be the consequence of thermodynamically derived charged structural defects, called valence alternation pairs (VAP). Research has shown that atoms in amorphous selenium exist in a two-fold coordinated random chain structure. The VAPs correspond to some of the chalcogen atoms being over and under coordinated. These defects result in the localized states in the mobility gap and hence control the electronic properties of amorphous selenium.

Charge transport in amorphous selenium is possible through a number of processes. Charge transport studies have suggested that the dominant transport process in a-Se is

diffusive type transport in the extended states near the mobility edge. The carrier transport is further modulated by the shallow traps near the mobility edge. The trapping and release events in these shallow traps reduce the drift mobility of charge carriers.

3 Time-of-Flight and Transient Trap Limited Transport

3.1 Introduction

One of the main driving forces in research of amorphous and microcrystalline semiconductors is that these materials can be economically fabricated into large-area devices required in applications such as displays, scanners, solar cells, image sensors, position sensors, and similar applications. Understanding the electronic conduction in these materials is therefore important for the successful use of these materials in commercial applications. Because of the mathematical complexities inherent in dealing with non-periodic atomic structures of amorphous materials, experimental measurements are required for characterization of these materials. The results of these experiments can be used to investigate the nature of electronic transport in such materials. Some of the charge transport and trapping experiments are Xerographic discharge, time-of-flight (TOF) and post-transit photocurrent analysis. Among these techniques, time-of-flight (TOF) photoconductivity technique is the most widely used method of investigation of charge transport in low mobility solids. It involves time resolving the motion of charge carriers that are generated by step excitation. The transient current waveforms thus obtained display features which are characteristic of the transport mechanism of the carriers in the material.

In the previous chapter the atomic and bonding structure of amorphous selenium, was discussed. In this chapter the principles and theories involved in investigating and interpreting transient conduction in solids will be reviewed.

3.2 General Principles of the TOF Technique

The term "time-of-flight" is now widely used to describe what is essentially a drift mobility experiment. Other terms used in the literature for the TOF technique are *Transient Charge Technique* (TCT) and *Transient Photoconductivity* (TP) technique. A simplified schematic of a TOF experimental setup is illustrated in Figure 3.1. A thin film of highly resistive material of thickness L is sandwiched between two electrodes A and B. The electrodes A and B are blocking electrodes, used in order to prevent charge carrier injection from the electrodes into the sample. The top electrode, A, is connected to a voltage source V_0 that creates a uniform electric field across the sample. The bottom electrode B is earthed through a sampling resistor R. A short pulse of strongly absorbed radiation through electrode A is used to generate a thin sheet of electron hole pairs (EHPs) near the surface of the sample. The wavelength of radiation is selected so that the absorption depth, δ, of excitation is small compared to the sample thickness L. For the biasing connection shown in the Figure 3.1, the photogenerated electrons will be collected by the electrode A, immediately after irradiation. The holes will drift across the sample under the influence of electric field towards the bottom electrode inducing a transient photocurrent through the sampling resistor R. From the shape of the induced current pulse, information pertaining to carrier transport, trapping and release kinetics can be determined. Electron transport can also be examined simply by reversing the polarity of the applied bias voltage.

The preconditions required for a TOF experiment that must be sustained throughout the experiment are as follows:

1. Absorption depth of the incident radiation must be significantly less than the sample thickness i.e. $\delta << L$.
2. Duration of excitation (t_{ex}) should be small compared to the transit time of the carriers i.e. $t_{ex} << t_T$.
3. Transit time of the carriers through the sample should be small compared to the dielectric relaxation time τ_{relax} of the specimen i.e. $t_T << \tau_{relax}$.
4. Small signal conditions should be maintained in the sample for the duration of experiment.

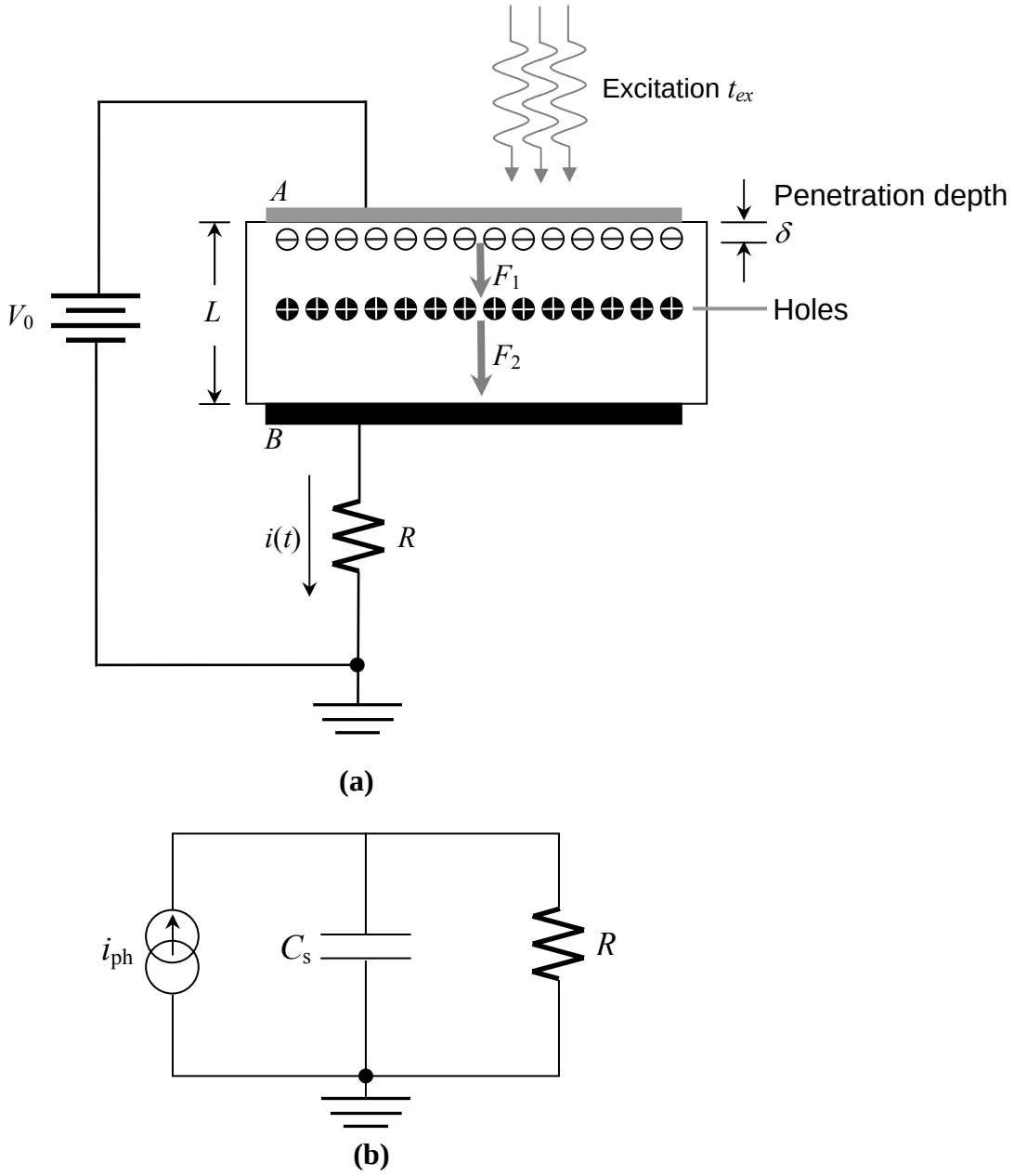

Figure 3.1: (a) Simplified illustration of TOF transient photoconductivity technique experimental setup (b) Small signal AC equivalent circuit

As mentioned in the preconditions, the incident photons must be absorbed close to the surface of the electrode so that the EHPs are generated near top electrode. Furthermore,

the duration of excitation, t_{ex}, should be kept small as compared to the transit time of the carriers through the sample. These conditions are ensured in order to avoid the bulk generation of the charge carriers in the sample. The duration of excitation t_{ex} and absorption depth δ determines the width of the sheet of carriers photogenerated. The sheet of carriers is used here as a probe in order to examine the charge transport through trapping and release events as the carriers drift across the sample, therefore the width of this sheet will determine the spatial resolution of the measurement. On the other hand, if the absorption depth of the excitation is too small, the generated carriers will be trapped by the surface defects and carriers will not contribute to the transient current. The time required for excess charge carriers in the material to reach thermal equilibrium through relaxation and recombination processes is known as the *dielectric relaxation time* denoted by τ_{relax}. Semiconductors with lifetimes greater than τ_{relax} are generally referred to as *lifetime* semiconductors, and the ones with lifetimes shorter than τ_{relax} are called *relaxation* semiconductors. One of the requirements of the TOF experiment stated above was that transit time t_T of the carriers should be considerably smaller than τ_{relax}. In order to effectively study the nature of traps within the material, the photoinjected carriers must not recombine with carriers of opposite charge before they traverse the sample. The number of carriers should decrease through trapping process only. Materials with very high resistivity, such as amorphous chalcogenide semiconductors, contain very few intrinsic mobile charge carriers at room temperature and hence fall into the category of this relaxation regime. Consequently, the probability that recombination will reduce the excess photoinjected carrier concentration is practically negligible for chalcogenides.

The electric field due to the sheet of mobile charge carriers in the sample perturbs the applied uniform electric field. Using Gauss's Law and simple electrostatic reasoning the electric fields F_1 and F_2 in front and behind the charge sheet can be determined. For any given position x' in the material, the expressions for fields F_1 and F_2 (shown in Figure 3.1) developed by Spear [56] are given by

$$F_1(x') = \frac{V_0}{L} + \frac{ep_0 w}{\varepsilon}\left(\frac{x'}{L} - 1\right) \tag{3.1}$$

and

$$F_2(x') = \frac{V_0}{L} + \frac{ep_0 w}{\varepsilon}\frac{x'}{L} \tag{3.2}$$

where p_0 is the concentration of holes in the charge sheet, w is the width of the carrier sheet, and ε is the dielectric constant of the specimen. The electric field behind the charge sheet F_1 is reduced and the electric field in front the charge sheet F_2 is enhanced. From the Equations 3.1 and 3.2, it is evident that the internal field is the sum of the applied field term and self-field term from injected charge. If the amount of charge p_0wA, where A is the irradiated area, is kept sufficiently small so that $ep_0w/\varepsilon << V_0/L$, then the electric field can be approximated as $F_1 = F_2 = F_0 = V_0/L$. Hence the number of charge carriers generated in a TOF experiment is restricted by this condition. If a large number of carriers are generated, then the electric field perturbation will become comparable to the applied field. The analysis in this case must take into account the effects of charge carrier on the applied field. Such photocurrent signals are called *space charge perturbed* (SCP) signals.

The photocurrent induced in the external circuit due to the drift of the charge packet in the sample can be estimated using Shockley-Ramo theorem [19]. Consider a sample of highly resistive medium of thickness L sandwiched between two electrodes. A positive charge carrier q photogenerated at position l in the sample will experience force due to the applied electric field $F_0 = V_0/L$. The carrier will drift towards the negative electrode with a constant drift velocity $v_d = \mu F_0$, where μ is the mobility of the carrier in the medium. The force acting on the charge q due to the applied electric field F_0 is qF_0. The time it takes for the carrier to travel the distance from generation point to the collection electrode is called transit time t_T. For the duration of the transit time, current will be induced in the external circuit. As soon as the carrier reaches the other electrode, it is collected and the current drops down to zero.

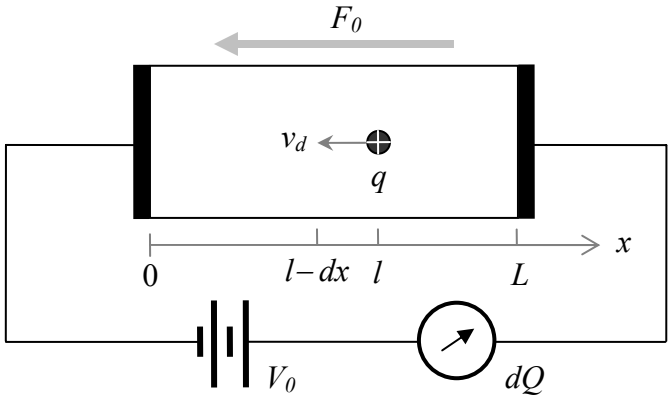

Figure 3.2: The drift of a charge carrier q through dx induces charge to flow in the external circuit.

The amount of work required to move the charge q a distance dx is $qF_0\,dx$, since qF_0 is the force experienced by charge carrier. This work is provided by the connected battery. Therefore the work done dW in moving charge q, a distance dx in time dt is given by

$$dW = q\,F_0\,dx = V\,i_{\mathrm{ph}}(t)\,dt \tag{3.3}$$

The magnitude of the current in the external circuit induced due to drifting charge carriers is therefore

$$i_{\mathrm{ph}}(t) = \begin{cases} \dfrac{qv_{\mathrm{d}}(t)}{L} & 0 < t < t_{\mathrm{t}} \\ 0 & t > t_{\mathrm{t}} \end{cases} \tag{3.4}$$

The equation 3.4 is valid for the case depicted in Figure 3.2 provided small signal conditions are met throughout the TOF experiment. Equation 3.4 can also be expressed in terms of carrier concentration. The total charge due to the injected holes in the TOF experiment is

$$Q_0 = ep_0wA \tag{3.5}$$

where p_0 is the injected hole concentration, w is the width of the charge sheet, and A is the area of this sheet, *i.e.* exposure area. The drift velocity $v_d = \mu V_0/L$ is constant under small signal conditions, so the transit time of the charge sheet is

$$t_t = \frac{L}{v_d} = \frac{L^2}{\mu V_0} \tag{3.6}$$

where μ is the drift mobility of the injected holes in the sample. Hence, the photocurrent in terms of carrier concentration is therefore expressed by

$$i_{ph}(t) = \begin{cases} \dfrac{ep_0 wAv_d(t)}{L} = \dfrac{ep_0 wA}{t_t} & 0 < t < t_t \\ 0 & t > t_t \end{cases} \tag{3.7}$$

There are two possible methods to detect the photocurrent signal, i_{ph}. Small signal ac equivalent of the TOF experimental setup of Figure 3.1(a) is shown in Figure 3.1(b). The combined sample, and stray capacitances due to cables and subsequent signal conditioning electronics are jointly represented by C_s in the equivalent circuit. The photocurrent signal produces a voltage signal that appears across the impedance determined by the parallel combination of R and C_s. If $V(s)$ and $I_{ph}(s)$ are the Laplace transforms of the voltage signal and photocurrent respectively, it can be shown that these two are related through

$$V(s) = \frac{R}{sRC_s + 1} I_{ph}(s). \tag{3.8}$$

This equation has two asymptotic solutions depending on the relative magnitude of the sampling resistor R and the joint capacitance C_s. If the bandwidth of the signal is arbitrarily defined to be the reciprocal of the carrier transit time, and if $RC_s << t_T$, then the inverse Laplace transform of Equation (3.8) yields

$$v(t) \approx R\, i_{ph}(t) \qquad RC_s << t_T. \tag{3.9}$$

Equation 3.9 is called the *I-mode* signal because the magnitude of the observed signal is directly proportional to the photocurrent signal. An ideal I-mode signal rises abruptly upon charge carrier generation, and remains constant until the charge carriers reach the collecting electrode and then abruptly falls down to zero. Alternatively, the other solution of the equation occurs if $RC_s >> t_T$. The inverse Laplace transform of Equation 3.8 becomes

$$v(t) = \begin{cases} \frac{1}{C_s}\frac{ep_0 wA}{t_t}t & 0 < t < t_T \\ \frac{1}{C_s}ep_0 wA & t > t_T \end{cases} \tag{3.10}$$

Simplifying further we have

$$v(t) \approx \frac{1}{C_s}\int_0^\infty i_{ph}(t)dt \qquad \text{for } RC_s >> t_T \tag{3.11}$$

Equation 3.11 is called the *V-mode* signal and is obtained by integrating the expression for I-mode signal. After photogeneration the signal increases linearly with time for the duration the carriers are drifting across the sample. After the carriers reach the collecting electrode, the signal maintains a constant value that is proportional to the total injected charge. Another term used for V-mode signal is *charge transient signal* since it is typically used to measure the total quantity of charge injected into the solid.

Both I-mode and V-mode techniques have distinct advantages. As mentioned above, the V-mode signal is typically used to evaluate the total quantity of charge injected into the specimen from the signal value at saturation. Similarly the I-mode signal abruptly drops down to zero when the carriers reach collecting electrode. From this sharp transition, the transit time of the carriers and hence the carrier mobility in the sample is calculated.

The time dependence of the number of carriers in the material has not been taken into account in the preceding discussion. Amorphous semiconductors have high degree of disorder that results in carrier trapping. This implies that the assumption of constant number of carriers throughout the experiment is not valid for these types of materials. As the charge sheet drifts across the sample the charge carriers get trapped in the localized

states and are immobilized for a certain period of time. The photocurrent signal therefore decays because of the trapping of charge carriers, since the photocurrent is proportional to the number of mobile charge carriers in the sample.

Consider a set of traps located at a discrete energy level in the mobility gap of the semiconductor characterized by a mean trapping time τ_c and release time τ_r. Trapping time is defined as the mean duration a carrier is free before getting trapped and release time is the mean time a carrier resides immobilized in a trap. It is assumed that charge trapping significantly reduces the concentration of free carriers and that charge carrier release time from the traps is considerably larger than the transit time of carrier, i.e. the carrier release is negligible within the time range of the experiment. In this scenario the number of free carriers decays exponentially as the carriers traverse the sample thickness. Equation 3.7 can be modified to take into account the time dependence of the number of carriers

$$i_{\mathrm{ph}} = \frac{ep_0 wA}{t_T} \exp\left(-\frac{t}{\tau_c}\right) \tag{3.12}$$

Using equation 3.6, the I-mode signal now is given by

$$v(t) = \begin{cases} R\dfrac{ep_0 wA}{t_T} \exp\left(-\dfrac{t}{\tau_c}\right) & 0 < t < t_T \\ 0 & t > t_T \end{cases} \tag{3.13}$$

By integrating the above expression, we obtain the expression for V-mode transient signal

$$v(t) = \begin{cases} \dfrac{ep_0 wA\tau_c}{C_s t_T}\left(1 - \exp\left(-\dfrac{t}{\tau_c}\right)\right) & 0 < t < t_T \\ \dfrac{ep_0 wA\tau_c}{C_s t_T}\left(1 - \exp\left(-\dfrac{t}{\tau_c}\right)\right) & t > t_T \end{cases} \tag{3.14}$$

The above equation is called the Hecht [57] relationship which is widely used to estimate the trapping time of the charge carriers. The I-mode and V-mode signal for a trap free material and the one with traps at a discrete energy level are shown in Figure 3.3.

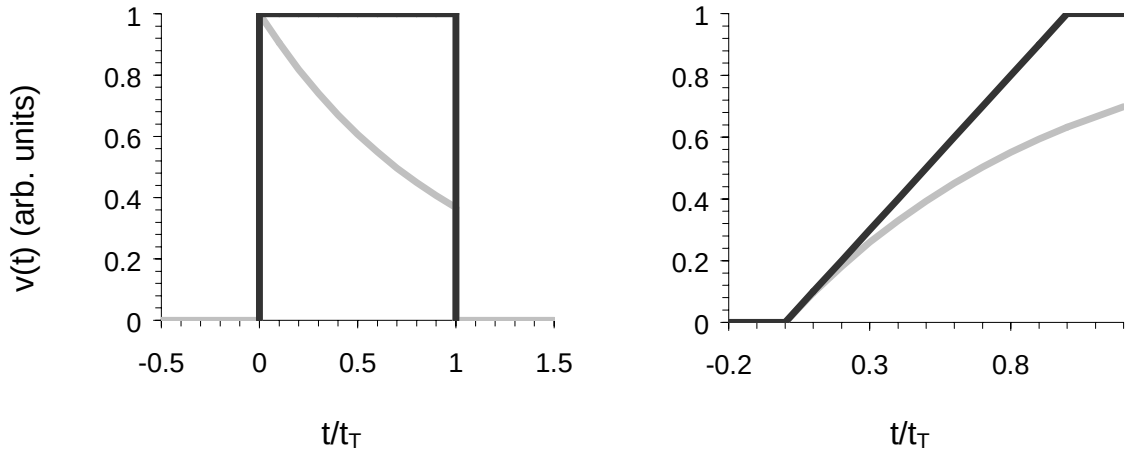

Figure 3.3: Waveforms of (a)I-mode and (b)V-mode signals. The solid lines represent the idealized signal shapes for a sample with no traps and the gray lines represent signals for a sample with a single discrete trapping level.

3.3 Transient Trap-Limited Transport Theory

As discussed in Chapter 2, a large concentration of localized states exists within the mobility gap of amorphous semiconductors which have profound effect on the charge carrier kinematics depending on the relative distribution of these localized states. The localized states act as capture centers for free carriers in the transport band. In this section, the transient trap-limited theory is developed for three cases commonly encountered, a monoenergetic trap distribution, binary trap distribution, and extended trap distribution.

3.3.1 Monoenergetic Trap Distribution

Consider a semiconductor film with a slice of infinitesimal thickness *dx* as shown in Figure 3.4. The current is flowing though the circuit due to hole transport across the sample alone.

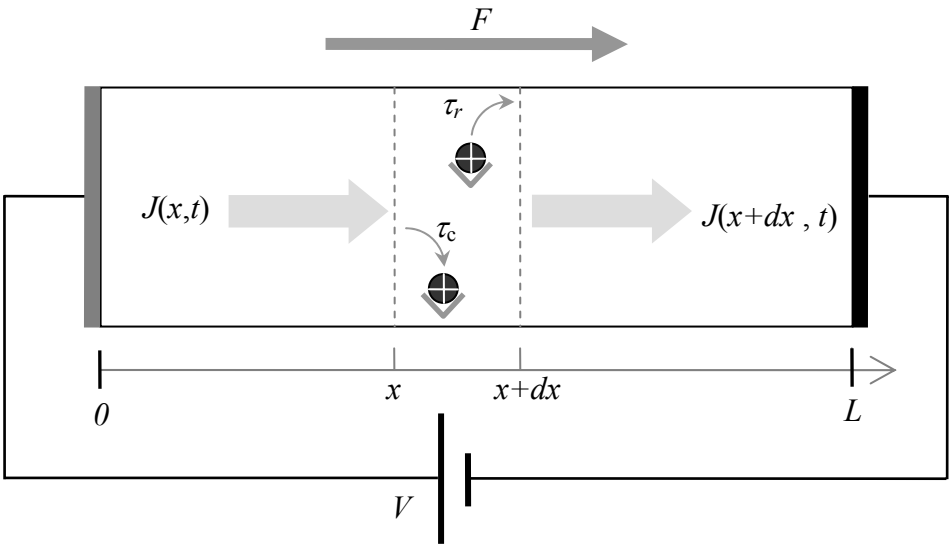

Figure 3.4: Current flow and trapping and release processes in a semiconductor with a single trapping level. The number of holes within a semiconductor slice of thickness *dx* increases due to the flow of holes into the slice and due to the release of trapped holes within the slice.

The number of holes in the slice may increase either due to the net flow of holes into the slice, or a net thermal release of the trapped charge carriers within the slice. The effect of recombination can be ignored since only one type of carrier is present in the sample. The rate of change in the number of free holes in the slice, is therefore expressed as

$$\frac{\partial p(x,t)}{\partial t} = -\frac{1}{e}\frac{\partial J(x,t)}{\partial x} - \frac{\partial p_t(x,t)}{\partial t} \tag{3.15}$$

where e is the charge of electron, $p(x,t)$ is the concentration of the free holes in the sample, $J(x,t)$ is the net current density in the slice and $p_t(x,t)$ is the trapped hole concentration. The current density $J(x,t)$ comprises of two components, one that takes into account the drift of the charge carriers under the influence of applied bias voltage, and the other that is the result of charge carrier diffusion. The conduction current density for holes is expressed as

$$J_c(x,t) = e\,\mu_0\,p(x,t)\,F(x,t) \tag{3.16}$$

where μ_0 is the conductivity mobility, and $F(x,t)$ is the electric field. The spatial variation in the charge carrier concentration results in the diffusion of charge carriers, which results in diffusion current described by the equation

$$J_{\mathrm{D}}(x,t) = -eD\frac{\partial p(x,t)}{\partial x} \tag{3.17}$$

where D is the diffusion coefficient. The total current density is equal to the sum of conduction and diffusion currents, therefore the Equation 3.15 can be expressed as

$$\frac{\partial p(x,t)}{\partial t} = -\mu_0 F(x,t)\frac{\partial p(x,t)}{\partial x} - \mu_0 p(x,t)\frac{F(x,t)}{\partial x} + D\frac{\partial^2 p(x,t)}{\partial x^2} - \frac{\partial p_t(x,t)}{\partial t} \tag{3.18}$$

Equation 3.18 is the one dimensional continuity equation for holes. Similarly, using the same arguments, the one dimensional equation for electron transport can also be derived and is given by

$$\frac{\partial n(x,t)}{\partial t} = \mu_0 F(x,t)\frac{\partial n(x,t)}{\partial x} + \mu_0 n(x,t)\frac{F(x,t)}{\partial x} + D\frac{\partial^2 n(x,t)}{\partial x^2} - \frac{\partial n_t(x,t)}{\partial t} \tag{3.19}$$

where $n(x,t)$ is the instantaneous electron density, and $n_{\mathrm{t}}(x,t)$ is the density of electrons occupying the traps.

Expressions for $\partial p_t(x,t)/\partial t$ and $\partial n_t(x,t)/\partial t$ are called the rate equations for the respective charge carriers and are determined by the difference in the instantaneous trapping and release rates. Given that τ_{c} and τ_{r} are the capture and release times for the charge carriers, expressions for the rate equations for holes and electrons respectively can be written as

$$\frac{\partial p_t(x,t)}{\partial t} = \frac{p(x,t)}{\tau_c} - \frac{p_t(x,t)}{\tau_r} \tag{3.20}$$

and

$$\frac{\partial n_t(x,t)}{\partial t} = \frac{n(x,t)}{\tau_c} - \frac{n_t(x,t)}{\tau_r} \tag{3.21}$$

In order to simplify our solution of the continuity equations, some simplifying assumptions can be made. For example, if small signal conditions are considered for TOF investigations, then the electric field can be assumed to be uniform throughout the sample. This implies that for a carrier at position x at time t, the $\partial F(x,t)/\partial x$ term in the continuity equation can neglected. Also the magnitude of diffusion current is considerably less than the conduction current, therefore the diffusion terms are also neglected.

Equations 3.18 and 3.20 are solved utilizing some boundary conditions. First consider that a short excitation pulse generated P_0 carriers at time $t = 0$ and at position $x = 0$. The distribution of the carriers generated at $t = 0$ is approximated to be a delta function, i.e.

$$p(x,0) = P_0\delta(x,0) \tag{3.22}$$

Since holes are generated at $t = 0$, the concentration of trapped carriers is zero, i.e.

$$p_t(x,0) = 0 \text{ for } x > 0. \tag{3.23}$$

After generation the carriers traverse the sample thickness, until they reach the opposite electrode where they are collected. Therefore

$$p(x,t) = 0 \text{ for } x > L. \tag{3.24}$$

Since there are no carriers trapped beyond the sample thickness, hence

$$p_t(x,t) = 0 \text{ for } x > L. \tag{3.25}$$

Equations 3.18 and 3.20 have been solved simultaneously by Zanio and Akutagawa [58] using the boundary equations stated above and Laplace transform techniques. The expression obtained for the free hole charge density is given by

$$p(x,t) = \frac{P_0}{\mu_0 F}\exp\left(-\frac{z}{\tau_c}\right)\delta(t-z) + \frac{P_0}{\mu_0 F}\exp\left(-\frac{z}{\tau_c} - \frac{(t-z)}{\tau_r}\right)\frac{\xi}{2}\cdot\frac{I_1(\xi)}{(t-z)}U(t-z) \tag{3.26}$$

Here $z = x / \mu_0 F$, $I_1(\xi)$ is the first order hyperbolic Bessel function, $U(x)$ is the unit step function, and $\xi = (2\sqrt{\tau_c z(t-z)/\tau_r})/\tau_c$. The solution obtained is the sum of two components. The first part of the expression represents the charge remaining in the injected carrier packet as it is drifting across the sample. These charge carriers have not suffered any delay through trapping. The number of charge carriers in the charge packet decreases exponentially as $\exp(-t / \tau_c)$ until the un-trapped carriers reach the opposite electrode. The second term represents the carriers which have been removed from the charge sheet and at time t are released back into the transport band. These carriers have suffered at least one trapping event; therefore they lag behind the original charge sheet. These carriers will contribute to the photocurrent signal for times greater than the transit time $t_T = L/\mu_0 F$, where μ_0 is the microscopic mobility. A specific solution of Equation 3.26 is depicted in Figure 3.5**.** This figure shows the time sequence plots for the free carrier density as it travels across the length of the sample. For this case the capture time and release time are taken as τ_c = 10 ns and $\tau_r = t_0 = L/\mu_0 F$ = 1 μs. The spreading of the charge carrier distribution as it travels through the sample is due to the random nature of the trapping and release events.

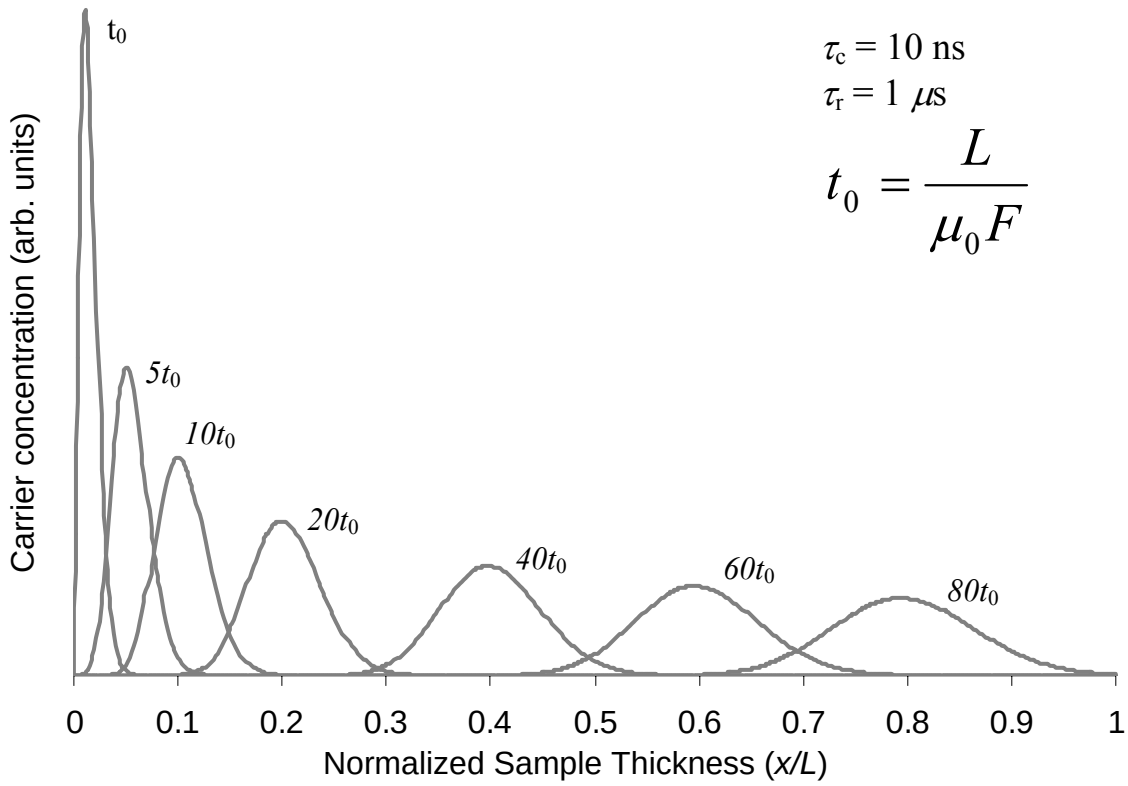

Figure 3.5: Profile of a carrier sheet at various time intervals as it travels through a sample of a semiconductor with one discrete level of traps. The plot is obtained by plotting Zanio's expression for the parameters shown in the inset of the figure.

The time dependence of the total number of free carriers can be obtained by integrating Equation 3.26 over the sample length. The resulting expression can be used to obtain an expression for the I-mode transient current response in a medium with a single discrete level of traps. Explicit expressions for the time dependence of mobile charge carriers and I-mode current response are cumbersome to handle. Therefore particular cases are treated to evaluate trapping parameters. This fact does not in practice limit the use of these expressions for predicting the transient response of the charge carriers since appropriate choice of sample thickness, operating voltage and temperature will help us meet these requirements. In the following section low and high field conditions are studied to determine expressions for I-mode current response for these limiting cases.

3.3.1.1 Low Fields

For the low applied field case, it is assumed that the capture time; the average time a carrier is free before getting trapped, is considerably shorter than the carrier transit time. It is also assumed that the release time; the average time the carrier is immobilized in the trap before being released, is comparable to the transit time i.e. $\tau_c << L/\mu_0 F \approx \tau_r$. These conditions imply that the carriers will undergo many capture and release events through its travel across the sample to the collecting electrode. Since the carrier release time is comparable to the transit time, the time derivative of the free carrier density in Equation 3.18 and Equation 3.20 will vanish over the time interval. In other words the number of free carriers in the transport band will eventually reach a steady state value. Using the principle of conservation of charge, the number of free charge carriers is related to the total number of injected charge carriers by the relation

$$N = N_0 \frac{\tau_c}{\tau_c + \tau_r} \tag{3.27}$$

Substituting this expression in Equation 3.7, the following expression for the I-mode transient signal is obtained.

$$i_{ph} = \frac{eN_0\mu_0 F}{L}\left(\frac{\tau_c}{\tau_c + \tau_r}\right) = \frac{eN_0\mu F}{L} \quad \text{for} \quad \tau_c < t < \frac{\tau_c + \tau_r}{\tau_c}\frac{L}{\mu_0 F} \tag{3.28}$$

This equation is similar to that of trap-free I-mode signal except the transit time has increased by a factor $(\tau_c+\tau_r)/\ \tau_r$ and that the microscopic drift mobility has been reduced from μ_0 to μ and now is given by

$$\mu = \mu_0 \frac{\tau_c}{\tau_c + \tau_r} = \theta\mu_0 \tag{3.29}$$

The carrier motion across the sample is constantly interrupted by the trapping mechanism which reduces the effective mobility of the carrier in the medium. This type of

transport mechanism is referred to as *shallow trap-controlled transport*. In the above equation the factor θ, by which the mobility is reduced is called the shallow trap-controlled transport factor. The equation we obtained is by neglecting the time derivative of the free and trapped charge carrier. The drawback for using this technique is that an analytical expression cannot be obtained to depict the spreading of the charge sheet as evident by the long photocurrent tails in TOF experiments. The spreading of the charge packet is due to the stochastic nature of trapping and release events, which have a much stronger spreading effect than from a simple diffusion mechanism.

3.3.1.2 High Fields

The transit time of the carrier through the sample is related to the applied electric field via the relation $t_T = L/(\mu_0 F)$. If the magnitude of the electric field is sufficiently high, the transit time of the carrier can be considerably smaller than the mean capture time of the carrier in the sample, i.e. $L/(\mu_0 F) << \tau_c$. In this case the carrier may travel the sample thickness without getting trapped. Martini and co-workers [59] derived the expressions for photocurrent signal by splitting their analysis for two time intervals i.e. for time below and above transit time $L/(\mu_0 F)$. According to Martini for time $t < L/(\mu_0 F)$ the photocurrent signal is given by

$$i_{\text{ph}} = \frac{eN_0\mu_0 F}{L}\left[\frac{\tau_c}{\tau_c+\tau_r} + \frac{\tau_r}{\tau_c+\tau_r}\exp\left(-\frac{\tau_c+\tau_r}{\tau_c\tau_r}t\right)\right] \quad \text{for } \frac{L}{\mu_0 F} \qquad (3.30)$$

If de-trapping is neglected, i.e. $\tau_r \to \infty$, then the above Equation reduces to the expression for the simple case of deep trapping.

For time above the transit time $t > L/(\mu_0 F)$, the trapped carriers will be released from the traps and the photocurrent beyond t_T is the result of these carriers. Once de-trapped, most of these carriers leave the sample without being trapped since $L/(\mu_0 F) << \tau_c$. The expression for this condition is give by [59]

$$i_{ph}(t) = \frac{1}{2}\frac{eN_0L}{\mu_0 F\tau_c\tau_r}\exp\left(-\frac{t}{\tau_r}\right) \text{ for } t > L/(\mu_0 F) \tag{3.31}$$

From Equations 3.30 and 3.31, it is observed that for the high biasing field, the photocurrent waveform decays slowly until transit time $t_T = L/(\mu_0 F)$, where a step change in the current magnitude is observed. Beyond the transit time, the photocurrent signal decays relatively slowly.

3.3.2 Binary Trap Distribution

In this section, carrier transport theory for a semiconductor model with two discrete trapping levels is analyzed. The two trapping levels are characterized by their capture times, τ_1 and τ_2, and the release times, τ_{r1} and τ_{r2}. Assuming that the injected charge carrier concentration is considerably less than the concentration of the traps at each energy level, the trap-filling effect can be neglected. In order to further simplify the analysis it is assumed that the concentration of trapped carriers increases due to carriers trapped from transport band only. The carrier rate equation (from Equation 3.20) is therefore expressed as

$$\frac{\partial p_{t1}(x,t)}{\partial t} = \frac{p(x,t)}{\tau_1} - \frac{p_{t1}(x,t)}{\tau_{r1}} \tag{3.32}$$

and

$$\frac{\partial p_{t2}(x,t)}{\partial t} = \frac{p(x,t)}{\tau_2} - \frac{p_{t2}(x,t)}{\tau_{r2}}. \tag{3.33}$$

The overall trapped carrier concentration is the sum of the trapped carrier concentrations at both trapping levels, i.e. $p_t(x,t) = p_{t1}(x,t) + p_{t2}(x,t)$. The continuity equation, Equation 3.15 and Equations 3.32 and 3.33 can be solved to obtain the expression for time evolution of charge carrier packet. Blakney and Grunwald [60] developed a solution to this problem, given by

$$j(t) = A\ \exp(-\ \alpha t) + B\ \exp(-\ \beta t) + j_\infty \tag{3.34}$$

where j_∞ represents the steady state current which flows after the charges have come into equilibrium with the trap distributions. The coefficients are related to each other through the following set of equations

$$\alpha + \beta = \frac{1+\theta_1}{\tau_1} + \frac{1+\theta_2}{\tau_2} \tag{3.35}$$

$$\alpha\beta = \frac{\theta_1 + \theta_2(1+\theta_1)}{\tau_1\tau_2} \tag{3.36}$$

$$\alpha A + \beta B = \frac{j_0}{\tau_1} + \frac{j_0}{\tau_2} \tag{3.37}$$

$$A + B + j_\infty = j_0 \tag{3.38}$$

and

$$j_\infty = \frac{j_0\theta_1\theta_2}{\theta_1 + \theta_2(1+\theta_1)} \tag{3.39}$$

where $\theta_1 = \tau_1/\tau_{r1}$ and $\theta_2 = \tau_2/\tau_{r2}$. It is worth mentioning that if one of the trap distribution is so deep such that the thermal release of captured carriers is improbable in time interval equal to the transit time, i.e. $\tau_{r2} \to \infty$, then $\theta_2 = 0$. This condition is the *shallow trap-controlled deep trapping* process commonly used to describe charge transport in amorphous selenium. In this condition the Equation 3.34 reduces to

$$j(t) = A\exp\left(-\frac{t}{\tau_1}\right) + B\exp\left(-\frac{\theta_1 t}{\tau_2}\right) + j_\infty \tag{3.40}$$

The first part of the equation suggests that the current should exhibit an initial exponentially decaying spike until the charge carriers are in equilibrium with the shallow traps followed by a slower decaying exponential curve with a characteristic decay rate given by τ_2/θ_1.

3.3.3 Extended Trap Distribution

Charge transport in semiconductors with monoenergetic and binary trap distributions has been discussed in the preceding sections. A more realistic model, and considerably more complex than the previous models, will be the one with continuous distribution of traps in the mobility gap. The multiple-trapping problem was analyzed by Rudenko and Arkhipov [61] and is reviewed here. Rudenko and Arkhipov addressed this problem by considering a continuous distribution of traps, represented by $N(E)$, distributed in energy E. The total density of traps will be given by

$$N_t = \int_0^\infty N(E)dE \tag{3.41}$$

The overall density of carriers in the sample is the sum of the density of free and trapped carriers written as

$$p(x,t) = p_f(x,t) + p_t(x,t) \tag{3.42}$$

where $p(x,t)$ is the total carrier density, $p_f(x,t)$ is the free carrier density, and $p_t(x,t)$ is the density of trapped carriers. The mean free time between two trapping events, τ depends on a number of material properties. These properties such as capture cross-section $\sigma(E)$ at energy E, the thermal velocity of the carriers v_{th}, and the density of the traps N_t. These parameters are related to the carrier lifetime by the relation

$$\tau = \frac{1}{\sigma(E)\, v_{\text{th}}\, N_t}.$$

The product of the capture cross-section $\sigma(E)$ and thermal velocity v_{th} is defined as the capture coefficient $C(E) = \sigma(E)\, v_{\text{th}}$. The probability per unit time that a free carrier will be captured by a trap of energy from E to $E + dE$ is given by

$$\frac{dE}{\tau(E)} = C(E)\, dN_t = C(E)\, N(E)\, dE \tag{3.43}$$

Carrier release from traps is a thermally activated process. Considering steady-state conditions, the probability of release per unit time for a carrier trapped at energy ΔE below E_c is can be written as

$$\frac{1}{\tau_r(E)} = N_c \cdot C(E) \cdot \exp\left(-\frac{\Delta E}{kT}\right) \tag{3.44}$$

where N_c is the density states at the conduction band edge, and ΔE represents the energy depth below E_c, i.e. $\Delta E = E_c - E$. The density of trapped carriers $p_t(x,t)$ is defined by the expression

$$p_t(x,t) = \int_0^\infty \rho(x,t,E)dE \tag{3.45}$$

where $\rho(x,t,E)$ is the density of trapped carriers in the range from E to $E + dE$. The rate equation for trapped carriers in the energy range from E to $E + dE$ maybe written as

$$\frac{\delta p_t(x,t,E)}{\delta t} = p_f(x,t)\frac{\delta E}{\tau(E)} - \frac{\delta p_t(x,t,E)}{\tau_r} \tag{3.46}$$

or,

$$\frac{\delta E \delta \rho(x,t,E)}{\delta t} = p_f(x,t) \cdot C(E) \cdot N(E) \cdot \delta E - \rho(x,t,E) \cdot \delta E \cdot N_c \cdot C(E) \cdot \exp\left(-\frac{\Delta E}{kT}\right) \tag{3.47}$$

The expression for the rate of change of carrier trapped density can be obtained by rearranging the above expression as follows

$$\frac{\delta \rho(x,t,E)}{\delta t} = C(E)\left[p_f(x,t) \cdot N(E) - \rho(x,t,E) \cdot N_c \cdot \exp\left(-\frac{\Delta E}{kT}\right)\right] \tag{3.48}$$

If thermal equilibrium of charge carriers between the conduction and localized states exists, the time derivatives of Equation 3.48 can be neglected, i.e.

$$\frac{dp_t}{dt} = \frac{d\rho}{dt} = 0 \tag{3.49}$$

Therefore the trapped charge carrier density at energy E may be related to the concentration of free carriers by the expression

$$\rho(x,t,E) = p_f(x,t)\frac{N(E)}{N_c}\exp\left(\frac{\Delta E}{kT}\right) \tag{3.50}$$

Substituting Equation 3.50 in Equation 3.45 will provide the total trapped charge concentration. The total charge concentration is the sum of free and trapped charge carrier concentration therefore

$$p(x,t) = p_f(x,t)\left[1 + \int_0^\infty \frac{N(E)}{N_c}\exp\left(\frac{\Delta E}{kT}\right)dE\right] \tag{3.51}$$

If the trapped controlled transport factor θ is defined as

$$\frac{1}{\theta} = \frac{p_t}{p_f} = \int_0^\infty \frac{N(E)}{N_c}\exp\left(\frac{\Delta E}{kT}\right)dE \tag{3.52}$$

then Equation 3.47 simply reduces to $p_f(x,t) = \theta(x,t)$ since $\theta << 1$.

The one dimensional continuity equation is required to complete the analysis. If the mutual Coulombic repulsion of the carriers is neglected, then the applied electric field F can be considered constant throughout the material. Assuming thermal equilibrium, the continuity equation may be stated as

$$\frac{\delta p(x,t)}{\delta t} + \mu_0 F\frac{\delta p_f(x,t)}{\delta x} - D_0\frac{\delta^2 p_f(x,t)}{\delta x^2} = 0 \tag{3.53}$$

Using the approximation $p_f(x,t) \approx \theta\, p(x,t)$ in Equation 3.49, the following expression is obtained

$$\frac{\delta p(x,t)}{\delta t} + \mu F \frac{\delta p(x,t)}{\delta x} - D \frac{\delta^2 p(x,t)}{\delta x^2} = 0 \qquad (3.54)$$

where $\mu \approx \theta\mu_0$ and $D \approx \theta \ D_0$. It is interesting to note that the reduction in the carrier mobility from μ_0 to μ is similar to the low field condition for the mono-energetic trap distribution. Hence the equations that govern the charge transport process (Equations 3.42, 3.45, 3.48, 3.54) in a semiconductor with continuous distribution have been derived.

It is worth mentioning that one major assumption in the development of Equation 3.54 was that the thermal equilibrium of charge carriers was instantaneously established by eliminating the time dependence in Equation 3.48. However there is a finite time where the concentration of trapped charges varies with time. For this case the continuity Equation 3.54 developed above will be modified as

$$\frac{\delta p(x,t)}{\delta t} + \mu F \frac{\delta p(x,t)}{\delta x} - D_{eff} \frac{\delta^2 p(x,t)}{\delta x^2} = 0 \qquad (3.55)$$

where $D_{eff} = D + D_f$. D_f is known as the field diffusion coefficient which takes into account the field dependence of the diffusion process [18].

3.4 Summary

In this chapter the theory of charge transport a typical TOF photoconductivity experiment is discussed. A TOF photoconductivity experiment is a commonly employed technique used to study charge transport kinematics in low mobility solids. Carriers generated by photoexcitation drift under the influence of an applied electric field to induce current in the external circuit. The photocurrent waveform is used to measure carrier drift mobility in the material and carrier lifetimes. There are two possible methods to detect the photocurrent signal. One is called the I-mode signal because the magnitude of the observed signal is directly proportional to the photocurrent signal and the other is called V-mode signal or *charge transient signal* since it is typically used to measure the total quantity of charge injected into the solid. Transient trap-limited theory is developed in this chapter for three cases commonly encountered, a monoenergetic trap distribution, binary trap distribution, and extended trap distribution. Traps that are located near the mobility edges

are called shallow traps. Carriers are trapped and released from these traps numerous times before they traverse the sample thickness; therefore the transit time of the carrier is prolonged by trapping in these states. The equations governing the charge transport process in these three models are derived.

4 Monte Carlo Model of Transient Trap-limited Transport

4.1 Introduction

Monte Carlo (MC) Simulation has become one of the most widely used techniques for investigating charge transport in amorphous semiconductors. It is a statistical numerical technique that relies on random numbers to simulate the stochastic behavior of elements of the model to calculate the required information. The greatest advantage of this method is the surprising simplicity of the calculations and the fact that it is more directly interpretable from a physical point of view. This method provides us with the possibility to manage very complicated models in which an analytical solution is either nearly impossible or extremely cumbersome. Conversely, the main disadvantage of the MC method is that it is relatively time consuming in terms of computation time, but as the computing price is decreasing, it is becoming more time effective.

The present work is aimed at developing a MC simulation model for carrier transport in a TOF transient photoconductivity experiment to investigate the distribution of localized states in the mobility gap of amorphous selenium. The MC technique, as applied here, consists of simulating the motion of a carrier sheet resulting from photoexcitation inside a sample, subject to the force from the applied electric field and undergoing multiple trapping and release events. The duration of free flight of carriers and their dwell time in the trapping centers are stochastically calculated with the given probabilities of these events. For this research work the MC simulation models were first developed for simpler semiconductor models; with monoenergetic trap distribution and models with traps at three discrete energy levels. The theoretical and analytical solutions proposed by previous

researchers were used to verify our MC modeling approach. After this, the continuous distribution of localized states in the mobility gap of a-Se was then investigated by using it in our calculations of transient photocurrents which are then compared with measured experimental results and with data published elsewhere. In this chapter the MC model developed for the trap distributions at a single energy level and at three discrete energy levels is discussed.

4.2 Random Numbers

Random numbers in Monte Carlo simulation techniques have special significance, since the method itself relies on *chance* or *randomness*. Random numbers produced by computers cannot be strictly classified as random because the manner in which they are produced is completely deterministic and the element of chance is not actually present. Hence the random numbers generated by computers are in fact *pseudo*random numbers. In 1951, Lehmer eloquently described the computer generated random sequence as a vague notion, in which each term is unpredictable to the uninitiated and whose digits pass a certain number of statistical tests. Mathematical software packages such as Matlab, Mathcad etc. available today contain random number generators that when called upon in a program, produce either a single random number or an entire array of random numbers. The random numbers in Matlab are called by using the *rand* function and the computer returns random numbers distributed uniformly in the interval (0, 1). The random number generator in Matlab 5.0 and above uses a lagged Fibonacci generator, with a cache of 32 floating numbers, combined with a shift register random integer generator. Two important features of the *rand* function in Matlab [62] are:

1. The random number generator will generate 2^{1492} ($\sim 10^{449.1368}$) numbers before the sequence will begin to repeat itself.
2. Floating point numbers between the range 2^{-52} and $1 - 2^{-52}$ are generated.

If the purpose of analysis involves transient conditions then it is necessary to simulate the behavior of a large number of carriers and follow their dynamic history of multiple trapping in order to obtain the desired information. The MC model of this research involves

simulating the transport of carriers in a-Se undergoing multiple trapping to calculate transient photocurrents. The period and range of the Matlab generator are quite sufficient for the scope of this research.

4.3 Monoenergetic Trap Distribution Model

The development of the MC simulation model started with the simplest case: semiconductor model of monoenergetic trap distribution. Zanio and Akutagawa [58] solved the problem of carrier transport in a semiconductor with a trap distribution at a single discrete energy and obtained an expression for free carrier density as a function of distance and time. Their solution was used to validate the MC modeling approach for modeling carrier transport undergoing trapping and release events.

In a TOF photoconductivity experiment the carriers are generated by an extremely short but highly absorbed pulse. The incident pulse results in photogeneration of electrons near the surface of the sample. It is assumed that the short excitation pulse is strongly absorbed by the sample resulting in a very thin sheet of charge carriers. Since the number of drifting carriers is assumed to be sufficiently small, the effect of the internal electric field due to the drifting carriers can be neglected and the electric field is assumed to be uniform throughout the sample thickness. As the carriers drift toward the opposite electrode under the influence of the applied electric field, they experience trapping and release. The time of free flight between two successive trapping events and the dwell time in the trap are stochastic events in accordance with the relative probabilities of these events. The mean time of free flight between two trapping events is called the capture time, represented by τ_c. The mean dwelling time of a carrier in a trap is called the release time, denoted by τ_r. The expression obtained by Zanio and Akutagawa for free carriers is given by Equation 3.26.

For our MC model of a TOF experiment, a semiconductor sample of thickness L is considered. Capture and release times are in the order of ~10ns and ~1μs respectively. The carriers drift under the influence of the applied electric field F towards their respective

electrodes. The sheet of carriers spreads out as the carriers experience trapping and release events. The MC model developed here calculates the spatial profile of drifting carrier sheet inside the sample at various time intervals. The different points in time when a *snapshot* of the drifting charge sheet profile is taken are multiples of the free carrier propagation time t_0, i.e. the time it takes for a free carrier to go across the sample thickness without getting trapped $\left(L/\mu_0 F\right)$. The flow chart of the MC model is shown in Figure 4.1. The blocks of the flowchart for electron transport are briefly explained below.

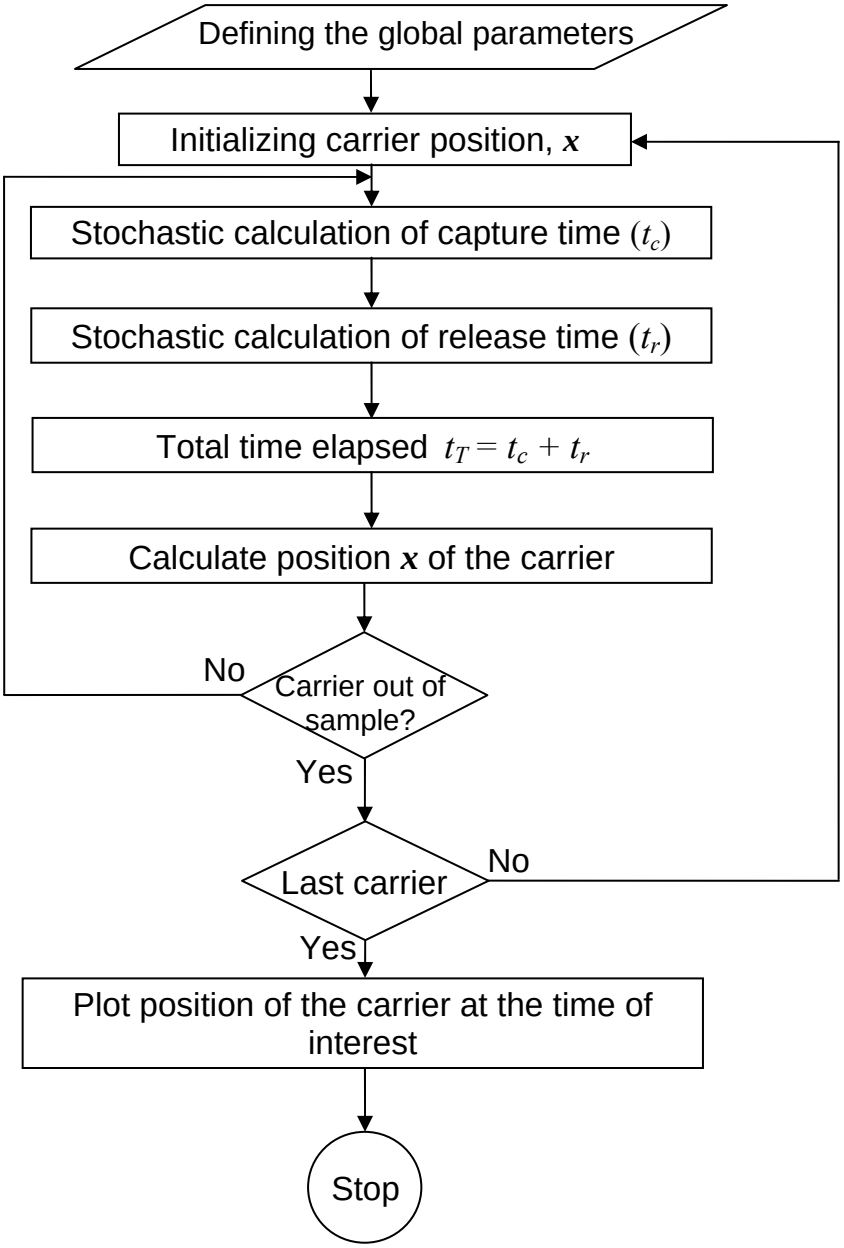

Figure 4.1: Monte Carlo simulation algorithm for semiconductor with monoenergetic trap distribution.

- ***Definition of global parameters***

  The program starts by defining the physical system of the experimental setup. This includes defining the material parameters such as sample length L, absorption coefficient (α) of the material etc. The relevant experimental parameters such as temperature T and applied electric field F are also defined within this block. Some adjustable parameters that control the simulation process are outlined here as well. For the monoenergetic semiconductor model, these parameters include the number of carriers N_e and the bin size of the histogram. The number of carriers N_e generally used in these simulations is 10^4 carriers. This number of carriers gives the best compromise for this model between statistical noise and computation time. The monoenergetic trap distribution model is a relatively simple model and therefore does not take large computational time, but for more complex models increasing the number of carriers greatly increases the simulation time.

- ***Initializing carrier position, x***

  After defining the global parameters, the starting position of the photogenerated carrier in the sample is initialized. If infinite absorption is considered, then the incident photons generate EHPs near the surface of the sample. The starting position of the entire sheet of carriers can be taken as 0 implying that all carriers are generated in the form of a thin sheet close to the surface of the sample.

- ***Stochastic calculation of capture time (t_c) and release time (t_r)***

  After photogeneration, holes are assumed to be collected promptly by the irradiated electrode. Electrons are the only mobile carriers assumed in this model. The electrons while drifting experience trapping a number of times. The time of "free" flight and the idle time in a trap are both random but are in accordance with the probability of

trapping and release. The capture and release times can be calculated using uniform random numbers from the following expressions

$$t_c = -\tau_c \ln(1 - r) \text{ and} \tag{4.1}$$

$$t_r = -\tau_r \ln(1 - r) \tag{4.2}$$

where τ_c and τ_r are the mean capture and release times respectively and r is a uniform random number between 0 to 1. Since both r and $(1 - r)$ are uniformly distributed between 0 and 1, in order to save computation time the expression (4.1) and (4.2) are modified to

$$t_c = -\tau_c \ln(r) \text{ and} \tag{4.3}$$

$$t_r = -\tau_r \ln(r) \tag{4.4}$$

- ***Total time elapsed*** $\boldsymbol{t_T = t_c + t_r}$

The time elapsed for the duration of events in one loop of the algorithm consists of time of free flight t_c and dwell time t_r in the trap by the carriers. The total time elapsed is calculated by adding the two times and recording it in memory in an array.

- ***Calculate position of the carrier using*** $\boldsymbol{t_c}$

The distance the carrier has been displaced during the free flight before getting trapped can be calculated from the expression

$$\text{Move} = \mu_0 \cdot F \cdot t_c$$

where μ_0 is the drift mobility of the carrier at the mobility edge and F is the applied electric field. The total distance, x, the carrier has traveled in the sample is the sum of all the displacements from the previous iterations. Hence for the i-th iteration the displacement is given by

$$x = \sum_{i=1}^{n} \text{Move}_i$$

- ***Check the position of the carrier within the sample***

  The loop is terminated when the carrier reaches the collecting electrode. This block checks if the carrier's position x is still within the sample thickness. This is done by comparing the total displacement since generation with the sample thickness L. If the condition $x \geq L$, is satisfied then the program comes out of the loop otherwise it goes back to the capture time block for further iterations until this condition is satisfied.

- ***Is this the last carrier***

  After the carrier is out of the sample, it is checked if the carrier under consideration was the last carrier. If the condition is true, the loop is terminated and program proceed to calculations, otherwise the carrier transport from $x = 0$ to $x = L$ is simulated for the remaining carriers.

- ***Plot position of the carrier at the time of interest***

  At this stage the information required to plot the carrier packet position in the sample at a given time is calculated from the arrays of carrier displacement and time history. The data has been recorded for each trapping event. The position of each carrier at the required time is recorded in an array and then sorted in bins to plot the histogram of the carrier concentration versus position in the sample.

MC calculations for a semiconductor sample of thickness L = 100 μm in a TOF experiment are performed. The capture and release times of the monoenergetic trap distribution are taken to be τ_c = 10 ns and τ_r = 1 μs respectively. The applied electric field strength is F = 3 V/μm. An important assumption is that the electric field is not perturbed by the drifting charge sheet and hence remains uniform throughout the sample. The theoretical solution of this particular case is plotted with the MC simulation and is shown in Figure 4.2. The results are in excellent agreement.

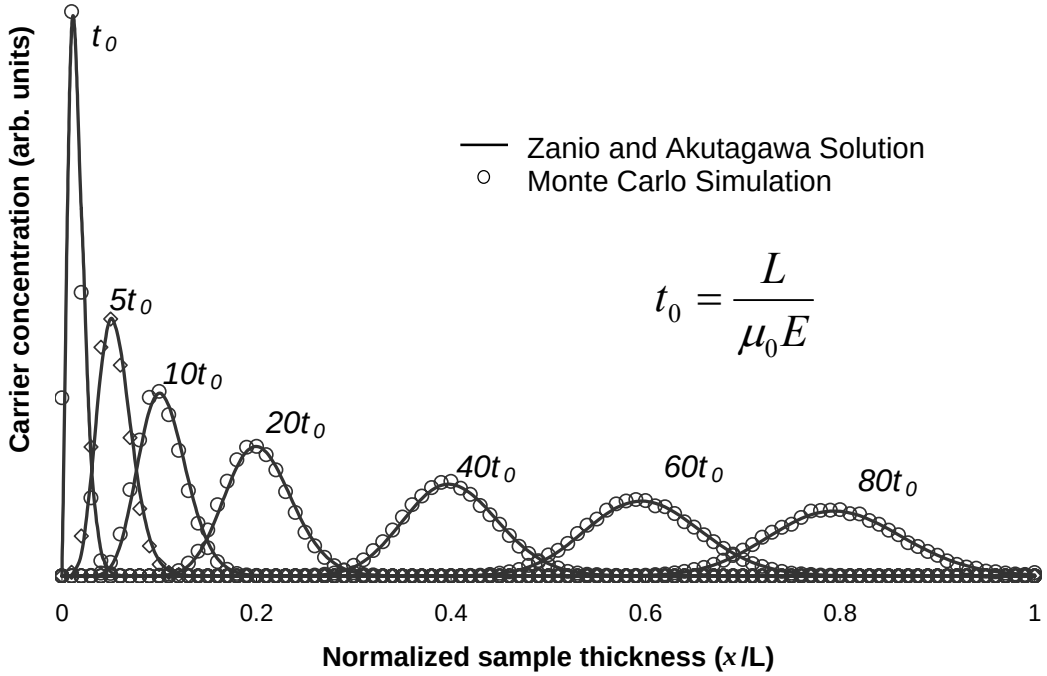

Figure 4.2: Time evolution of the spatial profile of photogenerated carrier sheet in a semiconductor model with mono energetic trap distribution during a TOF experiment.

4.4 Three Levels of Trap Distribution

In this section the Monte Carlo model for a slightly more complex system with three trapping levels is developed. The distribution of localized states in the mobility gap of a semiconductor is represented by three *effective* trapping levels. Similar models consisting of three trapping levels have been proposed by Noolandi [66] and Blakney [60]. The three trapping levels are characterized by their capture and release times as shown in the Figure 4.3. These trapping levels are sometimes referred to as *mobility*, *shallow* and *deep* in literature. The carrier transport generally occurs in the mobility and the shallow level. The carriers trapped in the mobility level are released almost immediately after capture since the release time is very short. The capture and release times for the shallow levels are comparable to the transit time t_T of the carriers and hence almost all the carriers trapped in these levels are released within the time frame of a TOF experiment. Carriers trapped in the

deep states are permanently lost, since the release time is very large and hence they do not contribute further to the transient photocurrent.

The electron transport across the sample is simulated to calculate the TOF photocurrent and compare with waveforms calculated from the inverse Laplace transform technique. The flow chart of the MC model is shown in Figure 4.4, and the blocks are explained below. Some of the blocks function in a similar manner as in the monoenergetic trap model and hence are not elaborated here.

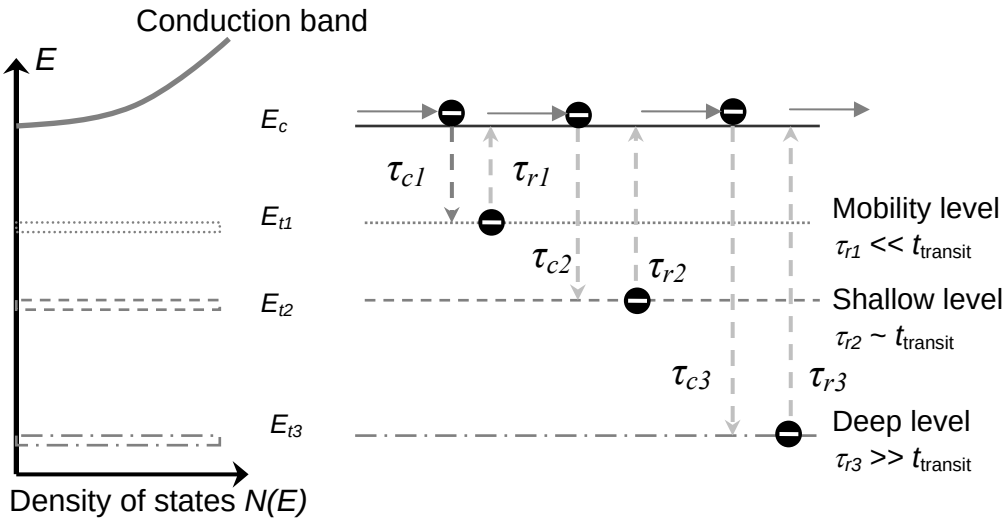

Figure 4.3: Semiconductor model with localized states at three discrete energy levels. Carriers in the mobility level are captured and released almost immediately. The release time for the shallow level is comparable to the transit time. Carriers trapped in deep traps are considered to be permanently lost.

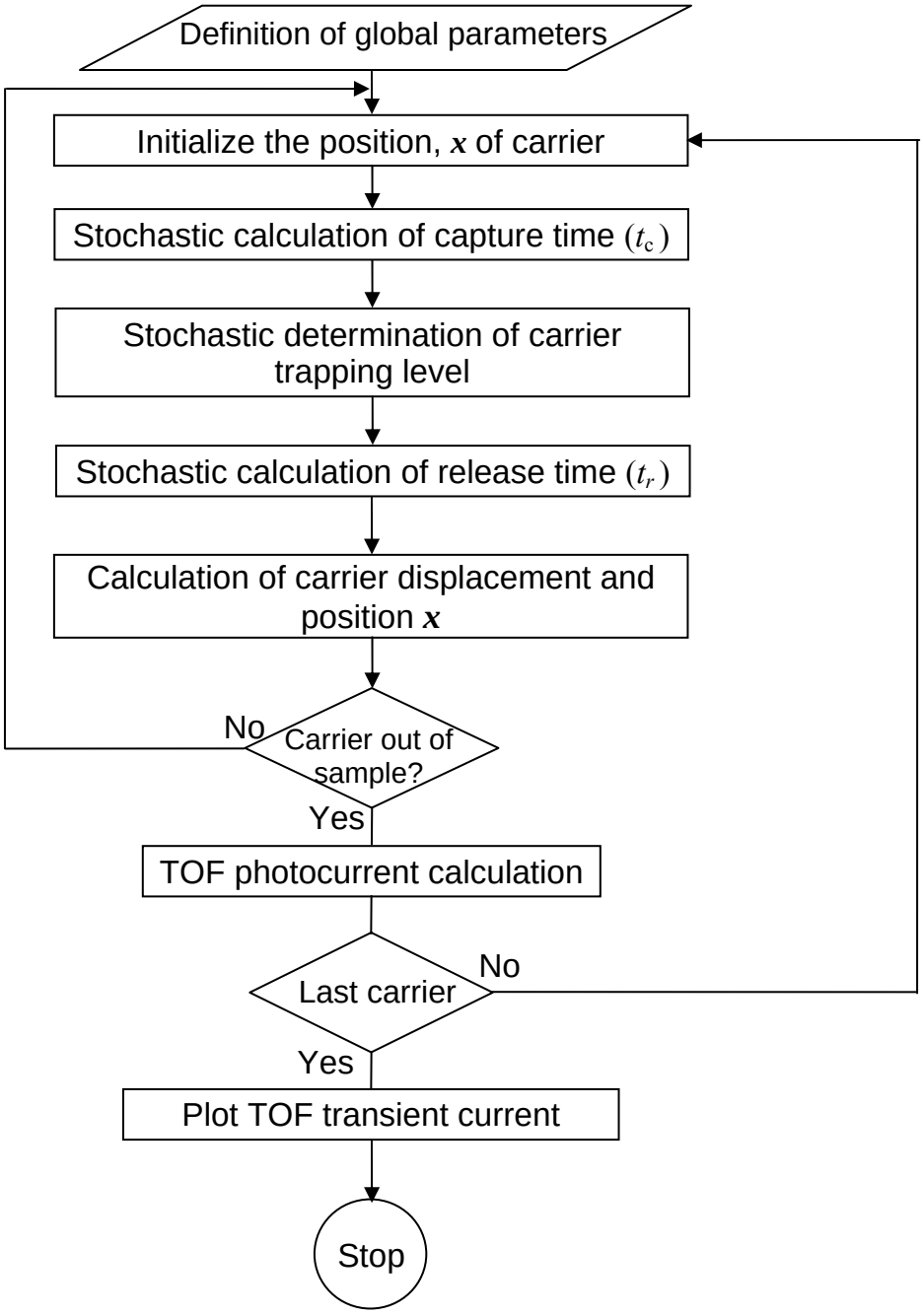

Figure 4.4: Flow chart of Monte Carlo simulation used to estimate TOF transient photocurrent in semiconductor model with traps at three discrete energy levels.

- ***Definition of global parameters***

  The global parameters are defined in the same manner as in the case of monoenergetic trap distribution. For this model there are three levels of traps and their capture and release times are defined at this stage. The TOF transient photocurrent is calculated by simulating the electron transport. The free drifting electrons contribute to the induced photocurrent in the external circuit. The parameters for calculating current are adjustable and are defined at this stage. Further explanation of the current calculation procedure is described below.

- ***Initializing the position, x of carrier***

  The position of the photogenerated carriers is initialized at this stage.

- ***Stochastic calculation of capture time (t_c)***

  The electric field throughout the sample is assumed to be uniform. The electrons drift towards the opposite electrode under the influence of the applied electric field. The carriers are then randomly captured in any of the three levels. The probability that a carrier will get capture in any of the three levels $(\tau_c^{tot})^{-1}$ is given by

$$\frac{1}{\tau_c^{tot}} = \frac{1}{\tau_{c1}} + \frac{1}{\tau_{c2}} + \frac{1}{\tau_{c3}} \tag{4.12}$$

  where τ_{ci} are the capture times for the three trapping levels. The stochastic capture time for a carrier is calculated using the overall probability of trapping using the expression

$$t_c = -\tau_c^{tot} \ln(r) \tag{4.13}$$

  where r is a computer generated random number with uniform distribution within the range [0, 1].

- ***Stochastic determination of the carrier capture level***

After the free flight the carrier is randomly trapped in one of the three trapping levels in accordance with the trapping probabilities for these levels. The trapping level is determined by defining an array of probabilities of trapping. The array consists of three elements represented here by p_1, p_2 and p_3, where

$$p_1 = \frac{\tau_c^{tot}}{\tau_{c1}},$$

$$p_2 = \frac{\tau_c^{tot}}{\tau_{c1}} + \frac{\tau_c^{tot}}{\tau_{c2}} \text{ and}$$

$$p_3 = \frac{\tau_c^{tot}}{\tau_{c1}} + \frac{\tau_c^{tot}}{\tau_{c2}} + \frac{\tau_c^{tot}}{\tau_{c3}} = 1$$

In order to determine the trapping level, a uniform random number r is generated and compared with the array, if $0 < r < p_1$, then the carrier is assumed to be trapped in level 1 (mobility level), similarly if $p_1 < r < p_2$, then the trapping level is 2 and if $p_2 > r > 1$, the carrier is assumed to be trapped in the deep trapping level. A simplified schematic of this block is shown in Figure 4.5. The concept of this method is similar to a roulette wheel, where the thickness of the three sectors of the roulette wheel represents the probability of capture of the carrier in that level.

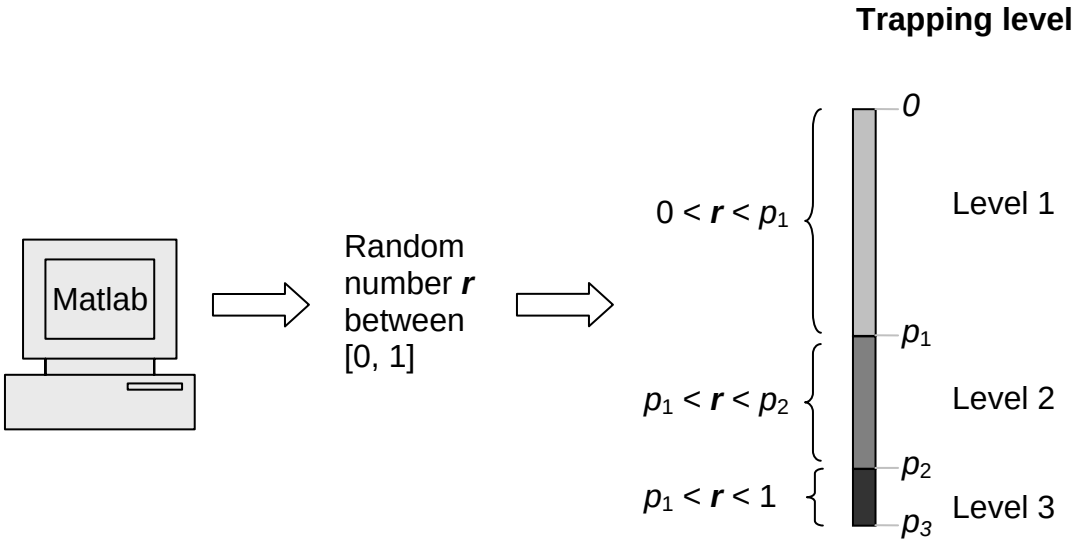

Figure 4.5: Stochastic determination of trapping level. Computer generated random number *r* is compared with an array of trapping probabilities to find the trapping level.

- ***Stochastic calculation of carrier release time (t_c)***

  The time for which a carrier dwells in the trap is also stochastic in nature and depends on the characteristic release time of that trapping level. The trapping level was determined in the previous block. In this block it is used here to calculate the release time for the carriers for that level by using the expression

  $$t_r = -\tau_{ri} \ln(r)$$

  where τ_{ri} is the release time of the *i*th level.

- ***Calculation of carrier displacement and position x of the carrier***

  The distance the carrier has been displaced after the free flight can be calculated by from the expression

  $$Move = \mu_0 \cdot F \cdot t_c$$

  where μ_0 is the drift mobility of the carrier at the mobility edge and F is the applied electric field. The total distance the carrier has traveled in the sample is the sum of all the displacements from the previous iterations. The total time elapsed in one iteration is the time the carrier was drifting free and the time it was immobile within a trap, hence both are added and recorded in memory.

- ***Check the position of carriers within the sample***

  This block checks if the carriers position *x* is still within the sample thickness.

- ***Is this the last carrier***

  After the carrier is out of the sample, all the required information is recorded in form of arrays and this process is repeated for the N_e carriers.

- ***Calculation of the contribution to the TOF transient current***

  The free drifting carriers contribute to the transient photocurrent. To calculate the TOF transient current, the time scale is divided into time bins of breadth Δt. The TOF transient current due to a single carrier at a given time t is proportional to the sum of the carrier displacements falling into the interval ($t-\Delta t/2$, $t+\Delta t/2$). The parameter Δt is adjustable. It should be large enough to include many events and to suppress statistical noise at the same time, it should be sufficiently short, to avoid smoothing of the TOF pulse shape. It was selected depending on the experimental conditions, after several trials which ensure that it is small enough and that the results of the simulations do not depend on it.

The photocurrents thus obtained from the Monte Carlo simulation were compared with inverse Laplace transform technique for a three trap level model in order to check the validity of these methods. A semiconductor sample of thickness L = 142 μm with traps at three different energy levels is considered. The capture times for the three levels are taken to be τ_{c1} = 43.14 ns, τ_{c2} = 9.135 μs, and τ_{c3} = 43.1 μs. The release times are τ_{r1} = 842.5 ns, τ_{r2} = 56.12 μs, and $\tau_{r3} \approx \infty$. Free carrier transit time ($t_T = L^2/\mu_0 V$) is 5.04 μs and the applied electric field F is 2.82 V/μm. The results of the MC simulation and inverse Laplace transform calculations are shown in the Figure 4.6. Figure 4.6(a) is the transient photocurrent on a linear scale and Figure 4.6(b) is the same transient curve but on a log-log scale to highlight the pre- and post- transit regions. The inverse Laplace transform calculations are shown as solid lines agree brilliantly with the circles representing the MC simulation.

(a)

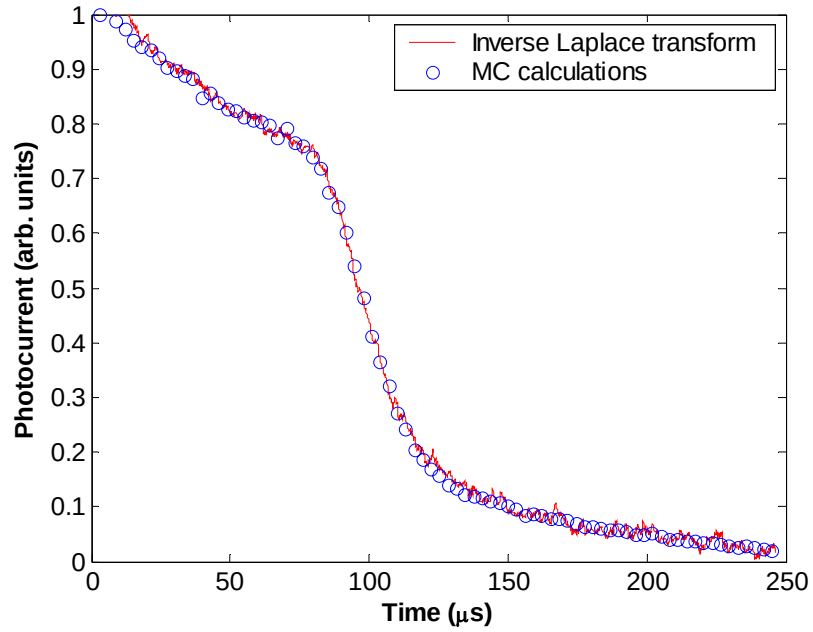

(b)

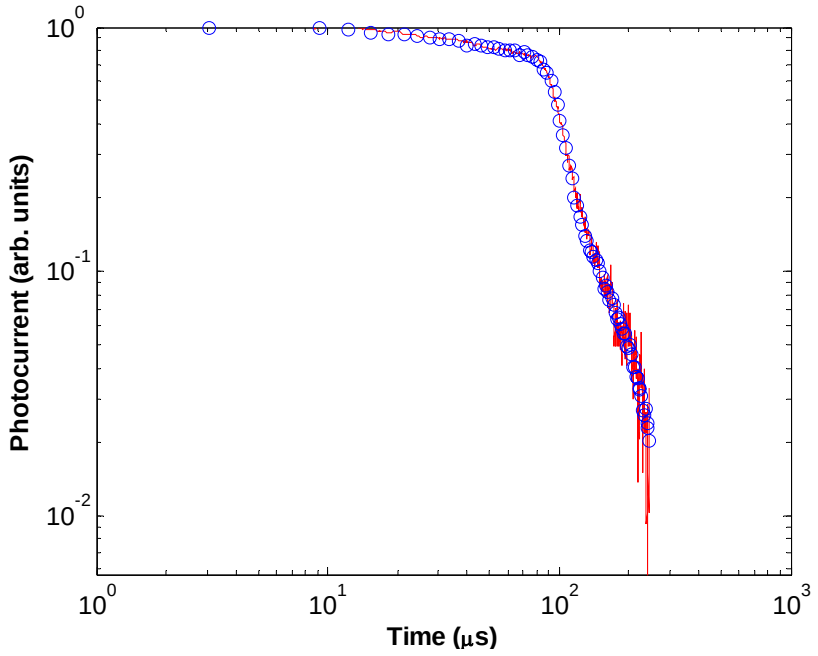

Figure 4.6: TOF transient current waveforms for a semiconductor model with three levels of trap obtained using a Monte Carlo simulation and compared with the inverse Laplace technique. Plot in Figure 4.5(a) is the current waveform on a linear-linear scale and Figure 4.5(b) is the same data plotted on a log-log scale.

4.5 Summary

In this chapter the MC models for charge transport in semiconductor with trap distribution at one and three discrete energy levels is discussed. The MC models presented in this chapter are based on simulating the motion of photogenerated carrier sheet inside a sample, subject to the force from applied electric field experiencing multiple trapping and release events in a TOF photoconductivity experiment. The duration of free flights and dwell times in trapping centers are stochastically calculated with the given probabilities of these events.

The monoenergetic trap distribution model is used to calculate free carrier spatial profile at various time intervals. The results were compared with the theoretical solution developed by pervious researchers and both agree brilliantly. The MC simulation model for a semiconductor with three trapping levels is used to calculate the transient photocurrents. The stochastic nature of trapping into the three levels and release events are simulated using random numbers with a uniform distribution. The results are compared with inverse Laplace transformation results and also are in excellent agreement.

5 Density of States of a-Se near the Conduction Band

5.1 Introduction

The Monte Carlo simulation models for charge transport in TOF photoconductivity experiments for semiconductors with a single level and three discrete levels of traps have been discussed and verified in the previous chapter. The calculation of charge transport in amorphous materials with a spectrum of DOS in the mobility gap is well known to be a complicated task. In this chapter the distribution of localized states (DOS) in amorphous selenium is investigated by comparing the experimentally measured transient photocurrents with those calculated by using the inverse Laplace transformation technique and the MC simulation method. The experiments and inverse Laplace transform calculation were performed by Koughia et al. and the results are published in their paper [45]. The samples were prepared by conventional vacuum deposition techniques. The experimental details are discussed in detail in the reference [45] and are not elaborated here.

5.2 DOS Distribution Calculations

The DOS distribution investigated here was obtained by the comparison of measured and calculated TOF shapes over a large range of electric fields (**F**). The final accepted DOS distribution was the one that generates the best calculated photocurrents,

closely matching the experimental photocurrent waveforms. The inverse Laplace transformation technique was used for the optimization process.

The DOS calculations started with a simple monotonous distribution with adjustable nodes that were adjusted to get a reasonable agreement between experimental and calculated photocurrents. The adjustable nodes and *spline* function (used for interpolation) were then replaced by predefined functions when it was apparent that the derived DOS distribution can be approximated as the sum of exponential and Gaussian distributions. The vertical positions of all the nodes and the total concentration of deep states N_{deep} were used as adjustable parameters, to minimize the discrepancy between the measured and calculated TOF photocurrent shapes. The DOS optimization was achieved by minimizing the mean-square deviation (MSD) between the experimental and calculated TOF photocurrent waveforms. The distribution of states lying deeper than E_c − 0.60 eV could not be resolved due to the lack of substantial thermal release from such deep states over the observation time of the experiment. The final optimized DOS distribution near the CB edge is shown in Figure 5.1.

This distribution achieved after the optimization process is a modified version of Abkowitz's [46] DOS model. There is an additional shoulder-like Gaussian *bump* at 0.45-0.50 eV below E_c. Mathematically, the DOS model is approximated as the sum of the exponential tail of the conduction band and two Gaussian distributions and can be written as

$$N(E) = N_c \exp\left(-\frac{E - E_c}{\Delta E}\right) + N_1 \exp\left(\frac{(E_1 - E_c)^2}{\Delta E_1^2}\right) + N_2 \exp\left(\frac{(E_2 - E_c)^2}{\Delta E_2^2}\right) \tag{5.1}$$

where N_c=2×10^{21} cm^{-3} is density of states at the CB edge, N_1 = 2.4×10^{16} cm^{-3}, N_2 = 5.6×10^{13} cm^{-3}, ΔE = 20 meV, ΔE_1 = 30 meV, ΔE_2 = 20 meV, $E_1 - E_C$ = 0.33 eV, and $E_2 - E_C$ = 0.448 eV for a given sample. The first term in the expression represents the extended tail distribution of localized states and the last two terms represent the larger Gaussian peak and the shoulder peak respectively.

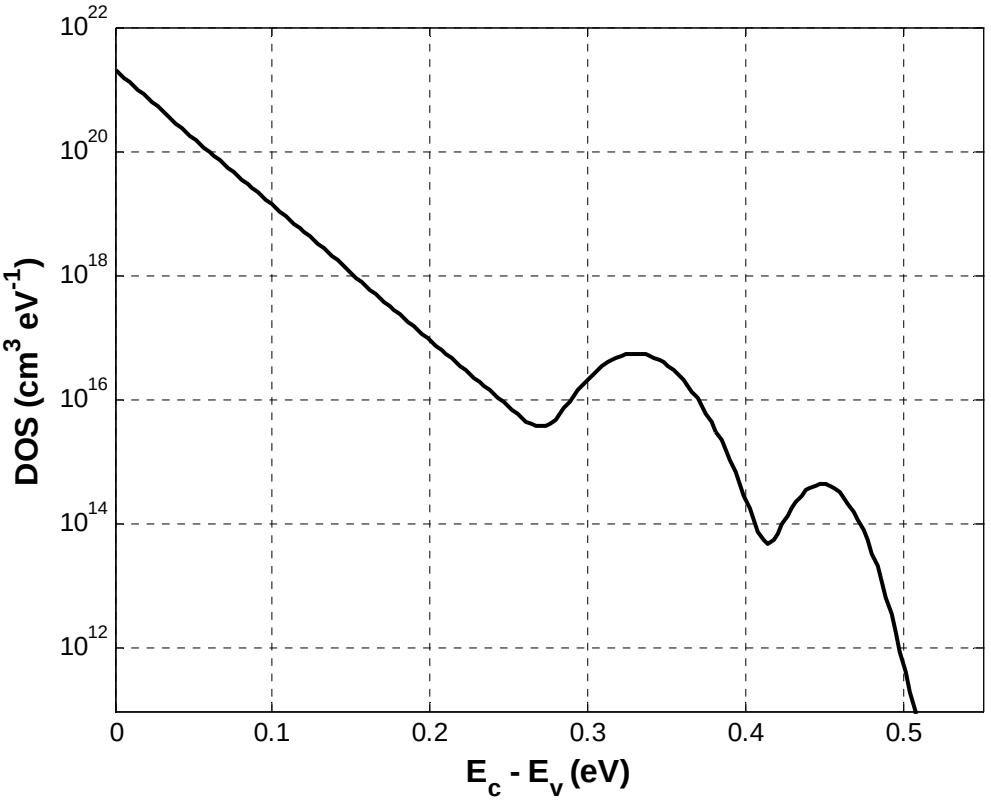

Figure 5.1: Density of localized states model in the mobility gap of a-Se near CB used in the Monte Carlo calculations of TOF transient photocurrent.

5.3 Inverse Laplace Transform Technique

The DOS distribution was optimized by the inverse Laplace transformation technique which is reviewed in this section. For inverse Laplace transformation and Monte Carlo simulation calculations, some reasonable approximations and assumptions were made. It was assumed that the small signal conditions are valid throughout the experiment. This condition implies that the injected charge concentration is so small that the distortion caused by this charge and the Coulombic interaction within the drifting packet on the applied electric field is negligible. It is also assumed that no space charge is accumulated during the photo-injection and transit of carriers. In a typical TOF photoconductivity experiment, following the application of the bias, a small amount charge is injected into the layer at the electrodes using photoexcitation and the carriers get trapped in the bulk of the sample. Eventually the concentration of this bulk space charge is sufficient to alter the

profile of the internal field. The time at which this occurs is known as the transition time t_{sc}. Prior to this stage it may be assumed that the internal field is uniform [63]. For a-Se films, it has been shown that t_{sc} is on the order of 100 ms [18].

The continuous distribution of localized states has been substituted by a set of discrete levels. This discretization technique of a continuous distribution of localized DOS is quite common and has been effectively used previously [64,65]. The energy scale is divided into slices of thickness dE, such that each slice has trap density N_{ti}. In our calculations, the number of discretization levels was chosen to be sufficiently high (normally > 100) so that the final solution was independent of the discretization.

Using the approximations and assumptions mentioned above, the carrier sheet transport mechanism can be described by a set of differential equations. These are the continuity, the charge conservation, and the trap occupation equations, and are written as follows

$$\frac{\partial \rho(\mathbf{x},t)}{\partial t} = g(\mathbf{x},t) - \nabla \cdot \mathbf{f}(\mathbf{x},t) \tag{5.2}$$

$$\rho(\mathbf{x},t) = n(\mathbf{x},t) + \sum_i n_i(\mathbf{x},t) \tag{5.3}$$

$$\frac{\partial n_i(\mathbf{x},t)}{\partial t} = n(\mathbf{x},t)c_i - n_i(\mathbf{x},t)r_i \tag{5.4}$$

where $\mathbf{x}$ is the spatial coordinate, t is the time, $\rho(\mathbf{x},t)$ is the total concentration of carriers, $g(\mathbf{x},t)$ is the photogeneration rate, $\mathbf{f}(\mathbf{x},t)$ is the flux of mobile charge carriers, $n(\mathbf{x},t)$ is the concentration of free carriers, $n_i(\mathbf{x},t)$ is the density of carriers trapped at the ith level, and c_i and r_i are the capture and release rates, respectively, to and from the ith level. The capture rates c_i (τ_{ci}^{-1}) were calculated from

$$c_i = C_t N_i,$$

where N_i is the concentration of the ith level and C_i is the capture coefficient. Capture coefficient C_i is equal to the product of thermal velocity v_{th} and capture cross-section σ. For

simplicity, the value of C_i was taken as 10^{-8} cm^3 s^{-1} for all the levels. The release rates were calculated as

$$r_i = \nu \cdot \exp\left(-\frac{(E_c - E_i)}{kT}\right)$$

where $\nu = 10^{12}$ s^{-1} is a typical phonon frequency and $E_c - E_i$ the depth of the ith level below E_c. Equations 5.2-5.4 can be solved using two practically realizable approximations.

1. δ-excitation, i.e., the excitation light pulse is assumed to be infinitesimally short and the light is absorbed in a very thin layer of material. This can be expressed in terms of a generation function g(**x**,t)= $\eta\delta$(**x**) δ(t), where η is the quantum efficiency.
2. The diffusion of carriers is negligible with respect to their drift, i.e., the carrier flux is **f**(x,t)= μ_0**F**n, where μ_0 is the mobility of carriers in the conduction band and **F** is the electric field.

The final solution found using the Laplace transform technique [66] is,

$$\tilde{I}(s) = \frac{e\eta}{t_0} \times \frac{1 - \exp[-a(s)t_0]}{a(s)} \tag{5.5}$$

where $\tilde{I}(s)$ is the photocurrent Laplace transform and

$$a(s)t_0 = s\left(t_0 + \sum_i \frac{c_i t_0}{s + r_i}\right) \tag{5.6}$$

Here, $t_0 = L/\ \mu_0\mathbf{F}$ is the free carrier transit time and L is the thickness of the sample. To obtain the photocurrent time dependence from Equations 5.5 and 5.6, the inverse Laplace transform was numerically calculated, using the method of Padé coefficients [67].

5.4 Initial Position of EHP Calculations

In a TOF photoconductivity experiment, an extremely short pulse of strongly absorbed radiation through a semitransparent electrode is used to generate a thin sheet of electron hole pairs (EHPs) near the surface of the sample. The wavelength of radiation is carefully selected so that the absorption depth (δ) is considerably smaller than the sample thickness L i.e. $\delta << L$. In the analytical models discussed in the previous chapters it was considered that electron hole pairs were generated near the surface of the electrode. In other words the sample is considered to have infinite absorption so that the photons are absorbed by the a-Se sample to generate the EHPs at $x = 0$.

When a medium is irradiated, some of the incident photons are absorbed by the medium. Consider a sample of thickness dx that is irradiated. The number of photons interacting with the medium in the slice is proportional to the sample thickness dx and the number of incident photons N. If the change in the number of photons during traveling a thickness dx is represented by dN, then

$$dN \propto N dx$$

or
$$dN = -\alpha N dx \tag{5.7}$$

where α is the constant of proportionality and is called *linear attenuation coefficient* of that medium. The negative sign in the equation indicates reduction in the number of photons. Rearranging the above equation we have

$$\frac{dN}{N} = -\alpha\, dx\,.$$

Integrating above expression we have

$$\int_{N_0}^{N} \frac{dN}{N} = -\int_{0}^{x} \alpha\, dx$$

$$N(x) = N_0\, e^{-\alpha x} \tag{5.8}$$

where N_0 is the number of incident photons and N represents the transmitted photons at a distance x from the irradiated surface. From Equation 5.8, it is clear that the radiation will be absorbed exponentially in the medium as a function of the attenuation coefficient of the medium [68].

The incident excitation pulse creates EHPs along the irradiated surface through a number of steps. The incident photons ionize the medium and result in the generation of an energetic primary electron and as this electron travels in the medium, it causes ionization along its track and hence results in the creation of many EHPs. The radiation absorbed exponentially (Equation 5.8) will create EHPs along its path. The spatial position of these EHP is completely random but the overall density distribution is exponential. This phenomenon is illustrated in Figure 5.2. Considering a uniform electric field throughout the sample, the carrier generation profile can be written as

$$C(x) = C_0 \, e^{-\alpha x} \tag{5.9}$$

where C_0 is constant.

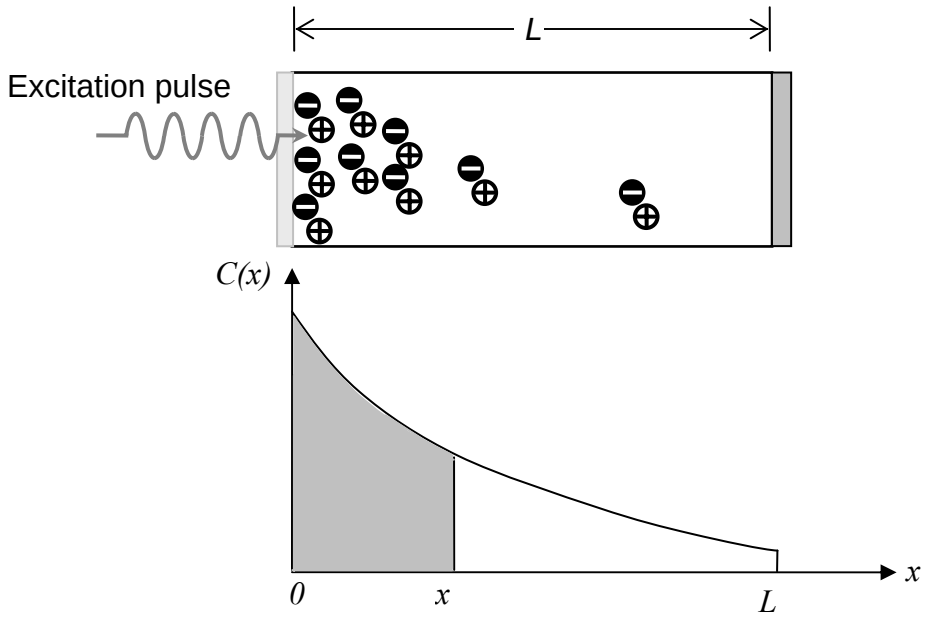

Figure 5.2: Process of EHP generation by a short excitation pulse is shown here.

In order to randomly compute the positions of the carriers so that the overall carrier distribution corresponds to the carriers generated by excitation pulse (that is exponentially distributed), a *probability density function* (PDF) is defined. The PDF for the generated carriers at position x inside the sample is defined as the ratio of the total generated carriers within the thickness from 0 to x to the total number of carriers in the sample. The PDF is then equated to random numbers, i.e.

$$\mathrm{PDF} = \frac{\int_0^x C_0 e^{-\alpha x} dx}{\int_0^L C_0 e^{-\alpha x} dx}$$

$$r = \frac{(1 - e^{-\alpha x})}{(1 - e^{-\alpha L})} \tag{5.10}$$

where r is a random number with uniform distribution in the interval [0, 1]. Rearranging the equation for x, we have

$$x = -\frac{1}{\alpha} \cdot \ln\left[1 - r \cdot (1 - e^{-\alpha L})\right]. \tag{5.11}$$

Equation 5.11 is used to calculate the initial position of the photogenerated carriers in the TOF experiment modeling [69].

5.5 Monte Carlo Simulation Model

The DOS distribution achieved by the inverse Laplace transformation technique was further investigated by performing the MC simulations of electron TOF photocurrents. The MC simulation model used for this purpose is based on the MC models for the simpler cases described in the previous chapters. The MC model simulates the transport of electrons in a sample of a-Se in the TOF experiment employing the proposed DOS distribution. The program simulates the behavior of N_e electrons. For the simulation performed for this work, values of $N_e > 10^4$ provide good reproducible results with small

statistical noise. It is assumed for the MC simulation models that the small signal condition is valid. The algorithm of the MC simulation model is shown in Figure 5.3, and the blocks of the algorithm are explained below.

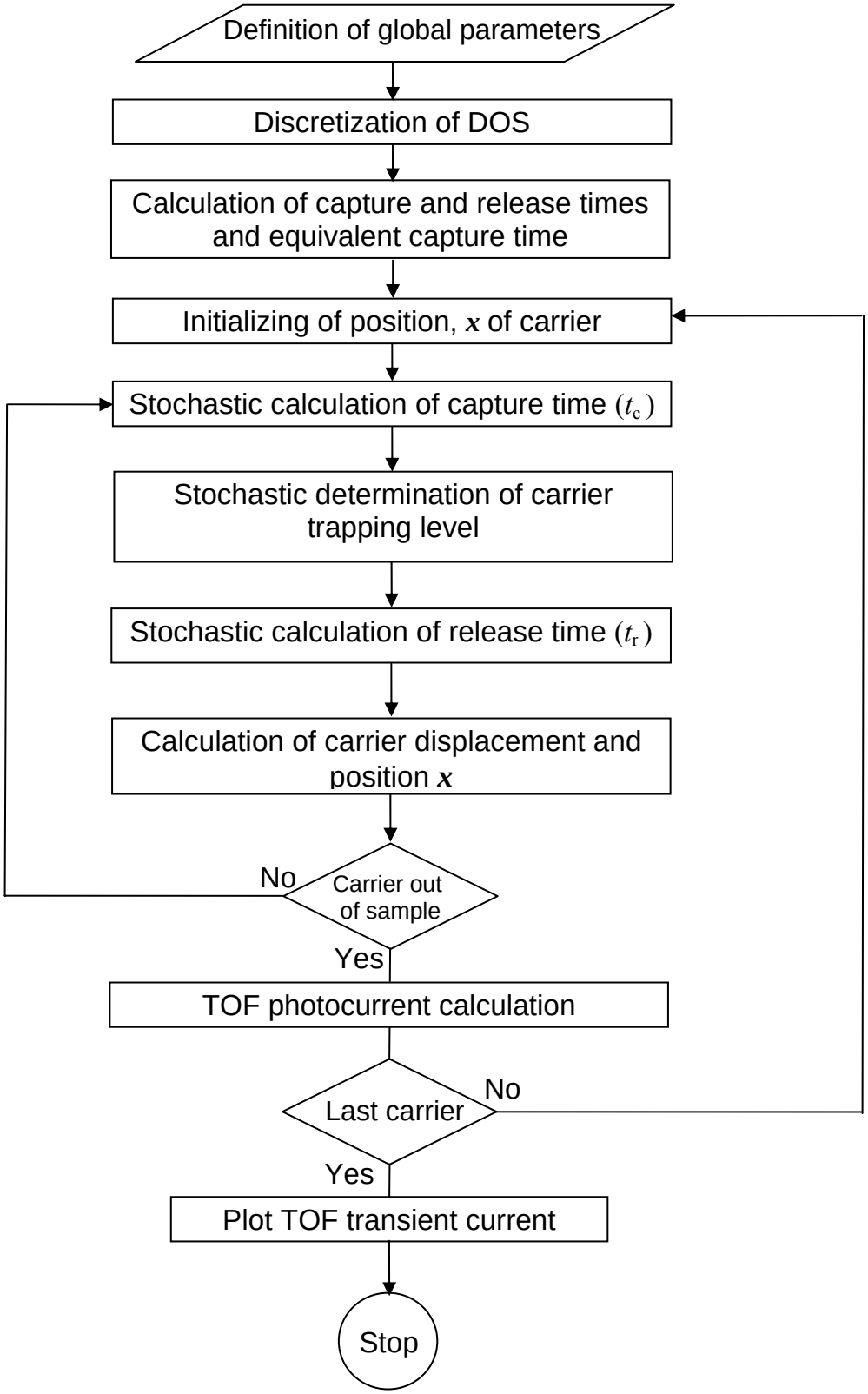

Figure 5.3: Flow chart of MC simulation model for semiconductor with continuous distribution of traps.

- ***Definition of global parameters***

  The first step of the simulation process is the definition of global parameters governing the simulation in the same manner as for the monoenergetic and three trap level simulations.

- ***Discretization of the density of states***

  In this block, the DOS distribution is defined mathematically as sum of exponential and Gaussian distributions as a function of energy. The energy scale is divided into *n* slices of thickness ΔE and the continuous localized state distribution is replaced by a set of discrete levels with concentrations N_i, where $i = 0 \ldots n$, and $i = 0$ corresponds to the mobility edge of the conduction band. The simulation results are found to be independent of the choice of *n*, as long as it was greater than 50. Therefore, for all the photocurrent calculations $n = 100$ is used, which gives excellent reproducibility.

- ***Calculation of the capture and release times and the equivalent capture lifetime***

  The capture time constants (τ_c^i) are calculated for all *n* levels (slices) from the expression

$$\tau_c^i = \frac{1}{N_i C_t}$$

  where C_t is the capture coefficient which, for simplicity, was kept equal to 10^{-8} cm^3 s^{-1} for all levels. The release (τ_r^i) time constant for the *i*-th level is calculated using the expression

$$\tau_r^i = \nu_{ph}^{-1} \exp\left(\frac{E_c - i\Delta E}{kT}\right)$$

  where $\nu = 10^{12}$ s^{-1} is a phonon frequency and ($E_c - i\Delta E$) is the depth of the *i*th level. After calculating τ_c^i, these values are used to calculate the equivalent capture lifetime

(τ_c^{total}). This time constant represents the capture time for the carrier into *any* of the levels and is calculated using

$$\tau_c^{tot} = \left(\sum_{i=1}^{i=n} \left(\frac{1}{\tau_c^i} \right) \right)^{-1}.$$

It is observed that the characteristics of very shallow states (i.e., those with $\tau_r^i << \tau_c^i$) do not affect the shape of the transient current. The release time from very shallow states is so short compared to the capture time that, within this time resolution, the carrier is captured and then released almost instantly such that it spends more time in the free extended states above the mobility edge than below it in the shallow tail states. Consequently, the behavior of these electrons is indistinguishable from that of free carriers and hence does not contribute to the current shape. Therefore, after investigation, the influence of these states has been neglected in the calculations, resulting in a hefty reduction in the computation time.

- ***Carrier position initialization***

At this stage, the position of the carriers is initialized. The procedure for calculating the initial position of photogenerated carriers is discussed in section 5.4. The expression that can be used for the calculating the initial position is

$$x = -\frac{1}{\alpha} \cdot \ln\left[1 - r \cdot (1 - e^{-\alpha L})\right]$$

where r is a random number uniformly distributed between [0,1], and α is the absorption coefficient of the sample. In our calculations, the value used for absorption coefficient is $\alpha = 10^7$ m^{-1}. Including finite absorption by using the above expression had no visible effect on the calculated photocurrents.

- ***Stochastic determination of the free travel time***

In this block, the random time which the carrier spends free before getting captured (t_c) is calculated. It is computed as

$$t_c = -\tau_c^{tot} \ln(r),$$

where r is a computer generated random number with a uniform distribution within the range [0,1]. The value of t_c is used later for the calculations of the current carrier position. This stage is the beginning of an iterative process of carrier drift simulation, which is repeated every time the carrier is trapped and subsequently re-released to the conduction band.

- ***Stochastic determination of the carrier capture level***

  After the free flight, the carrier gets captured randomly in any of the n levels. In order to find the level of trap with an appropriate random component, an array consisting of the inverse mean capture times $(\tau_c^i)^{-1}$ for all i =1 . . . n levels is generated. This array acts as a "roulette wheel", whose "sectors" are proportional to the probabilities of electron capture. A uniformly distributed random number is generated and compared with this array. The sector within which the random number falls defines the capture level.

- ***Stochastic determination of the carrier release time***

  The time which the electron spends trapped in the localized level before release (t_r) is calculated as

  $$t_r = -\tau_r^i \ln(r),$$

  where τ_r^i is the mean release time for the level i, as calculated earlier.

- ***Calculation of the carrier displacement and current position***

  At this stage, we calculate the current carrier displacement as

  $$\text{Move} = \mu_0 \cdot F \cdot t_c,$$

where μ_0 is the mobility at the edge of the conduction band and F is the electric field. The latest position of carrier is calculated as the sum of the present and all previous displacements.

- ***Calculation of the contribution to the TOF transient current***

  For the calculation of the TOF transient current, we divide the time scale into time bins of breadth Δt. The TOF transient current due to a single carrier at a given time t is proportional to the sum of the carrier displacements falling into the interval ($t-\Delta t/2$, $t+\Delta t/2$). The parameter Δt is adjustable. It should be large enough to include many events and to suppress statistical noise. On the other hand, it should be quite short, to avoid smoothing of the TOF pulse shape. Therefore, it has been selected depending on the experimental conditions, after several trials which allow us to ensure that it is small enough and that the results of the simulations do not depend on it.

- ***Is the carrier still inside the sample?***

  This block checks if the carrier is still inside the sample, by comparing its current position with the sample thickness. If the current position exceeds the sample thickness, then the calculation proceeds by examining the next carrier.

- ***Is it the last carrier?***

  The last block checks if we are dealing with the last carrier of the specified number. If so, it terminates the program.

The TOF photocurrent waveforms obtained using MC simulations for different values of electric field are compared with experimental results. Samples of a-Se and stabilized a-Se for experimental data were prepared by thermal evaporation of Se pellets on either aluminum plates or Corning 7059 glass substrates. The top electrodes on the sample were of semitransparent of sputtered platinum or gold. Sample thickness ranged from 50 to 200 μm. The details of sample preparation and experimental procedure are explained in the reference [45]. Comparison of the results is shown in the Figure 5.4. The waveforms in the left column are on a linear scale and the same data is plotted on a log-log scale. The pre-

and post- transit regions are clearly distinguishable on the log-log scale and it is evident that the calculated waveform and the experimental results are in excellent agreement.

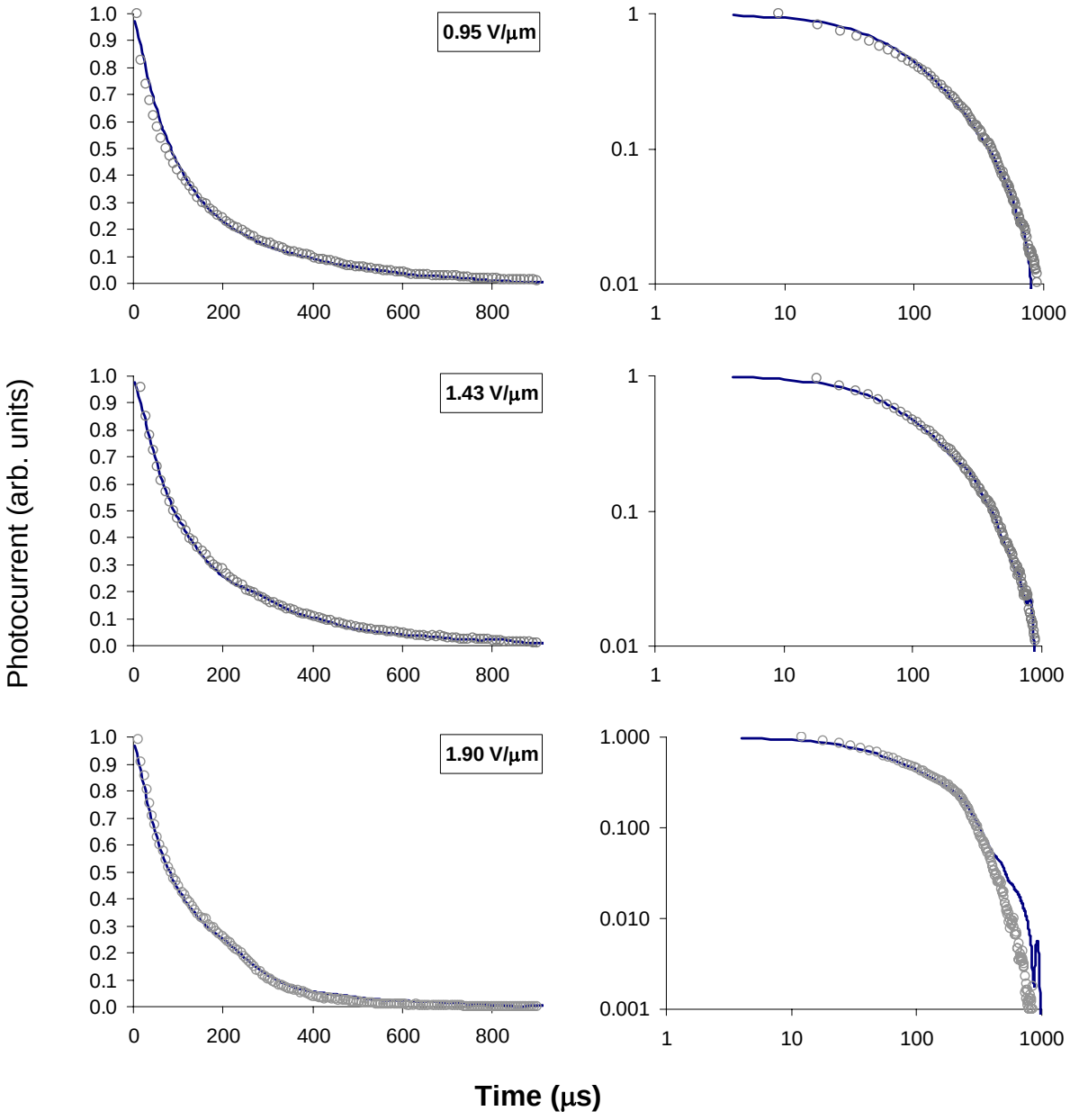

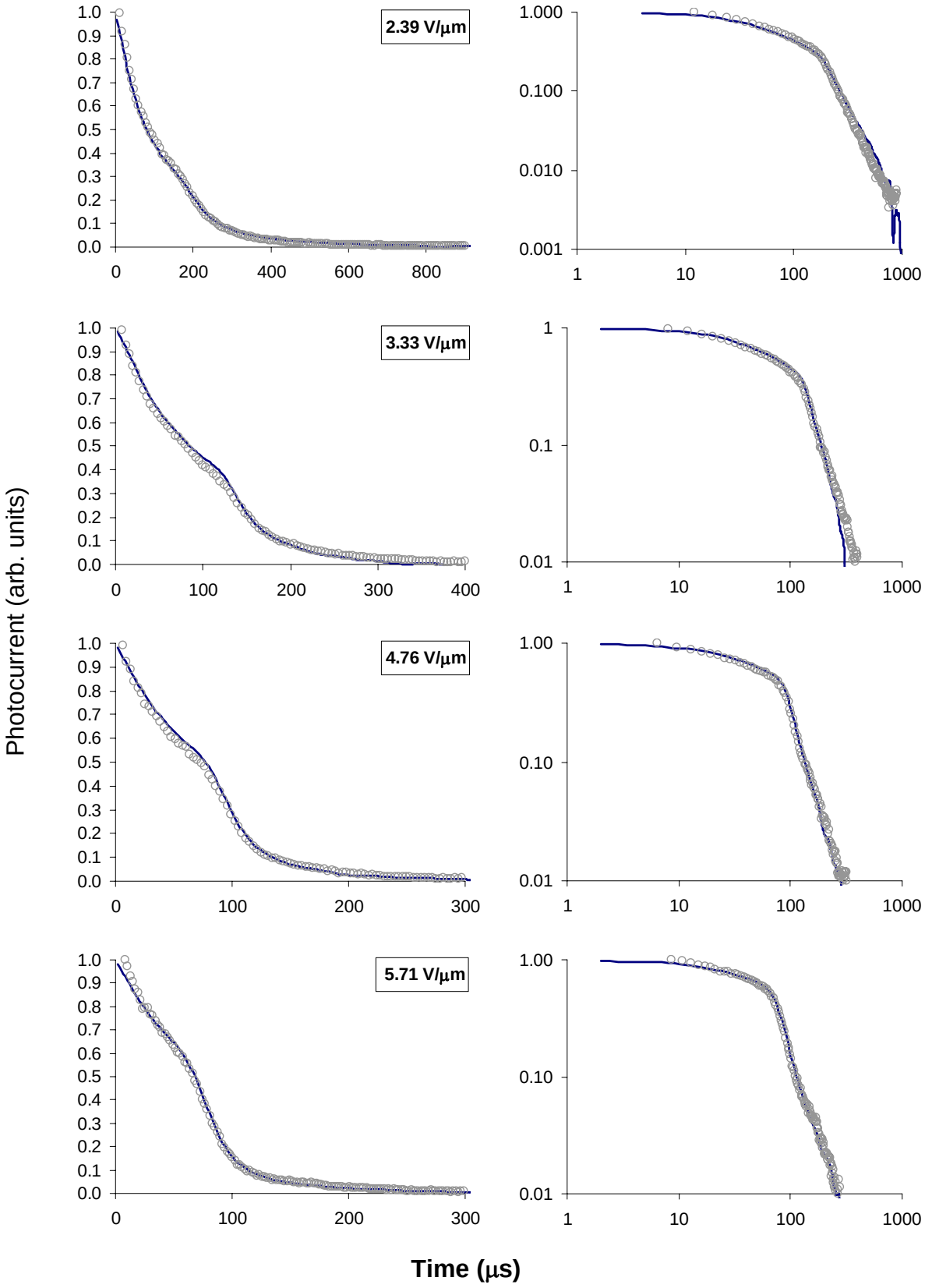
2.39 V/μm
3.33 V/μm
4.76 V/μm
5.71 V/μm
Photocurrent (arb. units)
Time (μs)

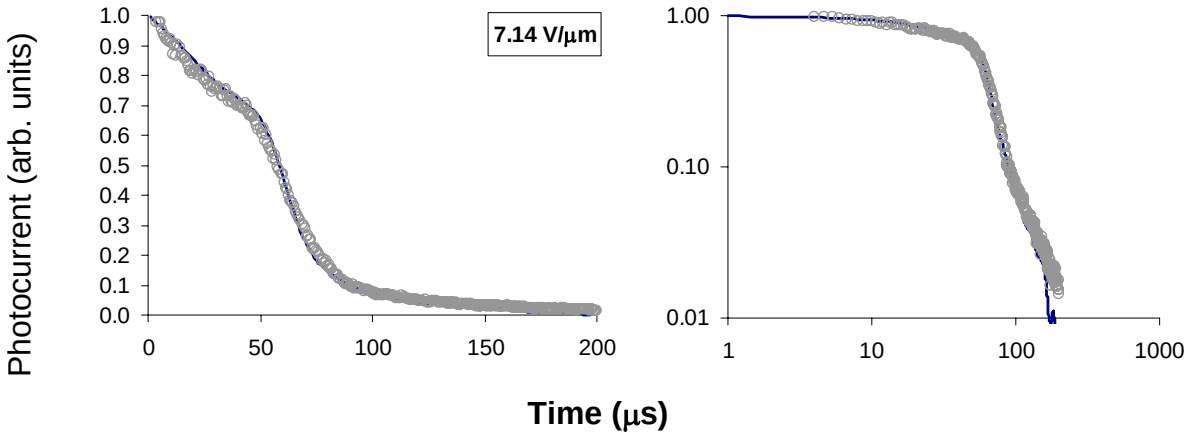

Figure 5.4: Comparison of the TOF transient photocurrent calculated using MC (circles) techniques and experimentally measured data (solid line). The left column presents the TOF data on a linear–linear scale and the right column presents the same data on a log–log scale.

5.6 Results Discussion

In the previous section the calculated and experimentally measured photocurrents were shown to compare satisfactorily by using the proposed DOS for a wide range of electric fields. It is worth mentioning that the optimized DOS investigated in this work may not necessarily be unique, rather, it is an *effective* DOS that is able to explain the observed TOF photocurrent shapes, while not excluding other possibilities. However there are some important points that support the DOS model proposed in this work. First is that the proposed DOS distribution is very stable with respect to sample to sample variations. This means that only small variations in the DOS distribution, such as a shift and/or correction in the amplitudes of the Gaussians, are needed to explain TOF experiments on different samples. Second, for any sample, the proposed DOS distribution is able to explain the experimental data for a large range of applied electric fields, as shown in Figure 5.4. It should be noted that the coincidence of the calculated and measured curves is unlikely to be accidental over a time interval covering more than two orders of magnitude. The fact that the DOS remains consistent for electric field variations exceeding one order of magnitude is a convincing factor. The effect of aging, annealing and alloying with As and doping with Cl on the DOS distribution have been also investigated by Koughia [45]. The salient

features of the proposed DOS distribution and their origin as discussed by Kougiha et al. are as follows:

A *random chain model* has been widely accepted as a structural model for *a*-Se. All of the atoms in this model are in two-fold coordinated chain structures and the dihedral angle is constant in magnitude but changes in sign randomly. The random chain model for a-Se has been discussed in detail in chapter 2. The random chains in the amorphous structure have chainlike and ringlike regions which are essentially fragments of perfect chains in trigonal γ-Se and Se_8 rings in α-Se. Only holes are considered to be mobile in γ-Se [70], whereas only electrons drift in monoclinic α-Se [71]. Theoretical calculations have shown that the random alternation of dihedral angles may itself produce localized (defect) states within the mobility gap, which would obviously affect the electronic properties [72].

The dominant feature of the DOS distribution in the upper half of the mobility gap is the primary peak at ~0.30 eV below the CB band edge E_c, which was introduced by Koughia et al. to explain the temperature dependence of the drift mobility. From the persistence of this peak for all of their samples, and the relative stability of its value, they have concluded that it may be connected with intrinsic defects in *a*-Se, such as distortions of the normal dihedral angle. The electron drift mobility in α-monoclinic Se is also thermally activated at low temperatures, which is regarded as evidence for the existence of a defect level at ~0.25 eV below E_c. It has been also proposed that the defect level in α-Se and the DOS peak in *a*-Se may have a common origin. The small difference of ~0.05 eV in their positions with respect to E_c can be accounted for by the formation of localized tail states below E_c in the amorphous phase. This interpretation is further supported by the observation in their paper that the mobility-controlling peak at E_c–0.30 eV persists even with alloying with As and doping with Cl.

The exact shape of the DOS distribution for deep states can not be conclusively decided. For the MC simulation calculation these states were assumed to have a Gaussian distribution. From the MC simulation results it can only be concluded that these states lie mostly below ~0.6 eV from E_c. At 0.65 eV below E_c and beyond, the position of these deep states had no visible effect on the transient photocurrent shape. These may be the states at E_c–1.1 eV identified by Abkowitz and Enck using Xerographic measurements [51]. The

exact nature of these states is still unknown, but their sensitivity to technological parameters, such as doping, alloying, and deposition temperature, is confirmed by numerous experiments. Koughia et al. have observed that the concentration of these deep states is very sensitive to alloying and doping. It also varies with aging and annealing. The exact nature of these states is unknown but, obviously, they behave as thermodynamic defects.

It is also noticed that the small peak (or shoulder) at 0.43–0.50 eV below E_c seems to behave in a similar way to the deep traps to aging (relaxation) and annealing. Consequently, it is concluded that the states forming the secondary peak (or shoulder) at 0.45–0.50 eV below E_c are also thermodynamic defects. These states may be connected with the existence of VAPs that is Se_3^+ and Se Se_1^- defects. Song [73], using a post transit photocurrent analysis, found a peak in the DOS of *a*-Se at about 0.55 eV, which is relatively close to the shoulder we observe at 0.45–0.50 eV. A similar electron trap peak has been observed at about the same energy from a cycled up residual voltage decay analysis [74].

5.7 Summary

In this chapter the MC simulation model for investigating the DOS distribution in the mobility gap of a-Se has been discussed. The MC model is used for calculating transient photocurrents that are compared with the experimentally measured and calculated transient photocurrents. The transient photocurrents were first calculated by the inverse Laplace technique and were verified by the MC simulation technique presented in this chapter. The resulting DOS has distinct features: A first peak at ~0.30 eV below E_c with a relatively stable amplitude ~10^{17} eV^{-1} cm^{-3}, which may be associated with such intrinsic defects as distortions of the normal dihedral angle, and a second small peak (or shoulder) at 0.45–0.50 eV below E_c with an amplitude 10^{14}-10^{15} eV^{-1} cm^{-3}, which may be related to the existence of VAPs consisting of Se defects.

The DOS distribution contains deep states with an integral concentration of 10^{14}–10^{15} cm^{-3} lying below 0.65 eV, whose exact distribution could not be resolved. The second

shoulder-like peak and the deep states are believed to correspond to *thermodynamic defects*, i.e., defects whose concentration is relaxing in a reproducible way to some equilibrium value after thermal treatments and/or cycling.

6 Density of States of a-Se near the Valence Band

6.1 Introduction

In the previous chapter the distribution of density of localized states near the CB mobility edge has been discussed. In this chapter, the DOS distribution in the lower half of the mobility gap of amorphous selenium near the VB has been analyzed. This is achieved by comparing TOF transient photocurrents at various temperatures calculated by the MC simulation technique using the proposed DOS distribution with data published elsewhere [66]. The shape of the density of states distribution is further investigated by comparing the hole drift mobility-temperature characteristics for different DOS distributions.

6.2 Model for DOS Distribution Near E_v

As mentioned in the previous chapter, the DOS distribution in the mobility gap of amorphous selenium is a still a subject of controversy. It is generally agreed upon that the DOS distribution in the upper half of the mobility gap near the CB mobility edge is not monotonous but contains peaks at certain energy levels. The exact position of these peaks are still being actively discussed. The DOS distribution in the lower half of the mobility gap near the VB edge has proven to be even more controversial. The generally accepted model proposed by Abkowitz in 1988 [75] contains a sharp peak at around 0.28 eV above E_v. On the other hand, Natio and co-workers [76] have suggested a DOS distribution that decays into the mobility gap with a very small Gaussian *bump* around 0.24 eV above the VB edge. They deduced their DOS model after re-examining the hole drift mobility-temperature data reported by Kasap and Juhasz [77]. A research group [73,78] after performing post-transit current measurements have reported another peak at 0.4 eV above

the VB edge. Recently Koughia [50] has proposed another model that is a monotonically decaying featureless distribution without the prominent 0.28 eV peak present in Abkowitz's model.

In this research work the DOS model proposed by Koughia has been investigated by calculating TOF transient photocurrents at various temperatures to compare with data reported previously by Pfister and Noolandi. The monotonic feature of the proposed DOS distribution is further investigated by comparing hole drift mobility-temperature (μ_h vs. $1000/T$) characteristics from purely a exponential distribution and Gaussian distribution as a function of electric field and temperature. The DOS distribution used for calculating the transient photocurrents to compare with the published data is shown in Figure 6.1.

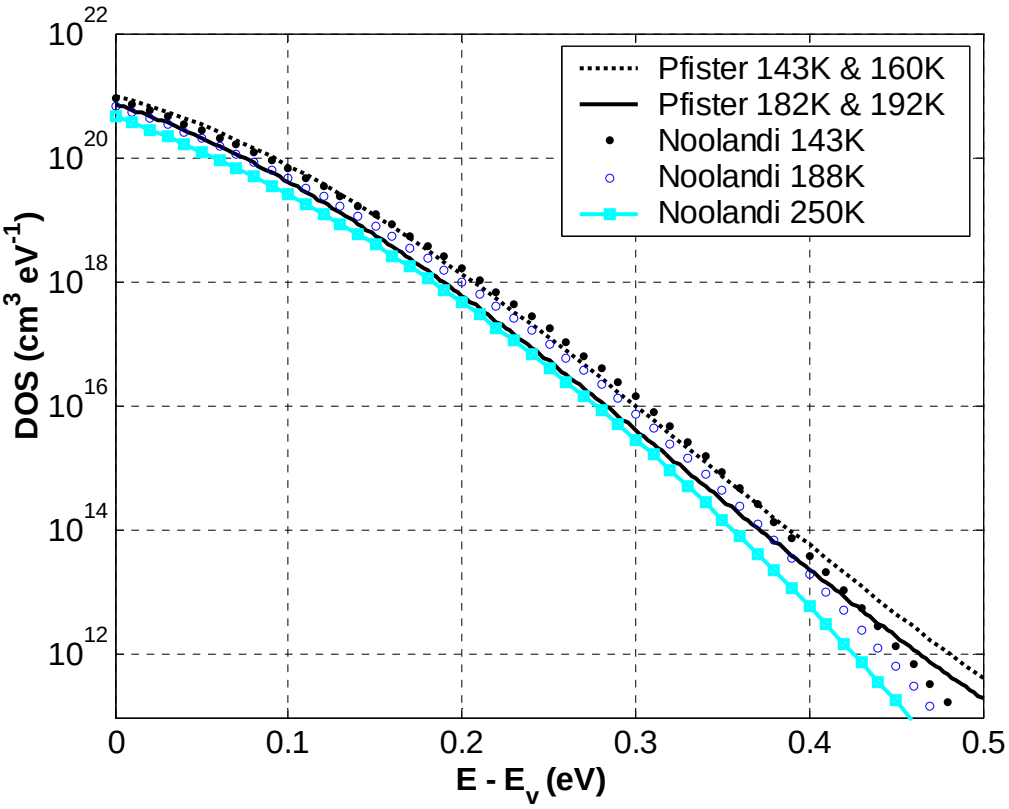

Figure 6.1: DOS distribution near the VB mobility edge in a-Se. The DOS distribution was used to compare the TOF transient currents with previous researchers is shown here. There is a slight shift in the position of the distribution with a change in temperature.

The inset of the Figure represents the source and the temperature of the TOF photocurrent data for which the respective DOS distributions were used to calculate the MC photocurrent.

6.3 MC Simulation Results

The MC simulation model for hole transient photocurrent calculations is similar to the one discussed in the previous chapter for electron transport with appropriate modifications in the carrier parameters. First, the MC simulation technique was used to calculate transient photocurrents using the DOS distribution shown in Figure 6.2 to compare with photocurrents measured by Noolandi.

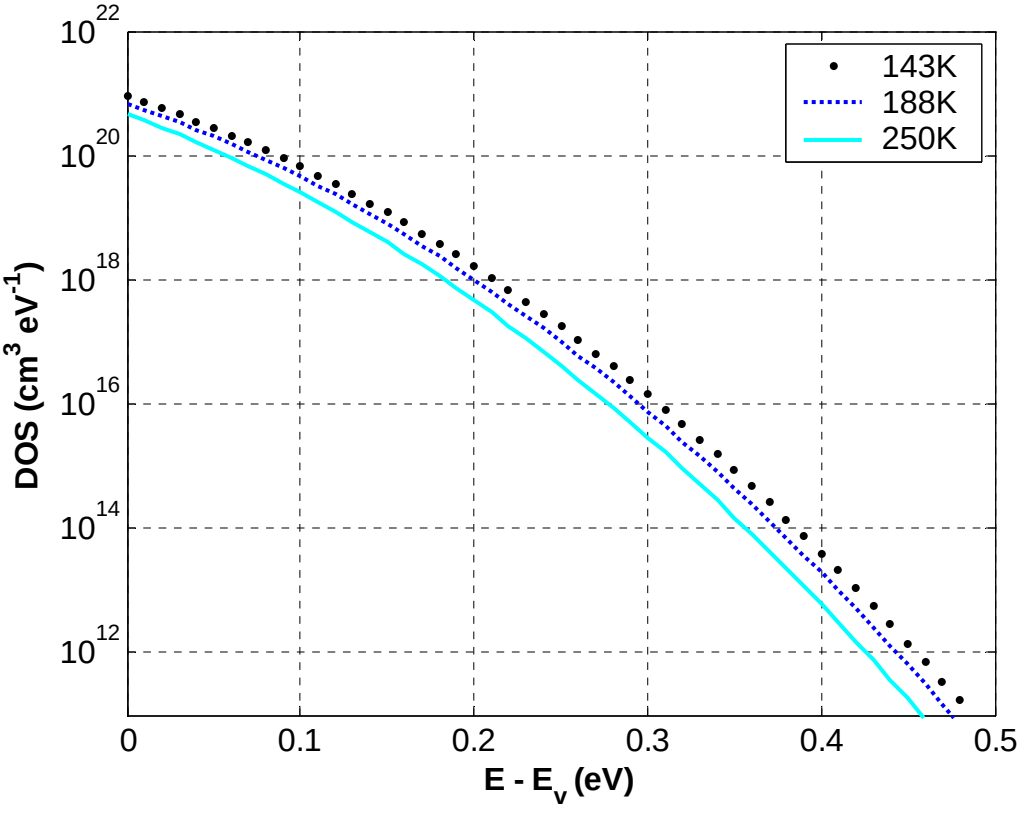

Figure 6.2: DOS distributions in the mobility gap of a-Se near VB edge at three different temperatures. As the temperature increases from low (143K) to high (250K), the DOS shifts slightly.

The photocurrents at low (T = 143K), medium (T = 188K), and high (T = 250K) temperatures with electric field strength of F = 10V/μm and sample thickness of 79μm are reported in that paper. The DOS distribution was adjusted until the photocurrents from the Monte Carlo simulation and experimental results were in reasonable agreement. The mobility edge was shifted by a small amount (Δ) with varying temperature to obtain a better fit of current waveforms. The shift in the mobility edge with temperature is approximately $\sim 3\times10^{-4}$ eV K^{-1}. The final DOS distribution seems to be monotonic and featureless, almost like an "exponential tail", at least in the range from E_v up to E_v + 0.4 eV where E_v is the mobility edge of valence band. The calculated and experimentally measured photocurrents are compared in Figure 6.4. Both results are in excellent agreement for the different values of temperature.

The MC transient photocurrents were then calculated to compare with the measured photocurrents reported by Pfister. The amorphous selenium samples used in Pfister's TOF were prepared by open-boat evaporation onto an Al or Au substrate at 55 °C. It was observed that some shallow states 0–0.15 eV and some relatively deeper states 0.35–0.43 eV can be neglected during the MC calculation without any noticeable effect on the transient current shape. Neglecting the states significantly reduces the computational time. The calculations were verified by using the inverse Laplace transformation technique and similar results were observed. The DOS distribution used in the MC calculations of photocurrents to compare with Pfister's data is shown in Figure 6.3. The calculated photocurrents and experimentally measured photocurrents are shown in Figure 6.5. Both the results are in excellent agreement over the range of temperature.

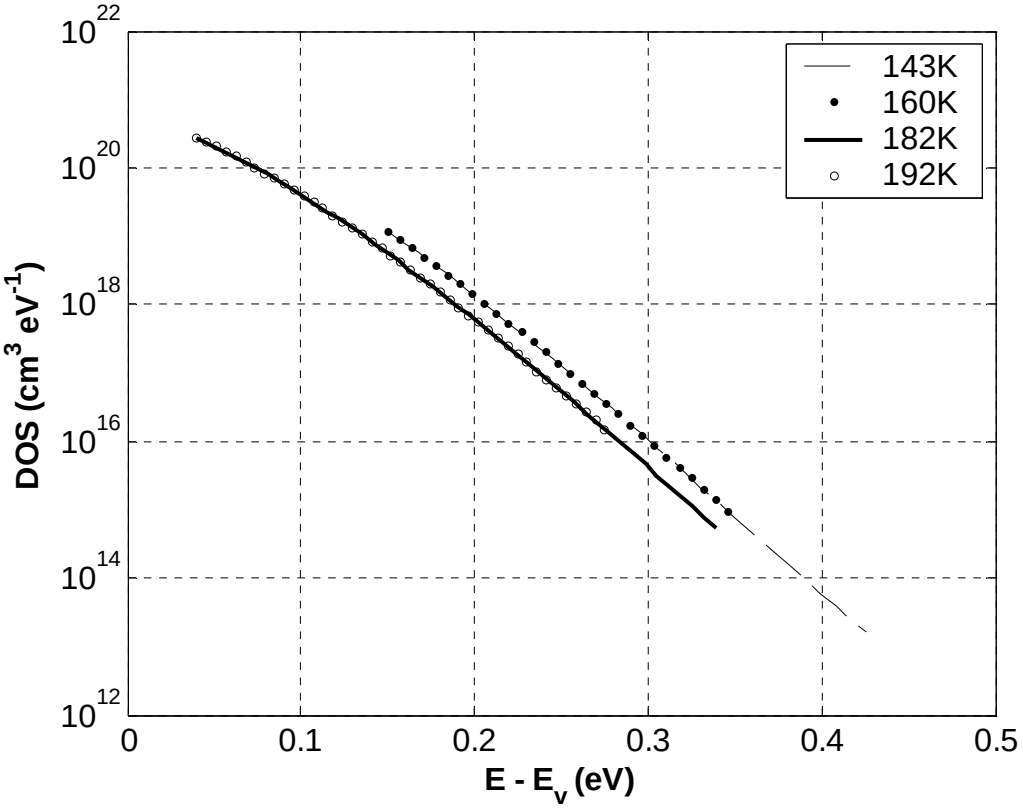

Figure 6.3: DOS distribution near VB edge used to calculate TOF transient photocurrents to compare with previously published results by Pfister.

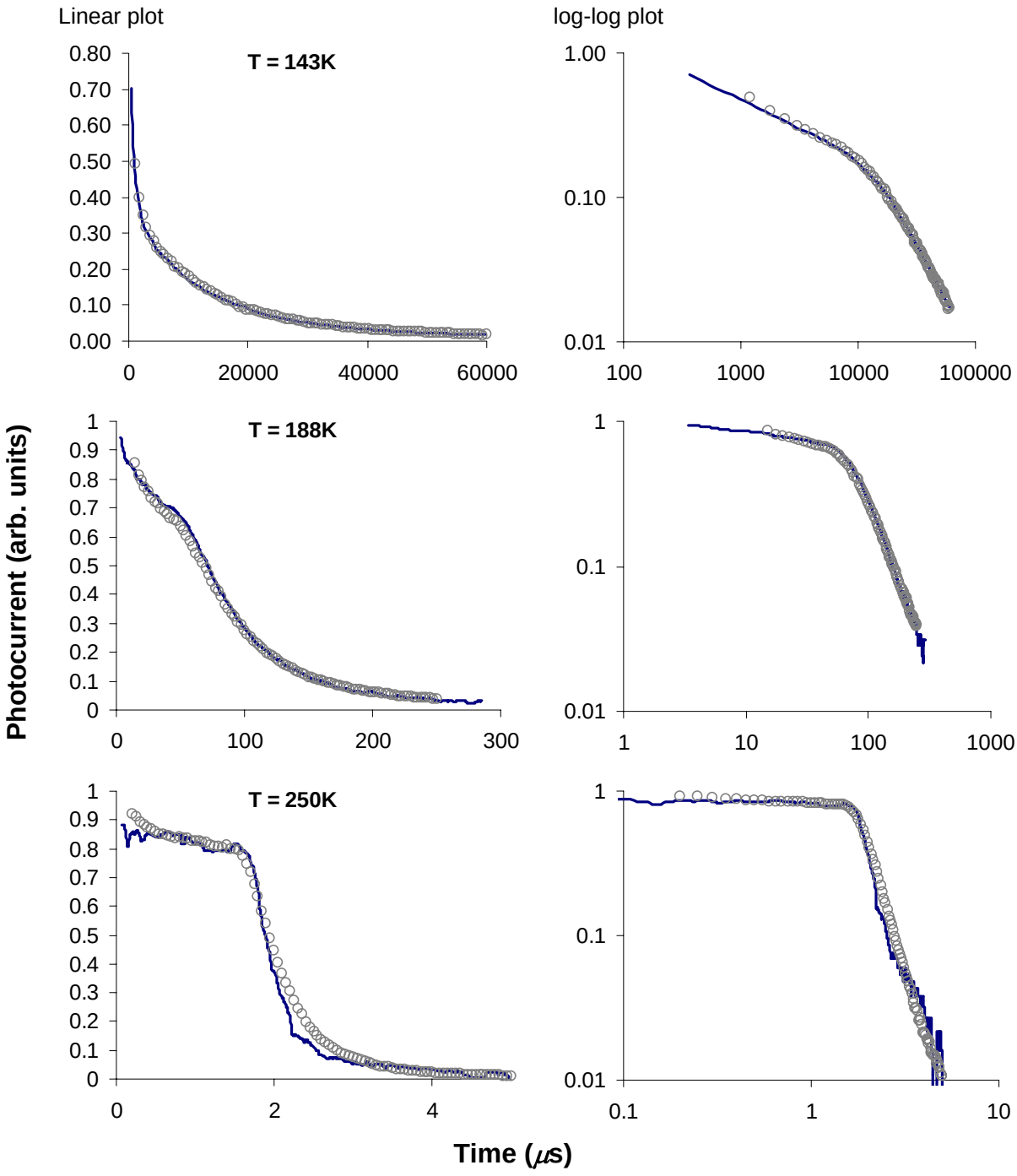

Figure 6.4: Comparison of TOF transient photocurrents at different temperatures reported by Noolandi (solid line) and obtained by Monte Carlo simulation (hollow circles). Curves on the right hand side are the same transient current plotted on log-log scale to emphasize the "knee" representing pre- and post-transit regions. An electric field of 10V/μm was used.

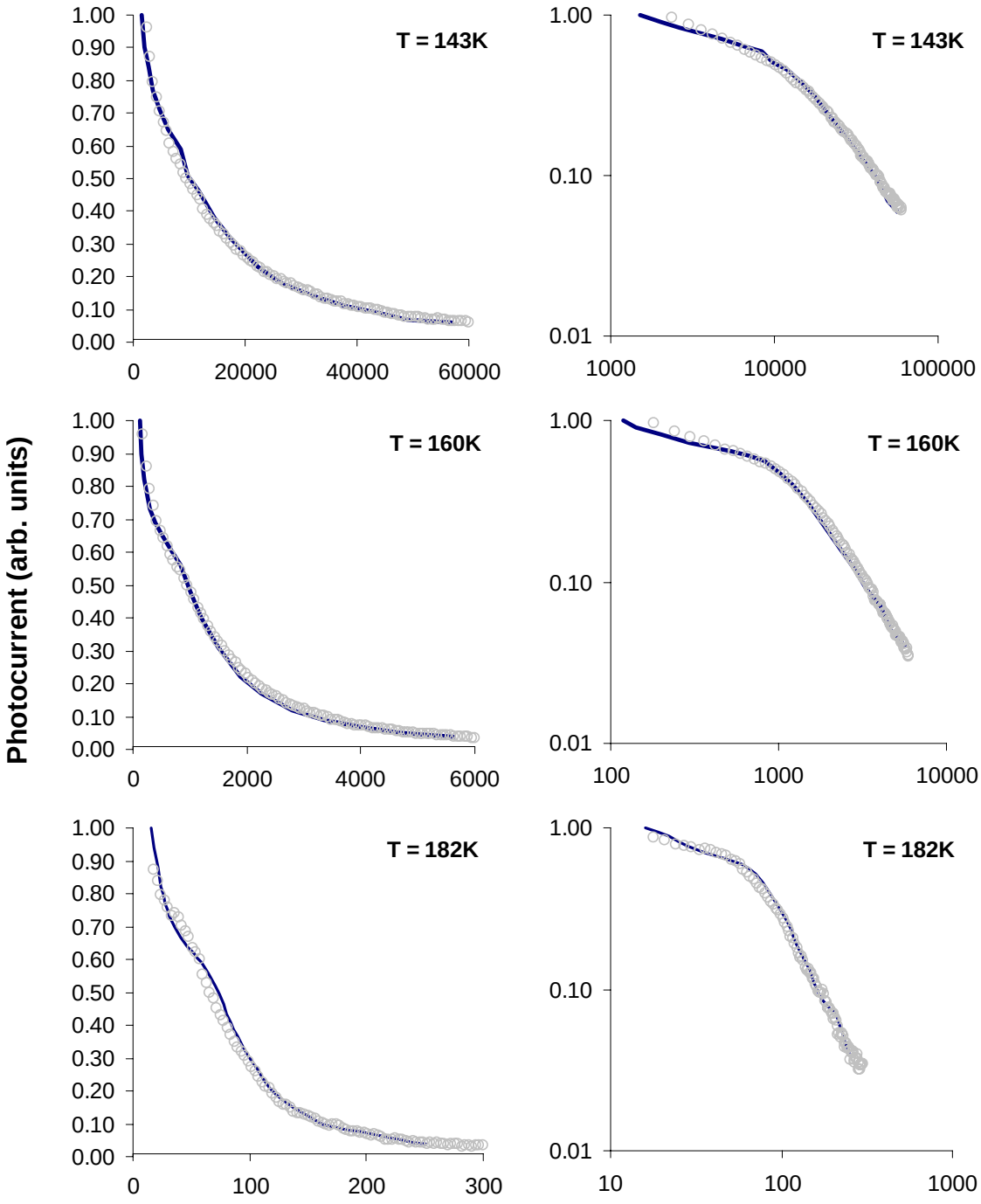
Photocurrent (arb. units)
T = 143K
T = 160K
T = 182K
1.00
0.90
0.80
0.70
0.60
0.50
0.40
0.30
0.20
0.10
0.00
0.01
0
20000
40000
60000
1000
10000
100000
2000
4000
6000
100
200
300
10
1000

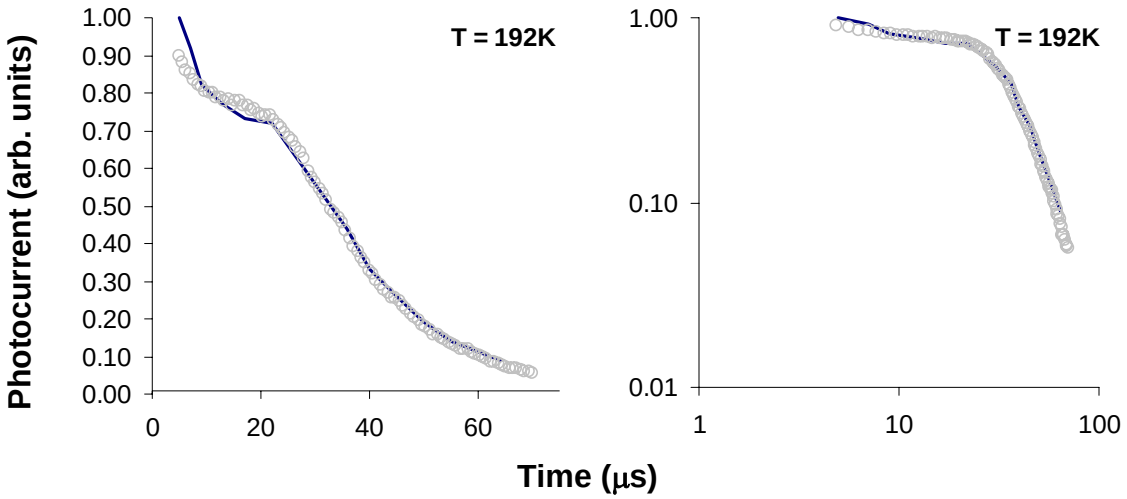

Figure 6.5: Comparison of TOF transient photocurrents at different temperatures reported by Pfister (solid line) and obtained by Monte Carlo simulation (hollow circles). Curves on the right hand side are the same transient current plotted on log-log scale. Electric field of 10V/μm was used.

6.4 Drift Mobility-Temperature characteristics

The DOS distribution model proposed by Koughia [50] (investigated in the previous section) is a monotonic featureless distribution contrary to the DOS models proposed by previous researchers, since almost all of them contain peaks or small bumps at various energies. In this section the drift mobility-temperature characteristics for a simplified monotonous distribution and a Gaussian shaped distribution are investigated. First a simple exponential distribution was used to calculate TOF transient photocurrents for different electric fields and temperatures. From the TOF photocurrents the drift mobility is calculated using $\mu_d = L/t_T F$. The transit time t_T was taken to be at the "knee" of the log-log current waveform, which separates so-called, pre- and post transit regions. The expression for the DOS distribution used is

$$N(E) = N_v \exp\left(-\frac{E}{\delta E}\right)$$

where N_v is the effective density of states at the VB mobility edge N_v= 1×10^{21} cm^{-3}, δE = 300K $\cdot$ k_B = 2.59×10^{-2} eV. Hence using the purely exponential DOS distribution,

photocurrents as a function of electric field and temperature were calculated. The photocurrents are calculated for electric field values of F = 1 V/μm, 5 V/μm, and 20 V/μm. The drift mobility-temperature characteristics at these electric fields for a purely exponential distribution are shown in Figure 6.6. The calculated drift mobility versus reciprocal temperature characteristics are similar to the those reported previously by a number of researchers [17,79,80,81]. The log(μ_h) vs. 1000/T curves has a saturation region at high temperatures and a linearly decreasing region at low temperatures. Field dependence of hole drift mobility is clearly visible from the calculated characteristics.

Next hole transient photocurrents using a purely Gaussian DOS distribution in the mobility gap of a-Se were calculated. and the μ_h vs. 1000/T characteristics were determined in the same manner as for the exponential distribution. The activation energy is estimated from the slope of the linear region of μ_d versus 1000/T curve (ΔE = slope. k. 1000). The activation energy for fields of 1 V/μm and 5 V/μm is calculated to be ~0.2 eV and 0.15 eV for 20 V/μm field.

The position of the Gaussian distribution is taken to be at 0.2 eV. The Gaussian DOS distribution mathematically can be written as

$$N(E) = N_t \exp\left(-\left(\frac{E - \Delta E}{\sigma} \right)^2 \right),$$

where $E - \Delta E$ represents the position of the Gaussian distribution above E_v and σ is the standard deviation of the distribution and is taken as 30 meV. The mobility-temperature characteristics are calculated from the transient photocurrents and are shown on the same Figure 6.6. From the mobility-temperature characteristics it is clear the drift mobility from a monotonic and featureless DOS distribution at lower temperatures is field dependent. While the characteristics from a Gaussian "bump" are independent of the electric field. The exponential and Gaussian distributions were selected as simplified DOS distributions to study the monotonous character of the proposed DOS.

(a)

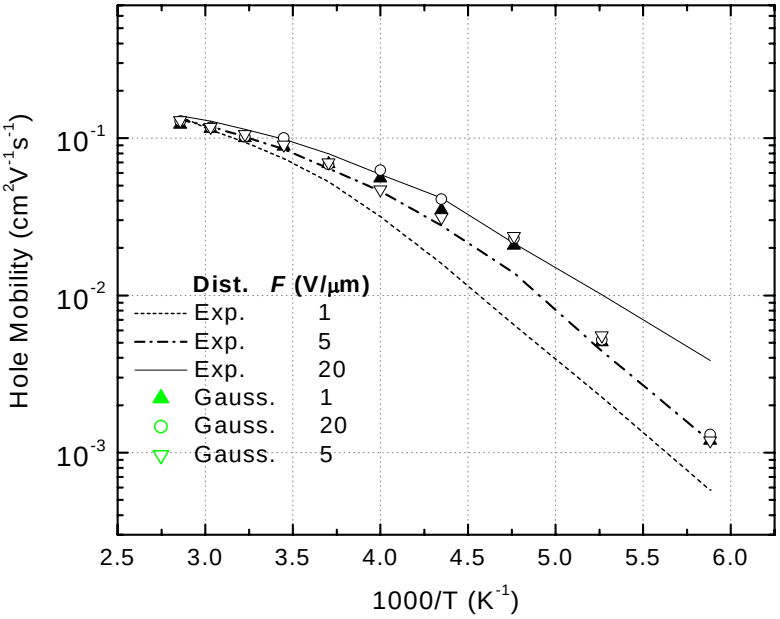

(b)

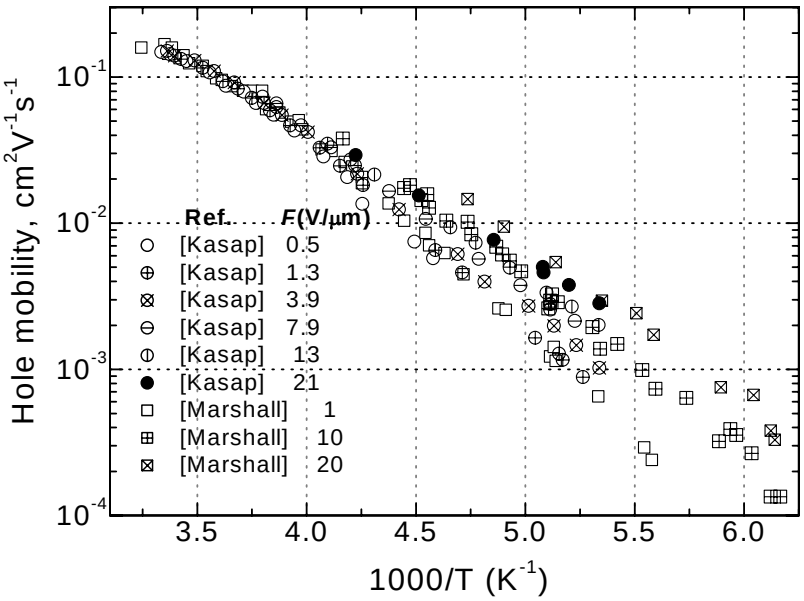

Figure 6.6: Mobility-temperature characteristics (a) for purely exponential and purely Gaussian distribution calculated using MC technique for three different electric fields. The dotted lines represent the characteristics for exponential distribution, and the symbols represent the characteristics for Gaussian distribution (b) the characteristics reported by previous researchers.

It is clear that only a featureless distribution can account for the electric field dependence of hole drift mobility as observed from the μ_h vs. $1000/T$ reported by Kasap [81] and Marshall [17], as shown in Figure 6.6(b).

6.5 Summary

In this chapter the DOS distribution near the VB mobility edge proposed by Koughia [50] was investigated. It is proposed that the DOS distribution near valence band edge E_v is a featureless, monotonically decreasing distribution almost like an "exponential tail" in energy up to E_v + 0.4 eV, without the 0.28 eV peak near the valence band which was thought to control the hole drift mobility. The DOS distributions are shown in the Figure 6.1. It is clear that the DOS distributions have a monotonic character and a clear absence of prominent features. Above E_v + 0.2 eV, DOS may be approximated roughly by a single exponential with characteristic energy $\delta E \approx 19$ meV which corresponds to a characteristic temperature $T_c \approx 220$ K. The monotonic change in the DOS distribution (without any features) was the main factor for the reasonable agreement between the MC calculations and experimental data. The DOS distribution was further optimized by allowing the mobility edge to shift with temperature, which is characterized by (Δ) the shift per unit temperature and is approximately $\sim 3\times10^{-4}$ eV K^{-1}.

The DOS distribution discussed here may not be unique; rather it is an *effective* density of states that was able to result in TOF photocurrents that satisfy the electric field and temperature variations. The interesting aspect of the proposed DOS model is that it satisfies experimental results for varying temperature from different sources. As mentioned previously amorphous selenium has two allotropes in the crystalline phase: trigonal Se (γ-Se) that is comprised of aligned Se chains in which only holes can drift, and α-monoclinic (α-Se) which consists of Se_8 rings, in which only electrons can drift. In the amorphous form and in the trigonal phase, the valence band is formed by lone pair (LP) interactions. Fluctuations in LP interactions are related to changes in the dihedral angle (ϕ) along the chain. The fluctuations in the amorphous form result in the formation of tail states that control the hole drift mobility. In γ-Se, the hole mobility is controlled by lattice scattering [82], whereas in a-Se, it is controlled by multiple trapping in the tail states. Koughia et al. have proposed that the hole transport mechanism undergoing multiple trapping interactions

with tail states in amorphous selenium is analogous to electron transport in a-Si:H. Further work that is based on combining an exponential tail and a Gaussian peak could be useful.

7 Summary and Conclusions

Amorphous selenium is one of the most widely studied amorphous materials not only because of its commercial applications but also due to its status as a prototype amorphous semiconductor. Its most important application has been in Xerography. For almost four decades it has been the material of choice in Xerographic applications until it was replaced by organic photoconductors. Recently it has again attracted attention due to its properties as an X-ray photoconductor in direct conversion X-ray image detectors and as an avalanche photoconductor in ultrahigh sensitivity video tubes called HARPICONs.

The energy distribution of localized states in the mobility gap is one of the most general characteristics of amorphous semiconductors. Despite a long history of research the exact shape of the DOS distribution in the mobility gap of amorphous selenium is still a subject of controversy. This research project is aimed at developing a MC simulation model for carrier transport in amorphous selenium in a TOF photoconductivity experiment to investigate the DOS distribution.

The MC simulation method consists of simulating the motion of a carrier sheet resulting from photoexcitation inside a sample, subject to the force from an applied electric field and of multiple trapping and release events. The duration of the free flight of carriers and their dwell time in the trapping centers have been stochastically calculated with the given probabilities of these events. The MC simulation model for TOF experiment was first developed for semiconductors with monoenergetic and three trap level distributions. The carrier sheet profile at various time intervals was compared with the theoretical solution by Zanio and Akutagawa [58]. The TOF photocurrent results were found to be in excellent agreement and verified our MC approach. The TOF transient photocurrent for the three trap

level model calculated using the MC technique was compared with inverse Laplace transform calculations. These calculations agreed perfectly as well.

The DOS distribution in the upper half of the mobility gap near the CB edge was then investigated. The MC simulation model was used to calculate TOF transient photocurrents at different electric fields and the results were compared with experimentally measured photocurrents. The DOS distribution that provides the best agreement with the photocurrents is the final accepted model. The resulting DOS distribution is a modified version of Abkowitz's model and has following distinct features:

1. The first peak is at ~0.30 eV below the CB mobility edge with a relatively stable amplitude of ~ 10^{17} eV^{-1} cm^{-3}.
2. A second smaller peak at 0.45-0.50 eV below E_c with amplitude of 10^{14}-10^{15} cm^{-3} eV^{-1}.

The exact distribution of deep states with an integral concentration of 10^{14}-10^{15} cm^{-3} eV^{-1} lying at 0.65 eV below E_c could not be resolved. In the MC simulations, these deep states were considered in the form of a Gaussian distribution below 0.65 eV. The exact position of these states below 0.65 eV did not affect the shape of calculated transient photocurrents. The first peak at 0.3 eV is believed to be associated with intrinsic defects like the distortion of the normal dihedral angel in the random chain model of amorphous selenium. The shoulder peak at 0.45-0.50 eV below E_c and the deep traps are believed to be thermodynamic defects.

The density of states (DOS) distribution in the vicinity of the valence band mobility edge in amorphous selenium has been investigated by studying the dependence of the shape of TOF transient photocurrent on temperature, and also the dependence of the drift mobility on the temperature and field. It is observed that analogous to electron transport in a-Si:H, the DOS near E_v is a featureless, monotonically decreasing distribution in energy up to E_v + 0.4 eV, without the 0.28 eV peak near the valence band which was thought to control the hole drift mobility. However further work is needed to confirm the latter conclusion.

The simulation results point to a DOS distribution that is shown in the Figure 7.1.

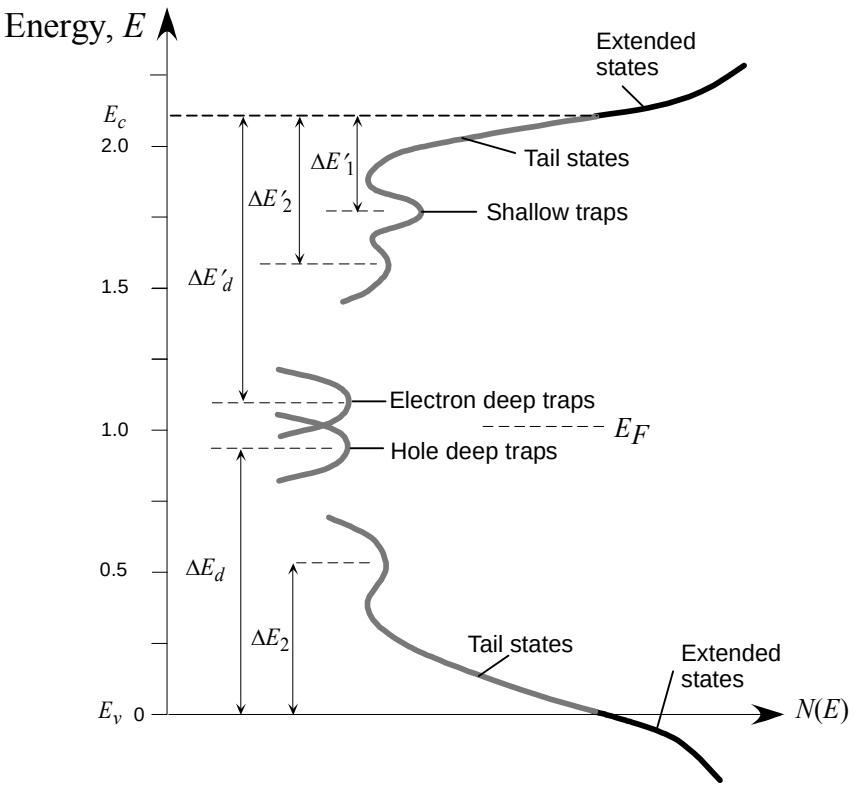

Figure 7.1: Salient features of the DOS model investigated in this research work [49].

8 References

1 N. A. Goryunova and B.T. Kolomiets, *Zh. Tekh. Fiz.* (Journal of Technical Physics, USSR), **25**, 2069-2078, 1955.

2 J.M. Marshall, "Carrier Diffusion in Amorphous Semiconductors", *Report on Progress in Physics*, **46**, 1235-1282, 1983.

3 W. Smith, *Nature* (London), **7**(170), 303, 1873.

4 J.D. Bronzino, *Biomedical Engineering and Instrumentation: Basic Concepts and Applications, PWS Engineering*, Boston USA, pp 403

5 John Rowlands and Safa O. Kasap, "Amorphous Semiconductor Usher in Digital X-ray Imaging", *Physics Today*, November Issue, 1997.

6 S.O. Kasap and J.A. Rowlands, in *Insulating and Semiconducting Glasses*, edited by Boolchand (World Scientific, Singapore 2002), pp. 781

7 S.O. Kasap, M. Zahangir Kabir, J.A. Rowlands, "Recent advances in X-ray photoconductors for direct conversion X-ray image detectors", *Current Applied Physics*, **6**, 288-292, 2006.

8 Safa O. Kasap, John A. Rowlands, "Direct-conversion flat panel X-ray image sensors for digital radiography", *Proceedings of the IEEE*, **90**, 591-604, 2002.

9 S.O. Kasap, J.A. Rowlands, "Direct-conversion flat panel X-ray image detectors", *IEE Proceedings: Circuits, Devices and Systems*, **149**, 85-96, 2002.

10 Safa. O. Kasap, Chris Haugen, Chris, Mark Nesdoly, J.A. Rowlands, "Properties of a-Se for use in flat panel X-ray image detectors", *Journal of Non-Crystalline Solids*, **266-269**, 1163-1167, 2000.

11 S.O. Kasap, John Rowlands, B. Fogal, M. Zahangir Kabir, G. Belev, N. Sidhu, Brad Polischuk, Robert E. Johanson, "Progress in the science and technology of direct conversion a-Se X-ray sensors", *Journal of Non-Crystalline Solids*, **299-302**, 988-992, 2002.

12 C. Haugen, S.O. Kasap, J. Rowlands, "Charge transport and electron-hole-pair creation energy in stabilized a-Se x-ray photoconductors", *Journal of Physics D: Applied Physics*, **32**, 200-207, 1999.

13 S.O. Kasap, J.A. Rowlands, "X-ray photoconductors and stabilized a-Se for direct conversion digital flat panel X-ray image-detectors", *Journal of Materials Science: Materials in Electronics*, **11**, 179-198, 2000.

14 D.L. Lee, L.K. Cheung, and L. Jeromin, "New Digital Detector for Projection Radiography", *SPIE Proceeding*, **2432**, 237-249, 1995.

15 D.L. Lee, L.K. Cheung, E.F. Palecki, and L. Jeromin, "Discussion on Resolution and Dynamic Range of Se-TFT Direct Digital Radiographic Detector", *SPIE Proceeding*, **2708**, 511-522, 1996.

16 W. Zhao, and J.A. Rowlands, "X-Ray Imaging Using Amorphous Selenium: Feasibility of a Flat Panel Self-Scanned Detector for Digital Radiology", *Medical Physics*, **22**, 1595-1604, 1995.

17 J.M. Marshall and A.E. Owen, "The Hole Drift Mobility of Vitreous Selenium", *physica status solidi* (*a*), **12**, 181-191, 1972.

18 B.T. Polischuk, "*Interrupted Field Time-of-Flight Photoconductivity Technique and its Applications to Amorphous Semiconductors*", Ph.D. Thesis, University of Saskatchewan, 21-22, 1994.

19 Kasap, S.O., *Optoelectronics and Photonics: Principles and Practices*, Prentice Hall, Upper Saddle River, New Jersey, 2001.

20 N.F. Mott, "Electrons in Disordered Structures", *Advances in Physics*, **16**, 49-57, 1967.

21 P.W. Anderson, "Absence of Diffusion in Certain Random Lattices", *Physical Review*, **109**, 1492-1505, 1958.

22 M.H. Cohen, H. Fritzsche, and S.R. Ovshinski, "Simple Band Model for Amorphous Semiconductor Alloys", *Physical Review Letters*, **22**, 1065-1072., 1969.

23 N.F. Mott, E.A. Davis, and R.A. Street, "States in the Gap and Recombination in Amorphous Semiconductors", *Philosophical Magazine*, **32**, 961-996, 1975.

24 A. Madan, P.G. Le Comber, and W.E. Spear, "Investigation of The Density of Localized States in a-Si Using the Field Effect Technique", *Journal of Non-Crystalline Solids*, **20**, 239-257, 1976.

25 G. Lucovsky, "Physics of Selenium and Tellurium", ed. by E. Gerlach and P. Grosse, Springer-Verlag, New York, 1979.

26 G. Lucovsky, and F.L. Galeener, "Intermediate Range Order in Amorphous Solids", *Journal of Non-Crystalline Solids*, **35-36**, 1209-1214, 1980.

27 S.O. Kasap, "Photoreceptors: The Selenium Alloys", *Handbook of imaging materials*, ed. by A.S. Diamond, Marcel Dekker Inc., New York, 329-372, 1991.

28 P.E. Meek, "Structural Interpretations of the Vibrational Spectra of Models of Amorphous As and Se", *Proceeding of the Symposium on the structure of Non-Crystalline Solids*, ed. by P.H. Gaskell, Taylor and Francis Ltd., London, 235-237, 1977.

29 J. Robertson, "Electronic Structure of Amorphous Semiconductors", *Advances in Physics*, **32**, 361-452, 1983.

30 M. Kastner, D. Adler, and H. Frutzsche, "Valence-Alternation Model for Localized Gap States in Lone-Pair Semiconductors", *Physical Review Letters*, **37**, 1504-1507, 1983.

31 M. Kastner, "Amorphous and Liquid Semiconductors", *Seventh International Conference on Amorphous and Liquid Semiconductors*, ed. by W.E. Spear, University of Edinburgh, Edinburgh, 504, 1977.

32 D. Adler, "Amorphous Semiconductors", *Scientific American*, **236**, 36-48, 1977.

33 D. Adler and E.J. Yoffa, "Localized Electronic States in Amorphous Semiconductors", *Canadian Journal of Chemistry*, **55**, 1920-1929, 1977.

34 M. Abkowitz, "Changes in the Photoelectric Properties of Glassy Chalcogenides Induced by Chemical Doping, Irradiation, and Thermal History", *Journal of Chemical Physics*, **46**, 4537, 1967.

35 S.C. Agarwal, "Nature of Localized States in Amorphous Semiconductors: A Study by Electron Spin Resonance", *Physical Review B*, **7**, 685-691, 1973.

36 S.R. Elliot, "Physics of Amorphous Materials", Longman, New York, 1984.

37 S.R. Elliot, "A Unified Model for Reversible Photostructural Effects in Chalcogenide Glasses", *Journal of Non-Crystalline Solids*, **81**, 71-98, 1986.

38 D. Carles, G. Lefrancois, and J.P. Larmagnac, "A Model for Steady-State Photoconductivity in Amorphous Selenium", *Journal of Physics Letters*, **45**, L901-L906, 1984.

39 M. Abkowitz, “Density of States in a-Se from Combined Analysis of Xerographic Potentials and Transient Transport Data”, *Philosophical Magazine Letters*, **58**, 53-57, 1988.

40 H.-Z. Song, G.J. Adriaenssens, E.V. Emelianova, and V.I. Arkhipov, “Distribution of Gap States in Amorphous Selenium Thin Films”, *Physical Review B*, **59**, 10607 - 10613, 1999.

41 S.O. Kasap and J.A. Rowlands, “X-Ray Photoconductors and Stabilized a-Se for Direct Conversion Digital Flat panel X-Ray Image-Detectors”, *Journal of Materials Science: Materials in Electronics*, **11**, 179, 2000.

42 L. Benkhedir, M.S. Aida, G.J. Adriaenssens, “Defect Levels in the Band Gap of Amorphous Selenium”, *Journal of Non-Crystalline Solids*, **344,** 193-198, 2004.

43 L. Benkhedir, M. Brinza and G. J. Adriaenssens, “Electronic Density of States in Amorphous Selenium”, *Journal of Physics: Condensed Matter*, **16**, S5253- S5264**,** 2004.

44 N. Qamhieh, M. K. Benkhedir, M. Brinza, J. Willeken, and G. J. Adriaenssens, “Steady-State Photoconductivity in Amorphous Selenium Glasses”, *Journal of Physics Condensed Matter*, **16**, 3827-3833, 2004.

45 K. Koughia, Z. Shakoor, S.O. Kasap, and J.M. Marshall, “Density of Localized Electronic Sates in a-Se from Electron Time-of-Flight Photocurrent Measurements”, *Journal of Applied Physics*, **97**, 033706-1-033706-11, 2005.

46 M. Abkowitz, “Density of States in a-Se from Combined Analysis of Xerographic Potentials and Transient Transport Data”, *Philosophical Magazine Letters*, **58**, 53-57, 1988.

47 H.-Z. Song, G.J. Adriaenssens, E.V. Emelianova, and V.I. Arkhipov, “Distribution of Gap States in Amorphous Selenium Thin Films” *Physical Review B: Condensed Matter*, **59**, 10607-10613, 1999.

48 N. Qamhieh, M.K. Benkhedir, M. Brinza, J. Willeken, and G.J. Adriaenssens, “Steady-State Photoconductivity in Amorphous Selenium Glasses”, *Journal of Physics Condensed Matter*, **16**, 3827-3833, 2004.

49 S.O. Kasap, J.A. Rowlands, T. Tanioka, A. Nathan, Applications of Disordered Semiconductors in Modern Electronics: Selected Examples, Wiley, (To be published).

50 K. Koughia, S.O. Kasap, "Density of States of a-Se Near the Valence Band", *Journal of Non-Crystalline Solids* (in press)

51 M. Abkowitz, and R. Enck, “Xerographic Spectroscopy of Gap States in Amorphous Semiconductors”, *Physical Review B*, **25**, 2567-2577, 1982.

52 J. Veres, and C. Juhasz, “Cycled Xerographic and Time-of-Flight Measurements: Theory and Experiment”, *Journal of Non-Crystalline Solids,* **164-166,** 407, 1993.

53 S.O. Kasap and J.A. Rowlands, “Review: X-Ray Photoconductors and Stabilized a-Se for Direct Conversion Digital Flat panel X-Ray Image Detectors”, *Journal of Materials Science: Materials in Electronics*, **11**, 179-198, 2000.

54 W.E. Spear, “Electronic Transport and Localization in Low Mobility Solids and Liquids”, *Advances in Physics*, **23**, 523-543, 1974.

55 N.F. Mott, and E.A. Davis, “Electronic Processes in Non-Crystalline Materials”, Oxford, 1971 1st ed., 1979 2nd Ed.

56 W.E. Spears, "Drift Mobility Techniques for the Study of Electrical Transport Properties in the Insulating Solids", *Journal of Non-Crystalline Solids*, **1**, 197-214, 1969.

57 K. Hecht, “Zum mechanismus des lichtelektrischen primärstromes in isolierenden kristallen”, *Zeitschrift Fur Physik*, **77**, 235-245, 1932.

58 K.R. Zanio, W.M. Akutagawa, and R. Kikuchi, “Transient Currents in Semi-Insulating CdTe Characteristics of Deep Traps”, *Journal of Applied Physics*, **39**, 2818-2828, 1968.

59 M. Martini, J.W. Mayer, and K.R. Zanio, “Drift Velocity and Trapping in Semiconductors Transient Charge Technique”, *Applied Solid State Science: Advances in Materials and Devices Research*, edited by R. Wolfe, Academic Press, 225, 1972.

60 R.M. Blakney, H.P. Grunwald, "Small Signal Current Transients in Insulators with Traps", *Physical Review*, **159**, 658-664, 1967.

61 A.I. Rudenko, V.I. Arkhipov, “Drift and Diffusion in Materials with Traps - 1. Quasi-Equilibrium Transport Regime”, *Philosophical Magazine B.*, **45**, 177-187, 1982.

62 http://www.mathworks.com/support/solutions/data/1-169M3.html?solution=1-169M3, The MathWorks, Solution Number: 1-169M3, MathWorks.com

63 M.D. Tabak, and M. Scharge, “Transition from Emission Limited to Space Charge Limited Photoconductivity”, *Journal of Applied Physics*, **41**, 2114-2118, 1970.

64 H. Michiel, and G.J. Adriaenssens, and E.A. Davis, “Extended-State Mobility and its Relation to the Tail-State Distribution in A-Si:H”, *Physical Review B*, **34**, 2486-2499, 1986.

65 F. W. Schmidlin, “Theory of Trap-Controlled Transient Photoconduction”, *Physical Review B*, **16**, 2362-2385, 1977.

66 J. Noolandi, “Multiple-Trapping Model of Anomalous Transit Time Dispersion in A-Se”, *Physical Review B*, **16**, 4466-4473, 1977.

67 G.A. Baker Jr., and P. Graves-Morris Padé, Approximants (Cambridge University Press, New York, 1996).

68 H. E. Johns and J. R. Cunnigham, The Physics of Radiology, 4th edition, 1983.

69 M. Yunus, "Monte Carlo Modeling of the Sensitivity of X-ray Photoconductors", M.Sc. Thesis, University of Saskatchewan, pp. 61-62, 2005

70 J. Mort, "Acoustoelectric Current Saturation in Trigonal Selenium", *Physical Review Letters*, **18**, 540-543, 1967.

71 W.E. Spear, "Carrier Mobility and Charge Transport in Monoclinic Se Crystals", *Journal of Physics and Chemistry of Solids*, **21**, 110-115, 1961.

72 C. K. Wong, G. Lucovsky, and J. Bernholc, "Intrinsic Localized Defect States in a-Se Associated with Dihedral Angle Distortions", *Journal of Non-Crystalline Solids*, **97**, 1171-1174, 1987.

73 H.-Z. Song, G. J. Adriaenssens, E. V. Emelianova, and V. I. Arkhipov, "Distribution of Gap States in Amorphous Selenium Thin Films", *Physical Review* B, **59**, 10607-10613, 1999.

74 U. Sciebel, T. Buchkremer, G. Frings, and P. Quadflieg, "Deep Trapping and Recombination in a-Se:As X-Ray Sensitive Photoreceptors", *Journal of Non-Crystalline Solids*, **115**, 216-218, 1989.

75 M. Abkowitz, “Density of States in a-Se from Combined Analysis of Xerographic Potentials and Transient Transport Data”, *Philosophical Magazine Letters*, **58**, 53-57, 1988.

76 H. Naito, T. Iwai, M. Okuda, T. Matsushita and A. Sugimura, "Computer Simulation Study of Tail-State Distribution in Amorphous Selenium", *Journal of Non-Crystalline Solids,* **114**, 112-114, 1989.

77 S.O. Kasap and C. Juhasz, "Time-of-Flight Drift Mobility Measurements on Chlorine-Doped Amorphous Selenium Films", *Journal of Physics D: Applied Physics*, **18**, 703, 1985.

78 M.K. Benkhedir, M. Brinza and G.J. Adriaenssens, "Electronic Density of States in Amorphous Selenium", *Journal of Physics: Condensed Matter*, **16**, S5253-S5264, 2004.

79 H.P. Grunwald, and R.M. Blakney, "Electron and Hole Drift Mobilities in Vitreous Selenium", *Physical Review*, **165**, 1006, 1968.

80 W.E. Spear, *Proceeding of Physical Society*, **B76**, 826, 1960.

81 S.O. Kasap and C. Juhasz, "Time-of-Flight Drift Mobility Measurements on Chlorine-Doped Amorphous Selenium Films", *Journal of Physics D: Applied Physics*, **18**, 703-720, 1985.

82 S. O. Kasap in The Handbook of Imaging Materials , 2nd ed. Ed. By A. Diamond and B. Weiss, Marcel Dekker, p. 329-368, 2002.